A pathway for mitotic chromosome formation

A pathway for mitotic chromosome formation

Johan H. Gibcus[1*], Kumiko Samejima[2*], Anton Goloborodko[3*$], Itaru Samejima[2], Natalia Naumova[1], Johannes Nuebler[3], Masato Kanemaki[4], Linfeng Xie[5], James R. Paulson[5], William C. Earnshaw[2#], Leonid A. Mirny[3#], Job Dekker[1,6#]

[1] Program in Systems Biology, Department of Biochemistry and Molecular Pharmacology, University of Massachusetts Medical School, 368 Plantation Street, Worcester, MA 01605, USA

[2] Wellcome Centre for Cell Biology University of Edinburgh, King's Buildings, Max Born Crescent Edinburgh EH9 3BF, Scotland, UK

[3] Institute for Medical Engineering and Science, and Department of Physics, Massachusetts Institute of Technology, Cambridge, MA 02139

[4] Division of Molecular Cell Engineering, National Institute of Genetics, Research Organization of Information and Systems (ROIS), and Department of Genetics, SOKENDAI, Yata 1111, Mishima, Shizuoka 411-8540, Japan.

[5] Department of Chemistry, University of Wisconsin-Oshkosh, 800 Algoma Blvd, Oshkosh, WI 54901

[6] Howard Hughes Medical Institute, 4000 Jones Bridge Road, Chevy Chase, MD 20815-6789, USA

*: equal contribution

#: Correspondence: WCE: bill.earnshaw@ed.ac.uk; LAM: Leonid@MIT.edu; JD: Job.Dekker@umassmed.edu

Abstract

Mitotic chromosomes fold as compact arrays of chromatin loops. To identify the pathway of mitotic chromosome formation, we combined imaging and Hi-C of synchronous DT40 cell cultures with polymer simulations. We show that in prophase, the interphase organization is rapidly lost in a condensin-dependent manner and arrays of consecutive 60 kb loops are formed. During prometaphase ~80 kb inner loops are nested within ~400 kb outer loops. The loop array acquires a helical arrangement with consecutive loops emanating from a central spiral-staircase condensin scaffold. The size of helical turns progressively increases during prometaphase to ~12 Mb. Acute depletion of condensin I or II shows that nested loops form by differential action of the two condensins while condensin II is required for helical winding.

One Sentence Summary

Mitotic chromosome folding occurs through condensin-mediated loss of the interphase conformation and formation of increasingly compacted helically arranged nested loop arrays.

Introduction

Chromosomes dramatically change their conformation as cells progress through the cell cycle. Throughout most of interphase, chromosomes of vertebrates display two layers of organization: topologically associating domains (TADs) (*1*, *2*) and A- and B-compartments (*3*). At a finer scale, chromatin looping between promoters, enhancers and CTCF-bound sites (*4*, *5*) facilitates gene regulation. During mitosis, these features disappear and chromosomes are compacted into dense arrays of randomly positioned consecutive chromatin loops (*6–9*).

Although the organization of these two states is now increasingly understood, much less is known about how cells convert from one state into the other. Previous microscopy observations revealed that chromosomes become recognizable during prophase and form linearly organized structures where sister chromatids are initially mixed (*10–13*). By late prophase, sister chromatid arms separate and each chromatid is thought to be organized as an array of loops that emanate from an axial core containing condensin complexes and topoisomerase II alpha (*14–18*). During prometaphase, the chromatids shorten and become thicker (*11*), ultimately forming fully condensed metaphase chromosomes (*19*). How compaction of loop arrays occurs during prometaphase is not known.

Here we employ a chemical-genetic system for highly synchronous entry of DT40 cells into prophase. DT40 cells are karyotypically stable, near diploid (**Fig. S1**) and have been extensively used for analysis of mitotic chromosome organization (*20*). Use of chemical genetics (*21*) in this cell system allowed us to apply Hi-C with high temporal resolution and to determine how chromosome conformation changes as cells disassemble the interphase nucleus and form mitotic chromosomes (*22*, *23*). These data, combined with polymer simulations (*24*, *25*) and

direct imaging reveal a mitotic chromosome morphogenesis pathway with distinct transitions, including compartment and TAD loss, loop array formation by late prophase and chromosome shortening during prometaphase through growing and winding of loops around a central helical scaffold. Using an auxin-inducible degron approach (*26*, *27*) we then identify distinct key roles for condensin I and II in this pathway.

Results

Synchronous progression into mitosis

To obtain cultures of cells that synchronously enter mitosis we arrested cells in G_2 by selectively inhibiting CDK1. We stably expressed a variant of *Xenopus laevis* CDK1 cDNA (CDK1as) harboring a F80G mutation in DT40 cells (*22*, *28*). This mutation renders CDK1as sensitive to inhibition by the ATP analog 1NM-PP1 (*22*). We then disrupted the endogenous CDK1 gene using CRISPR/Cas9. Growing cells for 10 hours in the presence of 1NM-PP1 efficiently arrested >90% of cells in G_2 as indicated by FACS (**Table S1,** **Fig. S2**) and by microscopy analysis of chromosome and nuclear morphology (**Fig. 1A**). Washing out 1NM-PP1 led to rapid release of cells from the G_2 arrest and synchronous entry into prophase.

This system allowed us to study chromosome morphogenesis by harvesting cells at sequential time points for imaging and Hi-C analysis as they synchronously progress through mitosis. For some cultures collected at later time points (30 - 60 minutes), we added nocodazole 30 minutes prior to their release from the 1NM-PP1 arrest, to block the metaphase-anaphase transition (see Methods). All time courses described here were performed in duplicate and results were highly concordant. DAPI staining showed the expected chromosome condensation and individualization in prophase (**Fig. 1A**). Nuclear envelope breakdown (NEBD) occurred around t = ~7 - 10 minutes as evidenced by staining for Lamin B1, which diffuses into the cytoplasm upon NEBD (**Fig. S3**) (*29*) and by measuring the association of previously cytoplasmic condensin I subunits with the chromosomes (CAPD2, CAPG1, CAPH and increased levels of SMC2 and SMC4; **Fig. S4A,B**). Previous studies, and our proteomic analysis (**Fig. S4B**) show that by late prophase, cohesin (SMC1 and SMC3) has dissociated from the arms of sister

chromatids, which separate, but remain aligned (*11*, *12*, *30*, *31*). Chromosome shortening subsequently occurred during prometaphase and at the late time points fully condensed chromosomes were observed (**Fig. 1A**).

Loss of compartments and TADs in Prophase

Hi-C analysis showed that G_2-arrested cells display all features characteristic of vertebrate interphase cells (*8*). First, chromosomes form territories as indicated by relatively high levels of intra-chromosomal interactions (*3*). Second, chromosomes display the characteristic pattern of active A- and inactive B- compartments as revealed by the plaid pattern of Hi-C interactions (*3*) (**Fig. 1B**). The locations of these compartments in G_2 resembled those detected in exponentially growing cells, though the compartment signal strength was stronger and the pattern sharper in the synchronous cells likely as a result of uniformity in cell cycle stage. Third, TADs were readily visible in the Hi-C interaction maps as squares of relatively high interaction frequencies along the diagonal (**Fig. 1C**). TAD boundaries were similar in position and strength to those in non-synchronous cells as determined using an insulation score calculated from a 250 kb sliding window (*32*) (**Fig. S5**). Finally, we analyzed how contact frequency (*P*) of contacts between locus pairs depends on their genomic distance (*s*). *P(s)* decays with genomic distance and this relationship changes with cell cycle stages (*8*). For G_2 cells, we found *P(s)* to be highly similar to that observed previously in non-synchronous cells (**Fig. S6, Fig. S7**). Together, these analyses show that G_2 chromosomes, which are composed of two closely aligned and likely catenated sister chromatids, are organized similarly to G_1 chromosomes (*8*).

This interphase chromosomal organization was rapidly lost upon release of cells into prophase. As soon as 5 minutes after release we detected a marked reduction in the typical plaid

pattern of long-range interactions, indicating a loss of compartments (**Fig. 1B**). By 10 minutes (late prophase) compartments were mostly gone. At the same time, TADs were also lost (**Fig. 1C, Fig. S8**).

We used eigenvector decomposition to quantify the disappearance of compartments (*33*). The first eigenvector readily captured compartments at t = 0 and 2.5 minutes, but starting at t = 5 minutes it explained progressively less of the variance in the Hi-C interaction maps, indicating weakening of the compartment structure. By t = 7.5 minutes the strength of the first eigenvector fell to 17% (from 80% at t = 0 minutes) and by t = 10 minutes, it no longer captured compartments. Loss of compartments was also quantified by calculating the ratio of A-to-A or B-to-B interactions over A-to-B interactions over the time course. From t = 0 to t = 2.5 minutes and onward this fraction decreased steadily, indicating that preferential interactions within compartments are lost (**Fig. 1D, Fig. S9**).

The strength of TADs can be quantified using the insulation score, which indicates the amount of contacts formed across a locus up to a certain distance (*32*). TAD boundaries have a low score (indicative of high insulation), whereas loci inside TADs show a high score value (no insulation). The genome-wide variance of insulation scores provides a quantitative measure of the presence of TADs (*8*). Starting at t = 2.5 minutes the variance of the insulation profiles progressively decreased, indicating loss of TADs (**Fig. 1C, Fig. S5B**). By t = 7.5 minutes the variance was reduced more than 2-fold and by t = 10 minutes no TADs were detected. This conclusion was confirmed by plotting the average Hi-C interaction pattern at and around TAD boundaries identified in G_2 at different time points during mitosis (**Fig. 1C**). Insulation is strongest in G_2 and by late prophase insulation values are near background levels (quantified in **Fig. S10**). We conclude that compartments and TADs disappear rapidly during early prophase.

By late prophase, when sister arms have resolved (*11*, *34*), and around the time of nuclear envelope breakdown (t ~ 7.5-10 minutes), the Hi-C maps are characterized by a general decay of contact frequency *P* with genomic distance *s* (**Fig. 2A**). The shape of the *P(s)* curve changes as prophase progresses. In G_2 cells, it is shallow ($P(s) \sim s^{-0.5}$) up to a distance of several hundred kb, reflecting compaction within TADs (*35*, *36*), but for larger distances the decay becomes steeper. During prophase, the initial shallow decay extends for longer-range interactions, with a steeper drop at 2 Mb at t = 10 minutes, suggesting a higher degree of compaction. As we demonstrate below, this decay and shape are consistent with formation of a linearly arranged, layered organization of the chromosome (*8*), where the size of each layer corresponds to the position of the steep drop in the *P(s)* curve.

Appearance of a second diagonal band in Hi-C maps from prometaphase cells

At t = 15 minutes, when cells have entered prometaphase, the Hi-C maps produce a *P(s)* curve with a drop at 2 Mb. Strikingly, a distinct second diagonal band appears, running in parallel with the primary diagonal for all loci and chromosomes (**Fig. 1B, Fig. S11**). This second diagonal represents increased interaction frequencies between any pair of loci separated by around 3 Mb. At 15 min, this feature is clearly observed in *P(s)* plots as a local peak at ~3 Mb (**Fig. 3A, Fig. S6, Fig. S7**). As cells progress through prometaphase, the position of the drop in *P(s)* and the position of the second diagonal migrate to larger genomic distances (**Fig. 3A**; **Fig. S6, S7**). By t = 60 minutes, when compact metaphase chromosomes have formed, the second diagonal is positioned at ~12 Mb and appears more diffuse. The second diagonal appears in all chromosomal maps and its position is independent of chromosome size over two orders of magnitude (**Fig. S11**). The appearance and movement of the second diagonal is not dependent or affected by

nocodazole: no nocodazole was added to the t = 15 minute sample, and a replicate Hi-C dataset obtained from a culture collected at t = 30 minutes in the absence of nocodazole was nearly identical to the data obtained in the presence of nocodazole (**Table S2, Fig. S7, Fig. S8**). Together, these *P(s)* curves reveal a periodicity of interactions that reflects chromosome structure at the scale of megabases.

The only known regular periodic structural feature of chromosomes is helical coiling, which was first described in 1880 (*37*) and can be observed in certain chromosome preparations (*10*, *38–40*). Experimentally induced banding of the chromosome arms is much more irregular (*41*). In helical chromosomes with a pitch (the length of a complete turn) of ~3 Mb, each locus is in relatively close proximity to loci located one turn up or down the chromosome, i.e. 3 Mb up or downstream along the DNA. The progressive movement of the second diagonal band to larger distances during prometaphase would reflect an increased "winding up" and shortening of the helix.

Although this is the first Hi-C data revealing the helical coiling of chromosomes, the chicken DT40 late prometaphase (t = 60 minutes) Hi-C contact maps strongly resemble those for mitotic human HeLa S3 chromosomes that we had reported earlier (*8*). In fact, re-analysis of mitotic HeLa S3 Hi-C data in more detail by deeper sequencing revealed a weak second diagonal band at ~10 Mb distance (**Fig. S12**), suggesting this periodic folding is a conserved feature of vertebrate mitotic chromosomes.

Testing models of chromosomes

Previous studies suggested that mitotic chromosomes are organized as arrays of consecutive loops emanating from a condensin-rich scaffold, forming a polymer bottlebrush (*42*, *43*), with a

layered organization of loops (*6*, *19*, *44*). To understand chromosome organization at different stages of compaction we built coarse-grained models of chromosomes as arrays of loops aiming to reproduce *P(s)* curves of Hi-C data, separately for each time point. In these models, a chromosome is represented by a cylinder with an axial scaffold; loop bases are arranged consecutively along the scaffold, and each chromatin loop, emanating from the scaffold in a particular direction, is represented by a blob of loci (**Fig. 2B,** see Supplemental Material). Loops are regularly placed along the axis, with angular positions determined by a stochastic model; loop sizes are exponentially distributed and bases of loops are not positioned at defined genomic sequences or loci (*8*). Analysis of condensin ChIP data for DT40 cells (*45*) supports sequence-independent positioning for >95% of loops (Supplemental Material, **Fig. S13**; see discussion). For specific models of loop arrangements, presented below, the *P(s)* curve can be found analytically as the return probability of a stochastic process describing angular positions of loops (see Supplemental Material, section "Coarse-grained model of contact probability decay in mitotic chromosomes"). The resulting *P(s)* always has three regions (**Fig. 2B**): (i) the intra-loop region at short separations, where two loci are likely to be within the same loop and *P(s)* reflects the internal organization of loops; (ii) the "intra-layer" region at larger genomic separations, where loci are located on different loops within the same axial layer of the cylindrical chromosome and *P(s)* reflects the specific arrangement of loops relative to each other; (iii) the "inter-layer" that appears as a steep drop in contact frequency at large genomic distances, where loci are located in loops that are so distant along the scaffold that their blobs can no longer overlap. In the *P(s)* plot of experimental Hi-C data throughout mitosis, the intra-layer region and the drop-off can be readily discerned (**Fig. 2A, 2C**).

Prophase chromosomes

The coarse-grained models show that the relative orientation of consecutive loops strongly affects the shape of the *P(s)* curve in the intra-layer region. If the orientations of consecutive loops are independent of each other, the contact frequency *P(s)* does not decay with genomic distance in the intra-layer region, as any pair of loops within a layer are equally likely to interact (**Fig. 2C**). In contrast, introducing correlations between orientations of consecutive loops, i.e. forcing neighboring loops to project in similar directions, makes them follow an angular random walk. The angular random walk is a 1D random walk on a circle and has a return probability of $P(s) \sim s^{-0.5}$ until the full turn is made by the walk. The $P(s) \sim s^{-0.5}$ decay followed by a drop is in good agreement with the late prophase Hi-C data (t = 7-10 minutes – **Fig. 2C**). Taken together, these results suggest that by late prophase chromosomes are already organized into arrays of consecutive loops with correlated angular orientations.

We developed detailed polymer models to test whether specific classes of conformations can reproduce experimental Hi-C data, though they do not prove mechanisms by which these structures form. Further, all our simulations produce equilibrium models and do not reflect kinetics of chromosome folding. In these models, chromatin is represented as a 10 nm fiber (*46*, *47*), where one monomer corresponds to one nucleosome (**Fig. 2D**), allowing us to simulate up to 40 Mb of chromatin. Prophase chromosomes are modeled as arrays of consecutive loops of exponentially distributed length and random genomic locations, emanating from a flexible scaffold, as would result from a loop extrusion process (*48*). The loop array is further condensed by imposing poor solvent conditions to the density observed in electron microscopy (one nucleosome per 11x11x11nm cube, i.e. ~40% volume fraction) (*49*), while preserving the overall cylindrical shape of the chromosome (**Fig. 2D**). We systematically varied two parameters: the

average loop size and the linear loop density along the chromosomal scaffold (**Fig. 2E**). For all combinations, we generated equilibrium conformations, simulated a Hi-C experiment, and evaluated its ability to reproduce *P(s)* curves from Hi-C data for different time points during prophase (**Fig. 2E-H**).

These polymer models can accurately reproduce *P(s)* (20 kb<s<4 Mb) for all prophase time points, in agreement with the prediction of the coarse-grained model (**Fig. 2C**). The best matching models for later prophase time points, when sister chromatids are separate and lie side-by-side, have gradually increasing average loop size: from 40-50 kb at t = 5 minutes to ~60-70 kb at t = 10 minutes (**Fig. 2H**), reproducing the gradually shifting position of the drop-off from 2 to 3.5Mb (i.e. increase of the layer size), while maintaining about the same ~50 loops per layer and ~250 loops per μm. These results are consistent with a model where loop arrays are formed early in prophase, and loop sizes grow gradually, e.g. by merging smaller adjacent loops (*25*). Thus, both coarse grained modes and polymer simulations indicate that by late prophase, chromosomes fold as dense arrays of loops, with consecutive loops positioned with correlated radial orientations.

Prometaphase spirals

A striking feature of prometaphase Hi-C data is the appearance of the second diagonal band, which appears as a distinct peak on the *P(s)* curves (**Fig. 3A**). This feature cannot be explained by interactions between sister chromatids, as these become minimal in prometaphase, and simulations show that no amount of overlap between sisters gives rise to such periodic pattern in interactions (**Fig. S14**). As argued above, periodic interactions seen by Hi-C are most readily explained by a helical organization of mitotic loop arrays, which has been observed

microscopically (*6, 10, 40, 50*). Two classes of chromosome architecture can give rise to periodicity in contact frequencies: an "external" helix when the whole chromosome is folded into a solenoid (*50*) (the solenoid model), and a "staircase" model in which consecutive loops wind in a helical order around a centrally located scaffold ("internal" helix). We note that by "scaffold" we do not necessarily imply a solid integrated structure stretching from one end of the chromosome to the other. The "scaffold" could equally be a dynamic association of smaller complexes linked by DNA that pack with helical symmetry. By modeling we examined these classes of architectures and the continuum of models in between them.

To explore whether an internal helix can arise through reorganization of loop orientations, while preserving the cylindrical morphology of the whole chromosome, we extended our coarse-grained prophase model (**Fig. 2B**) by adding a preferred angular orientation for each loop: (1) as in prophase, the orientation of each loop is correlated with its neighbors; (2) these loops have preferred, but not fixed, orientations that follow a helical path, thus winding around the chromosomal scaffold (**Fig. 3B**). Loops in this spiral staircase model follow an angular Ornstein-Uhlenbeck random walk with bias toward preferred positions, and *P(s)* can be found analytically (*51*) (Supplemental Material, section "Coarse-grained model of contact probability decay in mitotic chromosomes – loops with spiral staircase orientation"). This coarse-grained model yields a *P(s)* curve that closely follows the experimental prometaphase *P(s)* and displays both the $P(s) \sim s^{-0.5}$ decay and the narrow peak corresponding to the second diagonal band (**Fig. 3C**). These results indicate that, (i) the emergent second diagonal band in Hi-C data can result from a spiral organization, and (ii) such organization can arise from preferred orientations of loops around the central scaffold. Further support for a centrally located spiraling scaffold is provided by analysis of chromosome shape and SMC2-mAID-GFP, CAP-H-mAID-

GFP or CAP-H2-mAID-GFP localization along mitotic chromosomes from colchicine arrested DT40 cells (**Fig. 3B**, **Fig. S15, Fig. S16**). We observe a pattern of condensin localization that is consistent with a helical path of the scaffold.

Detailed polymer modeling allowed us to explore a broader range of architectures, with both external and internal helices, and to obtain quantitative estimates of loop sizes and other aspects of organization. Two aspects of the prometaphase organization must be captured by any model: (i) a higher linear density of chromatin of up to 50-70 Mb/μm, necessitating an evolution of the loop architecture; and (ii) spiraling of the scaffold. The higher density of loops can be achieved by a nested loop organization where several smaller (inner) loops are organized consecutively within each larger (outer) loop whose bases form the central axis (**Fig. 3D**). The presence of nested loops is an essential feature for prometaphase models, as models with a single layer of loops could not reproduce Hi-C *P(s)* curves even when other parameters were varied (**Fig. S14B**). To model helical architecture we made the scaffold follow a helical path in 3D, while allowing loops to adopt their equilibrium conformations within an otherwise cylindrical chromosome (**Fig. 3D**).

We systematically varied the model parameters, such as geometry of the spiral scaffold and loop sizes (**Fig. 3E**). This also probed different lengths and widths of chromosomes as the volume density was kept constant. For t = 30 minutes the best agreement was achieved for a relatively narrow internal spiral staircase-like scaffold (R=30-60nm) (**Fig. 3F-G**). This spiral is much more narrow than the ~300nm diameter of the chromatid, and has a small pitch (the height of one turn, 100-200nm) (**Fig. 3H**). Interestingly, this spiral arrangement of loop bases can achieve helical winding of loops that reproduces the second diagonal in the interaction maps and the peak on the *P(s)* curves for t = 15, 30 and 60 minutes (**Fig. 3F-H**). Wider spiraling of the

scaffold (**Fig. 3G-III**) approximating external helix architectures (*50*) failed to accurately reproduce *P(s)* (**Fig. S14C**). Taken together, coarse-grained and polymer models that agree with Hi-C data overwhelmingly support the spiral staircase ("internal" helix) architecture of the scaffold (I and II in **Fig. 3G**), and subsequent helical winding of loops.

Fitting consecutive time points probed by Hi-C, we found that the linear chromatin density of the best-matching models continued to grow throughout prometaphase, in agreement with the observed steadily shortening of mitotic chromosomes (**Fig. 1A, 3H, Fig. S18**). Simulations show that shifting the peak in *P(s)* to larger genomic distances representing the second diagonal in consecutive time points (**Fig. 3A**) can be achieved by increasing the radius of the helical scaffold from 30 to 100 nm, the radius of the chromatid from 300 to 360 nm, and increasing the pitch from 100 to 250 nm, while maintaining a constant outer and inner loop size (~400 kb and ~80 kb respectively) (**Fig. 3H**). These changes lead to the increase in amount of DNA (Mb) per turn of the spiral from ~3 Mb in early prometaphase up to ~12 Mb by late prometaphase.

Comparison of the dimensions of our best models with direct microscopic measurements of prometaphase chromosomes prepared according to the Hi-C protocol reveals good agreement between experiment and predictions (**Fig. S17**).

Condensins are critical for prophase chromosome morphogenesis

To determine the role of condensin complexes in chromosome morphogenesis, we fused a minimal auxin inducible degron domain (mAID) to SMC2 (Supplemental Materials, **Table S3**). In the presence of the plant F-box protein osTIR1, addition of auxin induces rapid proteasome-dependent degradation of the SMC2-mAID protein, thus disrupting both condensin I and II

complexes (*18*, *26*, *27*). Incubation of cells for 3 hours in the presence of auxin during the1NM-PP1-induced G_2–arrest (Supplementary Materials) reduced SMC2 levels to <5% (**Fig. S19**). Remarkably, this did not affect global chromosome organization as compartments and TADs were comparable to those in WT G_2 arrested cells (**Fig. 4A,** **Fig. S20**). Cells entered prophase rapidly after washout of 1NM-PP1, and the onset of NEBD, as indicated by DAPI staining, occurred as in wild type at ~7-10 minutes (**Fig. S21**).

Chromosomes in SMC2-depleted cells did not form well-resolved chromatids as cells progressed to prometaphase, confirming previous observations (**Fig. S21**) (*18*, *52–54*). Chromatin in such cells lacks functional condensin (*55*, *56*), but nonetheless achieves a normal degree of chromatin compaction despite the absence of individualized chromosomes (*57*). FACS analysis confirmed that these cells are incapable of normal mitotic exit. They ultimately undergo mitotic slippage, forming tetraploid interphase cells (**Fig. S2**).

Hi-C analysis revealed that in the absence of SMC2, interphase compartments and TADs were still present and largely unaffected by late prophase, at a time when they were completely disassembled in WT (t = 10 minutes, **Fig. 4A,** **Fig. S20A**). NEBD and spindle assembly did occur; indicating cells progressed to physiological prometaphase. In prometaphase (t = 45 minutes and t = 75 minutes), compartments and TADs progressively weakened, but remained detectable (**Fig. 4A,** **Fig. S22-23**). No second diagonal, characteristic for WT prometaphase ever appeared in Hi-C maps (**Fig. 4A**), instead *P(s)* curves show little change from G_2 (**Figs. S20A, S24-26**). Preferential A-to-A interactions and B-to-B interactions became progressively weaker (**Fig. S20A, S22A**). Analysis of the variation of the insulation score along chromosomes indicated that TAD boundaries were reduced in strength but not eliminated (**Fig. 4A,** **Fig. S23**). Further, removal of cohesin (SMC1/3) and CTCF from chromatin, as assessed by chromatin

enrichment for proteomics (ChEP) (*58*) was delayed and reduced compared to WT (**Fig. S4D**). This may explain the incomplete loss of TAD boundaries. Combined, these data reveal that condensin is not required for TAD and compartment architecture during interphase. In its absence, mitotic chromatin is compacted but chromosomes do not become individualized or acquire the normal mitotic morphology, while partially preserving elements of interphase architecture. This indicates (i) that compaction and formation of rod shaped mitotic chromosomes are two separate processes, as assumed by our model; and (ii) a critical role for condensin is in the formation of proper morphology and internal organization of mitotic chromosomes, and in disassembly of the interphase architecture (*59*).

Condensin I and II play distinct roles in chromosome morphogenesis

Next, we determined the roles of condensin I and II separately. Condensin I and II bind chromatin independently (*52*, *56*, *60*, *61*), and recent in vitro mitotic chromosome assembly experiments show that they can act independently (*62*). Therefore, depletion of one condensin complex is unlikely to affect the other, though we cannot rule out more subtle interplay between the complexes. We fused auxin inducible degron domains to the condensin II-specific kleisin CAP-H2 (CAP-H2-mAID) or the condensin I-specific kleisin CAP-H (CAP-H-mAID) in CDK1as DT40 cells (Supplemental Methods). Addition of auxin lead to >95% protein depletion in G_2–arrested CAP-H-mAID or CAP-H2-mAID cells (**Fig. S19**). Cells were then released from the G_2 block and chromosome conformation was determined by microscopy and Hi-C as cells progressed through mitosis.

Depleting either condensin I or II alone led to less severe phenotypes than depleting both together (**Fig. S21**). In contrast to cells lacking both condensin I and II (SMC2-mAID), these cells exited mitosis within 3 hours after entry into prophase (**Fig. S2**).

Comparison of Hi-C interaction matrices (**Fig. 4BC, Fig. S20BC**) and *P(s)* curves (**Fig. 5A, 5B, Fig. S24BC, S25-26**) for CAP-H and CAP-H2 depleted cells in late prometaphase (t = 30 minutes and 60 minutes) shows that they capture different aspects of the WT architecture. The *P(s)* curve for CAP-H2-depleted cells, where only condensin I remains active, matches that of the intra-layer organization of WT up to ~6 Mb, and lacks the second diagonal band (**Fig. 5B**). The *P(s)* curve for CAP-H depleted cells (active condensin II), matches that of WT only for the long-range organization (6-20 Mb), including the second diagonal band (**Fig. 5B**). CAP-H depleted cells have a much lower contact frequency between loci separated less than 6 Mb than do WT and CAP-H2 depleted cells. Thus, condensin I and II play distinct roles at different structural levels, in mitotic chromosome morphogenesis, providing a mechanistic explanation for earlier microscopic studies (*60*, *61*, *63*, *64*).

Helical winding during prometaphase requires condensin II

In condensin II-depleted cells, both A- and B-compartments and TADs were lost starting around the prophase-prometaphase transition (t = 10 - 15 minutes; **Fig. 4B, Fig. S20, Fig. S22**). In late prometaphase (t = 30 - 60 minutes), chromosomes in these cells were longer and narrower than WT chromosomes, as previously observed (*60*, *63*, *64*) (**Fig. S21**). *P(s)* curves for t = 10 and 15 minutes (early prometaphase) resembled those in WT for late prophase (t = 10 minutes; compare **Fig. 5A** with **Fig. 2A**), displaying a mild decay followed by a steep drop that is characteristic for a densely packed loop array (**Fig. 2B**). Most strikingly, CAP-H2 depletion prevented emergence

of the second diagonal band in prometaphase in Hi-C contact frequency maps and *P(s)* plots (**Fig. 4B, 5B;** **Fig. S20B, S24B**).

The close similarity between CAP-H2 prometaphase and WT prophase Hi-C, and lack of the second diagonal, allowed us to model CAP-H2 chromosomes as a prophase-like array of a single layer of loops emanating from a flexible, non-helical scaffold. By systematically varying the loop size and the degree of linear compaction, we obtained excellent agreement with experimental *P(s)* curves for ~40-60 kb loops, and a linear density of 15 Mb/μm for all prometaphase time points (**Fig. 5D, 5E**). This linear density is 3-4 times smaller than that of WT prometaphase chromosomes (50-70 Mb/μm). These simulations indicate that in the absence of condensin II, prometaphase chromosomes form extended prophase-like loop arrays and do not progress to further longitudinal shortening and helical winding.

Condensin I modulates the internal organization of prometaphase helical layers

Cells depleted for CAP-H (**Fig. S19**) seemed to progress through prophase normally: Hi-C data show a rapid loss of compartments and TADs (**Fig. 4C,** **S20C, S22, S23**) and by late prophase individual chromosomes were discerned by DAPI staining (**Fig. S21**). Deviation from the WT morphogenesis pathway was observed during prometaphase, i.e. after NEBD, when the bulk of condensin I normally loads in WT (**Fig. S4B, C**). A second diagonal was observed at 30 minutes indicating helical winding of the chromatids (**Fig. 4C,** **S20C**) but this was located at a genomic distance of ~12 Mb, which in WT cells was only observed at t = 60 minutes. Therefore, the progression to larger helical turns during prometaphase is accelerated in cells lacking CAP-H.

Despite a spiral organization, loss of condensin I leads to a different loop arrangement and folding, as seen from differences in the *P(s)* curves: the intra-layer arrangement of loops

shows a characteristic $P(s) \sim s^{-0.5}$ from 400 kb to ~3 Mb, with *P(s)* for the s<400 kb region having a different slope, possibly reflecting a different intra-loop organization. These features are captured well by the coarse-grained model with 200-400 kb loops emanating with correlated angular orientations from a spiral scaffold (**Fig. 5G**). This loop size agrees well with the sizes of outer loops in the best models for WT chromosomes at t = 60 minutes (**Fig. 3H**).

Strikingly, when we matched the t = 30 minutes *P(s)* curve with the simulations of prometaphase chromosomes with helical scaffolds and nested loops, the best match was achieved with either a single layer of 200 kb loops, or a nested system of loops, with 400 kb outer loops and 200 kb inner loops (**Fig. 5F**). Together these results suggest that CAP-H (condensin I) is essential for formation of short (60-80 kb) inner loops but is dispensable for ~200-400 kb outer loops emanating from a helical staircase scaffold. The helical arrangement appears weaker in condensin I depleted chromosomes, as illustrated by the reduced strength of the second diagonal and reduced peaks in the *P(s)* plots. One possible reason for this could be the much larger loop sizes in condensin I depleted chromosomes that may allow larger disorder in their angular arrangement. Taken together, our data obtained with CAP-H and CAP-H2 depleted cells support the formation of nested loops during prometaphase.

Discussion

We delineate a folding pathway from interphase to metaphase at minute time resolution. Hi-C data reveal a periodic pattern of interactions that we show to be consistent with a helical staircase model of mitotic chromosome folding. This model unifies many disparate observations made over the last several decades. We demonstrate that mitotic chromosomes have nested loops that are formed by differential action of condensin I and II, with condensin II being required for helical coiling of mitotic chromosomes. Finally, we find that condensins are required for the timely loss of the interphase nuclear architecture.

A mitotic chromosome morphogenesis pathway

The data and modeling presented here suggest a chromosome morphogenesis pathway by which cells convert interphase chromosome organization into compacted mitotic chromosomes (**Fig. 6**). Together, our imaging and Hi-C data, coarse-grained models and polymer simulations, and previous observations (*11*) reveal that upon entry into prophase, interphase features such as compartments and TADs are lost within minutes in a condensin-dependent process and by late prophase, chromosomes are organized as radial loop arrays. The mechanism by which TADs and compartments are lost is not known. Our data show that condensin is required. Additional contributing factors could include loss of CTCF and cohesin binding (**Fig. S4B, S4C**) and increased levels of loop extrusion that can erase boundaries even when CTCF is still bound (Supplemental Materials, **Fig. S27**). Importantly, activation of the mitotic kinase cascade is not sufficient to disassemble interphase chromatin organization without the action of condensin.

Our models that achieve best agreement with Hi-C data show that during prophase, condensin II-dependent loops grow from 30-40 kb to 60 kb in size, leading to a ~2-fold increase in linear chromatin density from ~7 Mb/μm to 15 Mb/μm. Condensins at loop bases form a chromosomal scaffold (*19*, *62*), which may be a dynamic, rather than static structure, and loops are arranged consecutively along it (one loop every ~5 nm of the axis). Interestingly, the radial arrangement of loops around the central flexible scaffold is not random, with consecutive loops projecting in similar directions i.e. with an angularly correlated arrangement.

Chromosomes shorten along their longitudinal axis and become wider during prometaphase. Our simulations show that condensin II loops continue to grow to 200-400 kb by 30 min and 400-700 kb by 60 min, accompanied by an increase in the linear chromatin density, which reaches 60 Mb/μm. However, two important reorganizations take place during prometaphase. First, large condensin II-mediated loops are subdivided into smaller 80 kb loops in a condensin I-dependent process, thus producing a nested loop arrangement with ~400 kb outer loops and ~80 kb inner loops. Second, the loop array acquires a helical arrangement as evidenced by the appearance of a second diagonal band in Hi-C maps for all loci and chromosomes. Models show that this helical arrangement of loops can be achieved if the scaffold forms a narrow helical “spiral staircase” inside an otherwise homogeneous cylindrical chromosome. Interestingly, the period, radius and pitch of this helix continue to grow through prometaphase, and this growth is to some extent restrained by condensin I. An emerging model of the prometaphase chromosome thus has a central helical scaffold formed by condensin II (*62*) that organizes 200-400 kb outer loops, that are further subdivided into 80 kb condensin I-mediated inner loops in order to achieve a high volume density.

Comparison to previous and classical studies

While specific details of this model emerge from an unbiased fitting of models to the data, the emerging organization and its quantitative characteristics agree with earlier studies. First, the 60-80 kb sizes of the inner loops are remarkably similar to values suggested by an extensive survey of the literature (*44*), measurements from electron microscopy (*6*, *19*) and Hi-C analysis of mitotic HeLa cells (*8*). Similarly, changes of linear density from prophase to prometaphase in the best models (from 15 Mb/μm to 50 Mb/μm) are consistent with prophase chromosomes being at least two-fold longer than metaphase chromosomes (*11*, *61*).

Second, helical prometaphase chromosomes have long been observed in certain chromosome preparations (*10*, *37*, *38*, *40*), and this has led to diverse models for how mitotic chromosomes are folded. Our analysis of Hi-C data indicates that the prometaphase chromosome is organized around a helical central region or scaffold: loops emanate with helical packing from a centrally located "spiral staircase" scaffold. Modeling shows that other helical arrangements of loop arrays, e.g. coiling of the entire loop array itself (*40*, *50*, *65*, *66*), are not consistent with our Hi-C data.

Our helical scaffold/loop model unifies a range of models and observations made over the years. It explains how a helical chromatin packing arrangement can be achieved while scaffold proteins such as condensins and topoisomerase II are localized centrally (*15–17*), within a cylindrical chromatid that is not obviously helical when visualized with a DNA dye such as DAPI (*67*). Interestingly, by late prometaphase we estimate the height of one helical turn to be around 200 nm, which is also the size of the layer (12 Mb layer at linear density 60 Mb/um), and

is consistent with microscope observations suggesting that consecutive genomic loci follow a helical gyre with a pitch of ~250 nm within the cylindrical shape of chromatids (*68*).

Possible mechanisms

Such loop arrangements can naturally emerge due to a process of loop extrusion. Loop extrusion has been hypothesized as a mechanism of chromosome compaction (*69*, *70*) and most recently examined by simulations (*25*, *48*, *71*) and supported by single-molecule studies (*72*). In this process, each condensin starts forming a progressively larger loop until it dissociates or stops being blocked by neighboring condensins or other DNA-binding proteins. A recent study demonstrated that this process can form an array of consecutive loops (*8*) with condensins forming a central scaffold in the middle of a cylindrical chromosome (*48*), essential features of mitotic chromosomes. We note that sister chromatids are resolved by late prophase (*11–13*) indicating that the formation of loop arrays occurs as sister chromatid arms become separated.

Another aspect of loop extrusion is that loop sizes are established by a dynamic process of condensin exchange, without a need for barrier elements or specific loading sites (*25*). This is consistent with our Hi-C data that suggests that loop bases are not positioned at specific reproducible positions (e.g. scaffold or matrix attachment regions - (*73*, *74*)) in a population of cells. Analysis of published chromatin immunoprecipitation data for SMC2 in mitotic DT40 cells (*45*) shows a low level of condensin binding throughout the genome and only very few loci enriched in condensin binding: only 289 sites show more than a 5-fold enrichment compared to DNA input and 4,617 sites show over 2-fold enrichment. These numbers are much lower than the 16,000 inner loops our data and models predict. Interestingly, the condensin-enriched sites do show a Hi-C interaction pattern consistent with them being at the bases of loops slightly more

frequently than other loci (Supplemental Materials, **Fig. S13**). Based on these analyses, we estimate that over 95% of mitotic loops are not positioned at specific loci.

Simulations show that loop extrusion slowly approaches steady state by exchanging condensins and gradually increasing loop sizes during this process (*25*). This is consistent with gradual growth of loops up to 500 kb by slowly-exchanging condensin II, and relatively rapid formation of 60-80 kb inner loops by the more rapidly exchanging condensin I (*75*).

Formation of nested loops was critical for our polymer simulations to reproduce prometaphase Hi-C data because only this allowed a higher linear chromatin density. In this architecture, the outer loop bases are located at the central scaffold, while the inner, nested loop bases are radially displaced. Our analysis of condensin I or II depletion reveals that condensin II generates outer loops and condensin I generates inner loops. Our simulations reveal that this nested loop arrangement can be explained by the longer half-life of condensin II and shorter half life of condensin I on chromatin as measured by FRAP (*75*) (Supplemental Material, **Supplemental Movie 1**). Indeed, nested loops only form in prometaphase, when condensin I gains access to chromatin. Thus, loop extrusion models can explain the nested loop arrangement of condensed mitotic chromosomes.

Why condensin II-based scaffolds only acquire helicity in prometaphase, and not in prophase is not known, but this could involve interactions with other proteins, such as DNA topoisomerase IIalpha or KIF4A. Our estimates of the radius of the prometaphase scaffold of 30-100 nm is consistent with a 50 nm length of SMC coiled coils that can interact with each other through HEAT repeats (*76*) which are known for ability to self-assemble into a helical “spiral staircase” (*77*). Gradual formation of such a HEAT-mediated staircase and binding of other factors can explain how the pitch and the radius of the helix increase in time.

We note that mitotic chromatin still condenses in the absence of both condensin I and II, although individualized rod-shaped chromosomes are not formed and cells cannot progress into anaphase. This indicates that there are other mechanisms by which chromatin fibers become condensed during mitosis. Our simulations also show that to achieve agreement with Hi-C data, chromatin should also be condensed (computationally analogous to poor solvent conditions) forming densely packed chromatin loops within mitotic chromosomes analogous to the dense packing of chromatin observed in mitotic chromosomes by electron microscopy (*46*, *78*, *79*). The molecular basis for this condensation is not known but may involve mitosis-specific chromatin modifications (*80*, *81*) or active motor proteins such as KIF4A (*82*, *83*).

The chromosome morphogenesis pathway described here, and the identification of distinct architectural roles for condensin I and II in organizing chromosomes as nested loop arrays winding around a helical "spiral staircase" within a cylindrical chromatid can guide future experiments to uncover the molecular mechanisms by which these complexes, and other key components such as topoisomerase IIalpha and KIF4A, act in generating, (re-)arranging and condensing chromatin loops to build the mitotic chromosome.

Methods Summary

DT40 Cell cultures synchronously entering mitosis were analyzed by Hi-C, imaging and proteomics to determine the structure of chromosomes. Hi-C data were used to quantify chromosome compartmentalization and to derive relationships between contact frequency P and genomic distance s. Coarse grained models and equilibrium polymer simulations were performed to test models of prophase and prometaphase chromosome organization against Hi-C data, and to identify best fitting parameters for size of loops, helical turn and pitch, linear density (Mb/micron

chromosome length). Imaging of chromosome dimensions and condensin localization were performed to validate model predictions. Cell lines expressing condensin subunits fused to auxin-inducible degron domains were used to efficiently deplete these subunits prior to cells entering mitosis. Hi-C and imaging analysis were then performed to assess the effects of depletion of condensins on mitotic chromosome formation. Detailed procedures for all methods are described in the Supplementary Materials.

References and Notes

1. J. R. Dixon *et al.*, Topological domains in mammalian genomes identified by analysis of chromatin interactions. *Nature*. **485**, 376–380 (2012).
2. E. P. Nora *et al.*, Spatial partitioning of the regulatory landscape of the X-inactivation centre. *Nature*. **485**, 381–385 (2012).
3. E. Lieberman-Aiden *et al.*, Comprehensive mapping of long-range interactions reveals folding principles of the human genome. *Science (80-.).* **326**, 289–293 (2009).
4. S. S. Rao *et al.*, A 3D map of the human genome at kilobase resolution reveals principles of chromatin looping. *Cell*. **159**, 1665–1680 (2014).
5. A. Sanyal, B. R. Lajoie, G. Jain, J. Dekker, The long-range interaction landscape of gene promoters. *Nature*. **489**, 109–113 (2012).
6. W. C. Earnshaw, U. K. Laemmli, Architecture of metaphase chromosomes and chromosome scaffolds. *J. Cell Biol.* **96** (1983) (available at http://jcb.rupress.org/content/96/1/84.long).
7. M. P. Marsden, U. K. Laemmli, Metaphase chromosome structure: evidence for a radial loop model. *Cell*. **17**, 849–58 (1979).

8. N. Naumova *et al.*, Organization of the mitotic chromosome. *Science (80-.).* **342**, 948–953 (2013).

9. T. Nagano *et al.*, Cell-cycle dynamics of chromosomal organization at single-cell resolution. *Nature*. **547**, 61–67 (2017).

10. Y. Ohnuki, Structure of chromosomes. I. Morphological studies of the spiral structure of human somatic chromosomes. *Chromosoma*. **25**, 402–28 (1968).

11. Z. Liang *et al.*, Chromosomes Progress to Metaphase in Multiple Discrete Steps via Global Compaction/Expansion Cycles. *Cell*. **161**, 1124–1137 (2015).

12. K. Nagasaka, M. J. Hossain, M. J. Roberti, J. Ellenberg, T. Hirota, Sister chromatid resolution is an intrinsic part of chromosome organization in prophase. *Nat. Cell Biol.* (2016), doi:10.1038/ncb3353.

13. L. L. Moore, M. B. Roth, HCP-4, a CENP-C-like protein in Caenorhabditis elegans, is required for resolution of sister centromeres. *J. Cell Biol.* **153**, 1199–208 (2001).

14. K. W. Adolph, S. M. Cheng, J. R. Paulson, U. K. Laemmli, Isolation of a protein scaffold from mitotic HeLa cell chromosomes. *Proc. Natl. Acad. Sci. U. S. A.* **74**, 4937–41 (1977).

15. W. C. Earnshaw, M. M. Heck, Localization of topoisomerase II in mitotic chromosomes. *J. Cell Biol.* **100**, 1716–25 (1985).

16. S. M. Gasser, U. K. Laemmli, The organisation of chromatin loops: characterization of a scaffold attachment site. *EMBO J.* **5**, 511–518 (1986).

17. Y. Saitoh, U. K. Laemmli, Metaphase chromosome structure: Bands arise from a differential folding path of the highly AT-rich scaffold. *Cell*. **76**, 609–622 (1994).

18. K. Samejima *et al.*, Mitotic chromosomes are compacted laterally by KIF4 and condensin and axially by topoisomerase IIα. *J. Cell Biol.* **199**, 755–70 (2012).

19. J. R. Paulson, U. K. Laemmli, The structure of histone-depleted metaphase chromosomes. *Cell*. **12**, 817–28 (1977).

20. M. Okada, T. Hori, T. Fukagawa, The DT40 system as a tool for analyzing kinetochore assembly. *Subcell. Biochem.* **40**, 91–106 (2006).

21. A. C. Bishop *et al.*, Design of allele-specific inhibitors to probe protein kinase signaling. *Curr. Biol.* **8**, 257–66 (1998).

22. H. Hochegger *et al.*, An essential role for Cdk1 in S phase control is revealed via chemical genetics in vertebrate cells. *J Cell Biol*. **178**, 257–268 (2007).

23. K. Samejima *et al.*, A promoter-hijack strategy for conditional shutdown of multiply spliced essential cell cycle genes. *Proc. Natl. Acad. Sci.* **105**, 2457–2462 (2008).

24. G. Fudenberg *et al.*, Formation of Chromosomal Domains by Loop Extrusion. *Cell Rep.* **15**, 2038–49 (2016).

25. A. Goloborodko, J. F. Marko, L. A. Mirny, Chromosome Compaction by Active Loop Extrusion. *Biophys. J.* **110**, 2162–2168 (2016).

26. A. J. Holland, D. Fachinetti, J. S. Han, D. W. Cleveland, Inducible, reversible system for the rapid and complete degradation of proteins in mammalian cells. *Proc Natl Acad Sci U S A.* **109**, E3350-7 (2012).

27. K. Nishimura, T. Fukagawa, H. Takisawa, T. Kakimoto, M. Kanemaki, An auxin-based degron system for the rapid depletion of proteins in nonplant cells. *Nat. Methods*. **6**, 917–22 (2009).

28. E. Sonoda, M. Takata, Y. M. Yamashita, C. Morrison, S. Takeda, Homologous DNA recombination in vertebrate cells. *Proc. Natl. Acad. Sci. U. S. A.* **98**, 8388–94 (2001).

29. S. D. Georgatos, A. Pyrpasopoulou, P. A. Theodoropoulos, Nuclear envelope breakdown

in mammalian cells involves stepwise lamina disassembly and microtubule-drive deformation of the nuclear membrane. *J. Cell Sci.*, 2129–40 (1997).

30. I. C. Waizenegger, S. Hauf, A. Meinke, J. M. Peters, Two distinct pathways remove mammalian cohesin from chromosome arms in prophase and from centromeres in anaphase. *Cell*. **103**, 399–410 (2000).

31. A. Losada, M. Hirano, T. Hirano, Cohesin release is required for sister chromatid resolution, but not for condensin-mediated compaction, at the onset of mitosis. *Genes Dev.* **16**, 3004–16 (2002).

32. E. Crane *et al.*, Condensin-driven remodelling of X chromosome topology during dosage compensation. *Nature*. **523**, 240–244 (2015).

33. M. Imakaev *et al.*, Iterative correction of Hi-C data reveals hallmarks of chromosome organization. *Nat Methods*. **9**, 999–1003 (2012).

34. S. Abe *et al.*, The initial phase of chromosome condensation requires Cdk1-mediated phosphorylation of the CAP-D3 subunit of condensin II. *Genes Dev.* **25**, 863–74 (2011).

35. W. Schwarzer *et al.*, Two independent modes of chromosome organization are revealed by cohesin removal. *bioRxiv* (2016) (available at http://biorxiv.org/content/early/2016/12/15/094185.abstract).

36. E. P. Nora *et al.*, Targeted Degradation of CTCF Decouples Local Insulation of Chromosome Domains from Genomic Compartmentalization. *Cell*. **169**, 930–944.e22 (2017).

37. J. Baranetzky, Die Kerntheilung in den Pollenmutterzellen einiger Tradescantien. *Bot. Zeitung*. **38**, 281–296 (1880).

38. Y. Kuwada, Chromosome Structure A critical review. *Cytologia (Tokyo).* **10**, 213–256

(1939).

39. C. L. Woodcock, L. L. Frado, J. B. Rattner, The higher-order structure of chromatin: evidence for a helical ribbon arrangement. *J. Cell Biol.* **99**, 42–52 (1984).

40. E. Boy de la Tour, U. K. Laemmli, The metaphase scaffold is helically folded: sister chromatids have predominantly opposite helical handedness. *Cell*. **55**, 937–44 (1988).

41. J. M. Craig, W. A. Bickmore, Chromosome bands--flavours to savour. *Bioessays*. **15**, 349–54 (1993).

42. J. Paturej, S. S. Sheiko, S. Panyukov, M. Rubinstein, Molecular structure of bottlebrush polymers in melts. *Sci. Adv.* **2** (2016), doi:https://doi.org/10.1126/sciadv.1601478.

43. J. F. Marko, E. D. Siggia, Polymer models of meiotic and mitotic chromosomes. *Mol. Biol. Cell*. **8**, 2217–31 (1997).

44. K. J. Pienta, D. S. Coffey, A structural analysis of the role of the nuclear matrix and DNA loops in the organization of the nucleus and chromosome. *J. Cell Sci. Suppl.* **1**, 123–35 (1984).

45. J. H. Kim *et al.*, Condensin I associates with structural and gene regulatory regions in vertebrate chromosomes. *Nat. Commun.* **4**, 2537 (2013).

46. H. D. Ou *et al.*, *Science (80-.).*, in press, doi:10.1126/science.aag0025.

47. Y. Nishino *et al.*, Human mitotic chromosomes consist predominantly of irregularly folded nucleosome fibres without a 30-nm chromatin structure. *EMBO J.* **31**, 1644–53 (2012).

48. A. Goloborodko, M. V Imakaev, J. F. Marko, L. Mirny, Compaction and segregation of sister chromatids via active loop extrusion. *Elife*. **5** (2016), doi:10.7554/eLife.14864.

49. D. G. Booth *et al.*, 3D-CLEM Reveals that a Major Portion of Mitotic Chromosomes Is

Not Chromatin. *Mol. Cell* (2016), doi:10.1016/j.molcel.2016.10.009.

50. J. B. Rattner, C. C. Lin, Radial loops and helical coils coexist in metaphase chromosomes. *Cell*. **42**, 291–6 (1985).

51. B. D. (Barry D. . Hughes, *Random walks and random environments* (Clarendon Press, 1995; https://global.oup.com/academic/product/random-walks-and-random-environments-9780198537885?cc=us&lang=en&).

52. T. Hirota, D. Gerlich, B. Koch, J. Ellenberg, J.-M. Peters, Distinct functions of condensin I and II in mitotic chromosome assembly. *J. Cell Sci.* **117**, 6435–45 (2004).

53. T. Ono, Y. Fang, D. L. Spector, T. Hirano, Spatial and temporal regulation of Condensins I and II in mitotic chromosome assembly in human cells. *Mol. Biol. Cell*. **15**, 3296–308 (2004).

54. D. F. Hudson, P. Vagnarelli, R. Gassmann, W. C. Earnshaw, Condensin is required for nonhistone protein assembly and structural integrity of vertebrate mitotic chromosomes. *Dev Cell*. **5**, 323–336 (2003).

55. S. Ohta *et al.*, The protein composition of mitotic chromosomes determined using multiclassifier combinatorial proteomics. *Cell*. **142**, 810–21 (2010).

56. S. Ohta *et al.*, Proteomics Analysis with a Nano Random Forest Approach Reveals Novel Functional Interactions Regulated by SMC Complexes on Mitotic Chromosomes. *Mol. Cell. Proteomics*. **15**, 2802–18 (2016).

57. K. Samejima *et al.*, Rapid degradation and 3D CLEM of condensin reveal chromatin compaction uncoupled from chromosome architecture in mitosis. *bioRxiv* (2017) (available at http://biorxiv.org/content/early/2017/08/09/173633.abstract).

58. G. Kustatscher, K. L. H. Wills, C. Furlan, J. Rappsilber, Chromatin enrichment for

proteomics. *Nat. Protoc.* **9**, 2090–9 (2014).

59. M. Yanagida, Clearing the way for mitosis: is cohesin a target? *Nat. Rev. Mol. Cell Biol.* **10**, 489–96 (2009).

60. T. Ono *et al.*, Differential Contributions of Condensin I and Condensin II to Mitotic Chromosome Architecture in Vertebrate Cells. *Cell*. **115**, 109–121 (2003).

61. L. C. Green *et al.*, Contrasting roles of condensin I and condensin II in mitotic chromosome formation. *J. Cell Sci.* **125**, 1591–604 (2012).

62. K. Shintomi *et al.*, Mitotic chromosome assembly despite nucleosome depletion in *Xenopus* egg extracts. *Science (80-.).* **356**, 1284–1287 (2017).

63. K. Shintomi, T. Hirano, The relative ratio of condensin I to II determines chromosome shapes. *Genes Dev.* **25**, 1464–9 (2011).

64. T. Zhang *et al.*, Condensin I and II behaviour in interphase nuclei and cells undergoing premature chromosome condensation. *Chromosome Res.* **24**, 243–69 (2016).

65. A. S. Belmont, J. W. Sedat, D. A. Agard, A three-dimensional approach to mitotic chromosome structure: evidence for a complex hierarchical organization. *J. Cell Biol.* **105**, 77–92 (1987).

66. A. S. Belmont, S. Dietzel, A. C. Nye, Y. G. Strukov, T. Tumbar, Large-scale chromatin structure and function. *Curr. Opin. Cell Biol.* **11**, 307–11 (1999).

67. K. Maeshima, U. K. Laemmli, A Two-Step Scaffolding Model for Mitotic Chromosome Assembly. *Dev. Cell*. **4**, 467–480 (2003).

68. Y. G. Strukov, Y. Wang, A. S. Belmont, Engineered chromosome regions with altered sequence composition demonstrate hierarchical large-scale folding within metaphase chromosomes. *J. Cell Biol.* **162**, 23–35 (2003).

69. K. Nasmyth, Disseminating the Genome: Joining, Resolving, and Separating Sister Chromatids During Mitosis and Meiosis. *Annu. Rev. Genet.* **35**, 673–745 (2001).

70. A. D. Riggs, DNA methylation and late replication probably aid cell memory, and type I DNA reeling could aid chromosome folding and enhancer function. *Philos. Trans. R. Soc. Lond. B. Biol. Sci.* **326**, 285–97 (1990).

71. E. Alipour, J. F. Marko, Self-organization of domain structures by DNA-loop-extruding enzymes. *Nucleic Acids Res.* **40**, 11202–11212 (2012).

72. T. Terekawa *et al.*, The Condensin Complex Is A Mechanochemical Motor That Translocates Along DNA. *bioRxiv* (2017) (available at http://www.biorxiv.org/content/early/2017/05/13/137711).

73. J. Mirkovitch, S. M. Gasser, U. K. Laemmli, Scaffold attachment of DNA loops in metaphase chromosomes. *J. Mol. Biol.* **200**, 101–9 (1988).

74. P. N. Cockerill, W. T. Garrard, Chromosomal loop anchorage of the kappa immunoglobulin gene occurs next to the enhancer in a region containing topoisomerase II sites. *Cell*. **44**, 273–82 (1986).

75. D. Gerlich *et al.*, Condensin I stabilizes chromosomes mechanically through a dynamic interaction in live cells. *Curr. Biol.* **16**, 333–44 (2006).

76. S. H. Yoshimura, T. Hirano, HEAT repeats - versatile arrays of amphiphilic helices working in crowded environments? *J. Cell Sci.* **129**, 3963–3970 (2016).

77. B. Kobe *et al.*, Turn up the HEAT. *Structure*. **7**, R91-7 (1999).

78. E. ROBBINS, N. K. GONATAS, THE ULTRASTRUCTURE OF A MAMMALIAN CELL DURING THE MITOTIC CYCLE. *J. Cell Biol.* **21**, 429–63 (1964).

79. M. Eltsov, K. M. Maclellan, K. Maeshima, A. S. Frangakis, J. Dubochet, Analysis of

cryo-electron microscopy images does not support the existence of 30-nm chromatin fibers in mitotic chromosomes in situ. *Proc. Natl. Acad. Sci. U. S. A.* **105**, 19732–7 (2008).

80. B. J. Wilkins *et al.*, A cascade of histone modifications induces chromatin condensation in mitosis. *Science*. **343**, 77–80 (2014).

81. A. Zhiteneva *et al.*, Mitotic post-translational modifications of histones promote chromatin compaction in vitro. *Open Biol.* **in press** (2017).

82. M. Mazumdar, S. Sundareshan, T. Misteli, Human chromokinesin KIF4A functions in chromosome condensation and segregation. *J. Cell Biol.* **166**, 613–20 (2004).

83. M. Takahashi, T. Wakai, T. Hirota, Condensin I-mediated mitotic chromosome assembly requires association with chromokinesin KIF4A. *Genes Dev.* (2016), doi:10.1101/gad.282855.116.

84. A. Maritan, C. Micheletti, A. Trovato, J. R. Banavar, Optimal shapes of compact strings. *Nature*. **406**, 287–90 (2000).

85. J. Cox, M. Mann, MaxQuant enables high peptide identification rates, individualized p.p.b.-range mass accuracies and proteome-wide protein quantification. *Nat. Biotechnol.* **26**, 1367–72 (2008).

86. B. Schwanhäusser *et al.*, Global quantification of mammalian gene expression control. *Nature*. **473**, 337–42 (2011).

87. J. R. Wiśniewski, M. Y. Hein, J. Cox, M. Mann, A "proteomic ruler" for protein copy number and concentration estimation without spike-in standards. *Mol. Cell. Proteomics*. **13**, 3497–506 (2014).

88. S. G. Landt *et al.*, ChIP-seq guidelines and practices of the ENCODE and modENCODE

consortia. *Genome Res.* **22**, 1813–31 (2012).

89. J. M. Belton *et al.*, Hi-C: A comprehensive technique to capture the conformation of genomes. *Methods*. **58**, 268–276 (2012).

90. B. R. Lajoie, J. Dekker, N. Kaplan, The Hitchhiker's guide to Hi-C analysis: Practical guidelines. *Methods*. **72**, 65–75 (2015).

91. M. Imakaev *et al.*, Iterative correction of Hi-C data reveals hallmarks of chromosome organization. *Nat Methods* (2012), doi:10.1038/nmeth.2148.

92. W. C. Warren *et al.*, A New Chicken Genome Assembly Provides Insight into Avian Genome Structure. *G3*. **7**, 109–117 (2017).

93. Y. Zhang *et al.*, Spatial organization of the mouse genome and its role in recurrent chromosomal translocations. *Cell*. **148**, 908–921 (2012).

94. I. M. Flyamer *et al.*, Single-nucleus Hi-C reveals unique chromatin reorganization at oocyte-to-zygote transition. *Nature*. **544**, 110–114 (2017).

95. J. Kihoon, K. Hong, S. Satchell, *Defining Single Asset Price Momentum in Terms of a Stochastic Process* (2012), vol. 2.

96. P. Eastman *et al.*, OpenMM 7: Rapid development of high performance algorithms for molecular dynamics. *PLoS Comput. Biol.* **13**, e1005659 (2017).

97. P. Eastman, V. S. Pande, Efficient nonbonded interactions for molecular dynamics on a graphics processing unit. *J. Comput. Chem.* **31**, 1268–72 (2010).

98. J. Nuebler, G. Fudenberg, M. Imakaev, N. Abdennur, L. Mirny, Chromatin Organization by an Interplay of Loop Extrusion and Compartmental Segregation. bioRxiv (2017) (available at http://biorxiv.org/content/early/2017/10/03/196261.abstract).

99. J. Molnár et al., The Genome of the Chicken DT40 Bursal Lymphoma Cell Line. G3. 4,

2231–2240 (2014).

Acknowledgements

Supported by grants from the National Human Genome Research Institute (HG003143) and the National Institutes of Health Common Fund (DK107980) to J. Dekker and L. Mirny. J. Dekker is an investigator of the Howard Hughes Medical Institute. Work in the Mirny lab was also supported by the National Science Foundation (Physics of Living Systems, 1504942), and the National Institute of General Medical Sciences (GM114190). Work in the Earnshaw lab was funded by Wellcome, of which W.C.E. is a Principal Research Fellow (Grant 107022). The Wellcome Centre for Cell Biology is supported by core funding from the Wellcome Trust [203149]. M.T.K. was supported by JSPS KAKENHI Grant (16K5095), and research grants from Mochida Memorial Foundation for Medical and Pharmaceutical Research, SGH Foundation, The Sumitomo Foundation, and The Canon Foundation. Sorting of GFP positive and negative cells was performed in the Flow Cytometry facility, Institute of Immunology & Infection Research, Edinburgh with assistance of Dr. Martin Waterfall. We thank Dr. Hakan Ozadam for assistance with Hi-C data processing. All Hi-C data has been submitted to GEO and will be publicly available upon publication (accession number GSE102740).

This paper is dedicated to the memory of Donald S. Coffey, who pioneered the study of chromatin loops in the nucleus.

Author contributions

KS generated cell lines, established cell synchronization protocols, performed synchronized timecourses and performed imaging analyses. JHG and NN performed Hi-C analyses. AG and JN performed polymer simulations. LAM and AG designed and analyzed coarse grained models.

AG analyzed condensin chromatin immunoprecipitation data. LX and JRP prepared 1NM-PP1. IS performed chromatin enriched proteomics analyses. MK provided constructs for cell line engineering. AG, JHG, KS, JN, WCE, LAM and JD designed the project and analyzed data. All contributed to writing the manuscript.

Figure Legends

Fig.0. Summary figure. In prophase, condensins mediate the loss of interphase conformation and loop arrays are formed. In prometaphase, combined action of condensin I and II forms helically arranged nested loop arrays.

Fig. 1. Chromosome morphogenesis during synchronous mitosis. (A) Representative DAPI images of nuclei and chromosomes in CDK1as DT40 cells taken at indicated time points (in minutes) after release from 1NM-PP1-induced G_2 arrest show mitotic chromosome formation. Bar indicates 5 micron. (B) Hi-C interaction maps of chromosome 7 (binned at 100 kb) from cells collected indicated time points in prophase and prometaphase show large-scale changes in contact frequencies as cell progress through mitosis (C) The average interaction maps center around G_2 TAD boundaries. TAD boundaries disappear. (D) Compartmentalization saddle plots: average distance-normalized interaction frequencies between cis-pairs of 100-kb bins arranged by their G_2 eigenvector value. Compartments disappear.

Fig. 2. Prophase chromosomes fold as axially compressed loop arrays. (A) Genome-wide curves of contact frequency *P(s)* vs genomic distance *s*, normalized to unity at *s*=100 kb. The curves are derived from prophase Hi-C data at the indicated time points after release from G_2 arrest. The

dotted line indicates $P(s) = s^{-0.5}$ observed for mitotic chromosomes *(8)*. (B) Overview of the coarse grained model of prophase chromosomes. The chromosome is compacted into a series of consecutive loops and compressed into a cylindrical shape. The loop bases form a scaffold at the chromosomal axis, each loop occupies a cylindrical sector of height h and angular size φ, oriented at angle Θ_i. The coarse-grained model predicts the *P(s)* curve to have three distinct regions: an intra loop (I), intra layer (II) and inter layer (III) regions. (C) The best fitting *P(s)* predictions by the coarse grained model for late prophase (t = 7.5 minutes) under two different assumptions on loop orientations: (top panels) uncorrelated and (bottom panels) correlated orientations of consecutive loops. Uncorrelated angular loop orientations lead to a plateau in *P(s)* in the intra-layer, whereas correlated angles lead to the experimentally observed $P(s) = s^{-0.5}$ (right panels). (D) Polymer models of prophase chromosomes. Chromatin fibers are modeled as chains of particles (dark grey circles), compacted into arrays of consecutive loops (loop bases indicated in orange). Chromosomes are compacted into a cylinder with a density of one nucleosome per 11x11x11nm cube (lower right). (E) Goodness of fit for simulated vs experimental *P(s)*. Polymer simulations were performed for a range of loop densities and loop lengths, and for each simulation *P(s)* was calculated. The heatmap shows the quality of a match between the predicted and experimental *P(s)* curves at late prophase (t = 7.5 minutes). (F) *P(s)* derived from late prophase Hi-C experiments (green line) and the best fitting polymer models (grayscale lines). Average loop size and linear density of loops along the chromosome axis are listed.. (G) Top and side view of the best fitting polymer model of late prophase chromosomes. Loops bases are shown in red and several loops rendered in different colors. (H) The average loop size and linear density of the 3 best-fitting models of prophase chromosomes at different time points.

Fig. 3. Helical organization of prometaphase chromosomes. (A) Genome-wide curves of contact frequency *P(s)* vs genomic distance (separation, *s*), normalized to unity at *s*=100 kb. The curves are derived from Hi-C data obtained from prometaphase cells (t = 10-60 minutes after release from G_2 arrest). The dashed line indicates $P(s) = s^{-0.5}$. Arrows indicate positions of a local peak in *P(s)* representing the second diagonal band observed in Hi-C interaction maps. (B) The coarse grained model of prometaphase chromosomes with staircase loop arrangement. Left, top: the staircase loop arrangement implies that loops rotate in genomic order around a central scaffold (see Supplemental Materials). Left, bottom: angles of adjacent loops are correlated and steadily increasing, reflecting helical arrangement of loops. Right: this helical arrangement can be observed as gyres by DNA staining and a helical scaffold can be observed in cells expressing GFP-tagged condensins. (C) The best fitting *P(s)* predictions by the staircase coarse grained model for late prometaphase t = 30 minutes (30min; left panel) and t = 60 minutes (60min, right panel) after release from G_2 arrest (Hi-C data: colored lines; model; gray lines). (D) Polymer model of prometaphase chromosomes. Chromosomes are modeled as arrays of consecutive nested loops with a helical scaffold (outer loops in red, inner loops in blue, also indicated diagrammatically bottom right). (E) Goodness of fit for simulated vs experimental *P(s)*. Polymer simulations were performed varying the helix height (nm), the size of a helical turn (Mb), and the sizes of inner and outer loops. For each simulation *P(s)* was calculated. The heatmaps show the quality of the best match between the predicted and experimental *P(s)* at prometaphase (t = 30 minutes), when two out of four parameters were fixed to the specified values. (F) *P(s)* derived from prometaphase Hi-C experiments (colored lines) and the best fitting polymer models (gray lines). Left panel: t = 30 minutes, right panel t = 60 minutes after release from G_2 arrest. Average size of outer and inner loops, the length of a helix turn and the helical pitch are indicated. (G)

Parameters of the helical scaffolds from the best fitting polymer models. X-axis: ratio of the radius of the helical scaffold to that of the whole chromatid; Y-axis: ratio of the pitch to the helix radius. The dashed lines show the corresponding values (0.46 and 2.5122) for the optimal space-filling helix (*84*). Classical solenoid configurations are predicted to be in sector III, while the "spiraling staircase" configurations are in I and II. On the right, three examples of models of type I, II and III are shown with loops bases in red and several individual loops rendered in different colors. Also shown is a schematic of a prometaphase chromosome with the helical winding of loops indicated by arrow around the loop array. (H) Parameters of the best 3 models of prometaphase chromosomes at different time points.

Fig. 4. Defects in chromosome morphogenesis in condensin depleted cells. (A-C). Hi-C interaction frequency maps (binned at 100 kb) for chromosome 7 at indicated time points (top right in each heatmap) after release from G_2 arrest. The first plot below each Hi-C interaction map displays the compartment signal (Eigenvector 1). The bottom graph shows the insulation score (TADs; binned at 50 kb). (A) SMC2-mAID cells were treated with auxin for three hours prior to release from G_2 arrest to deplete SMC2. SMC2+: Hi-C interaction map for G_2-arrested cells prior to auxin treatment. SMC2-: Hi-C interaction map for G_2-arrested cells after three hours of auxin treatment. (B) Hi-C data for CAP-H2-mAID cells treated for three hours with auxin prior to release from G_2 arrest to deplete CAP-H2. (C). Hi-C data for CAP-H-mAID cells treated for three hours with auxin prior to release from G_2 arrest to deplete CAP-H.

Fig. 5. Distinct roles for condensin I and II in mitotic chromosome formation. (A) Genome-wide curves of contact frequency *P(s)* vs genomic distance *s*, normalized to unity at *s*=100 kb. The

curves are *P(s)* derived from Hi-C data obtained from CAP-H2-depleted (left panel) and CAP-H-depleted cells (right panel), at t = 7-60 minutes after release from G_2 arrest. Dashed line indicates $P(s) = s^{-0.5}$. (B) Overlayed *P(s)* curves of WT, CAP-H- and CAP-H2-depleted chromosomes show independent contributions of two condensin complexes to short- and long-distance contacts. (C) Polymer models of CAP-H2 (top) and CAP-H (bottom) depleted chromosomes. Top: depletion of CAP-H2 is modeled via removal of outer loops and relaxation of the helix.. Bottom: depletion of CAP-H is modeled via removal of the inner loops, while preserving the helical arrangement of the scaffold. Condensin II loop anchors are shown in red, condensin I loop anchors are shown in blue. (D) *P(s)* derived from late prometaphase CAP-H2 depletion Hi-C experiments (red line) and the three best fitting polymer models (grayscale lines). The average loop size and linear density of loops along the chromosome axis are indicated. (E) The average loop size and linear DNA density of the 3 best-fitting models of CAP-H2-depleted chromosomes at different time points. (F) *P(s)* derived from late prometaphase CAP-H depletion Hi-C experiments (blue line) and the best fitting polymer models with and without nested inner loops (grayscale lines). The average size of outer and inner loops, the length of a helix turn in Mb and the helical pitch are indicated. (G) The best fitting *P(s)* predictions by the staircase coarse grained model for late prometaphase CAP-H depletion Hi-C experiments at t = 30 minutes after release of G_2 arrest (gray lines; experimental P(s): red lines. Top: loop size is 200 kb, bottom: loop size is 400 kb.

Fig. 6. A mitotic chromosome morphogenesis pathway. In prophase, condensin II compacts chromosomes into arrays of consecutive loops and sister chromatids split along their length. The scaffold of condensin II-mediated loop bases is indicated in red. Upon nuclear envelope

breakdown and entry into prometaphase, condensin II-mediated loops become increasingly large as they split into smaller ~80 kb loops by condensin I. Chromosomes are shown as arrays of loops (only inner loops can be observed microscopically; top: cross-section, bottom: side view. For clarity, loops are indicated as separate entities pointing in one direction, while in reality loops are unstructured and can mix). The nested arrangements of centrally located condensin II-mediated loop bases and more peripherally located condensin I-mediated loop bases are indicated in red and blue respectively. During prometaphase central scaffold acquires a helical arrangement with loops rotating around the scaffold as steps in a “spiral staircase” (helical path of loops is indicated by arrows). As prometaphase progresses outer loops grow and the number of loops per turn increases and chromosomes shorten to form the mature mitotic chromosome.

Fig.0

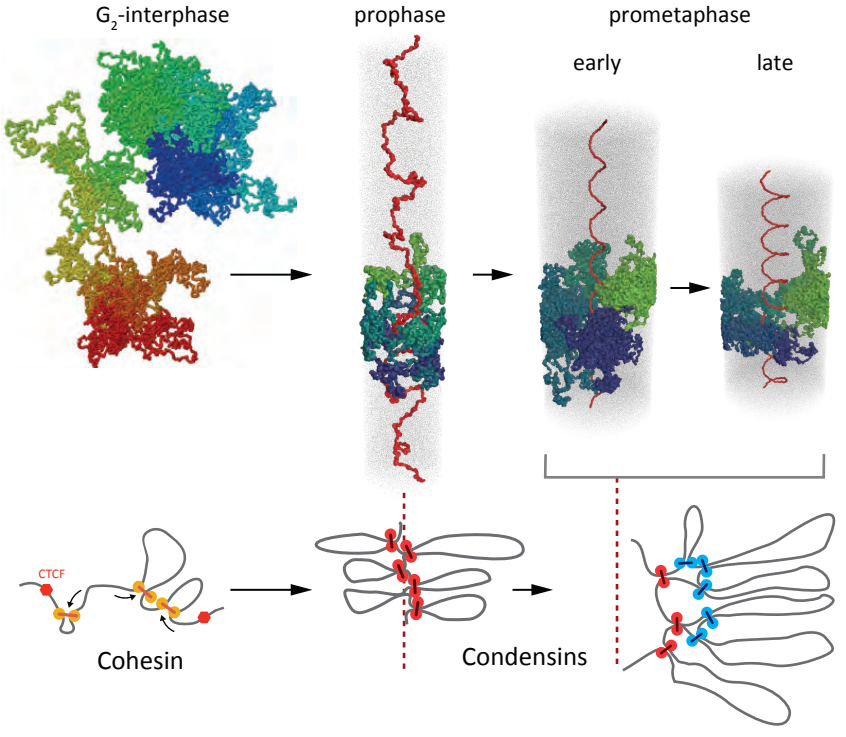
G2-interphase
prophase
prometaphase
early
late
CTCF
Cohesin
Condensins

Fig.1

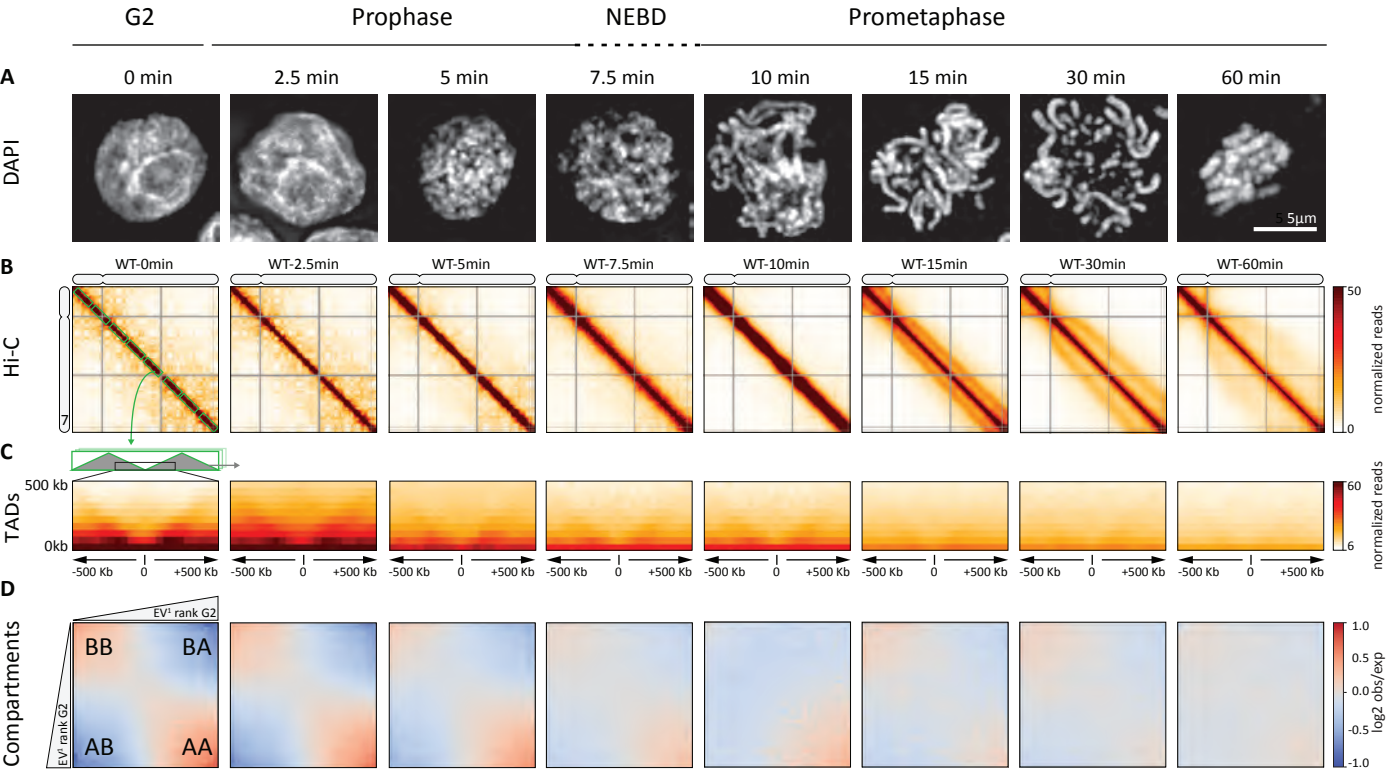
G2
Prophase
NEBD
Prometaphase
A
0 min
2.5 min
5 min
7.5 min
10 min
15 min
30 min
60 min
DAPI
5 5µm
B
WT-0min
WT-2.5min
WT-5min
WT-7.5min
WT-10min
WT-15min
WT-30min
WT-60min
Hi-C
7
50
0
normalized reads
C
TADs
500 kb
0kb
-500 Kb
0
+500 Kb
60
6
normalized reads
D
Compartments
EV¹ rank G2
EV² rank G2
BB
BA
AB
AA
1.0
0.5
0.0
-0.5
-1.0
log2 obs/exp

Fig.2

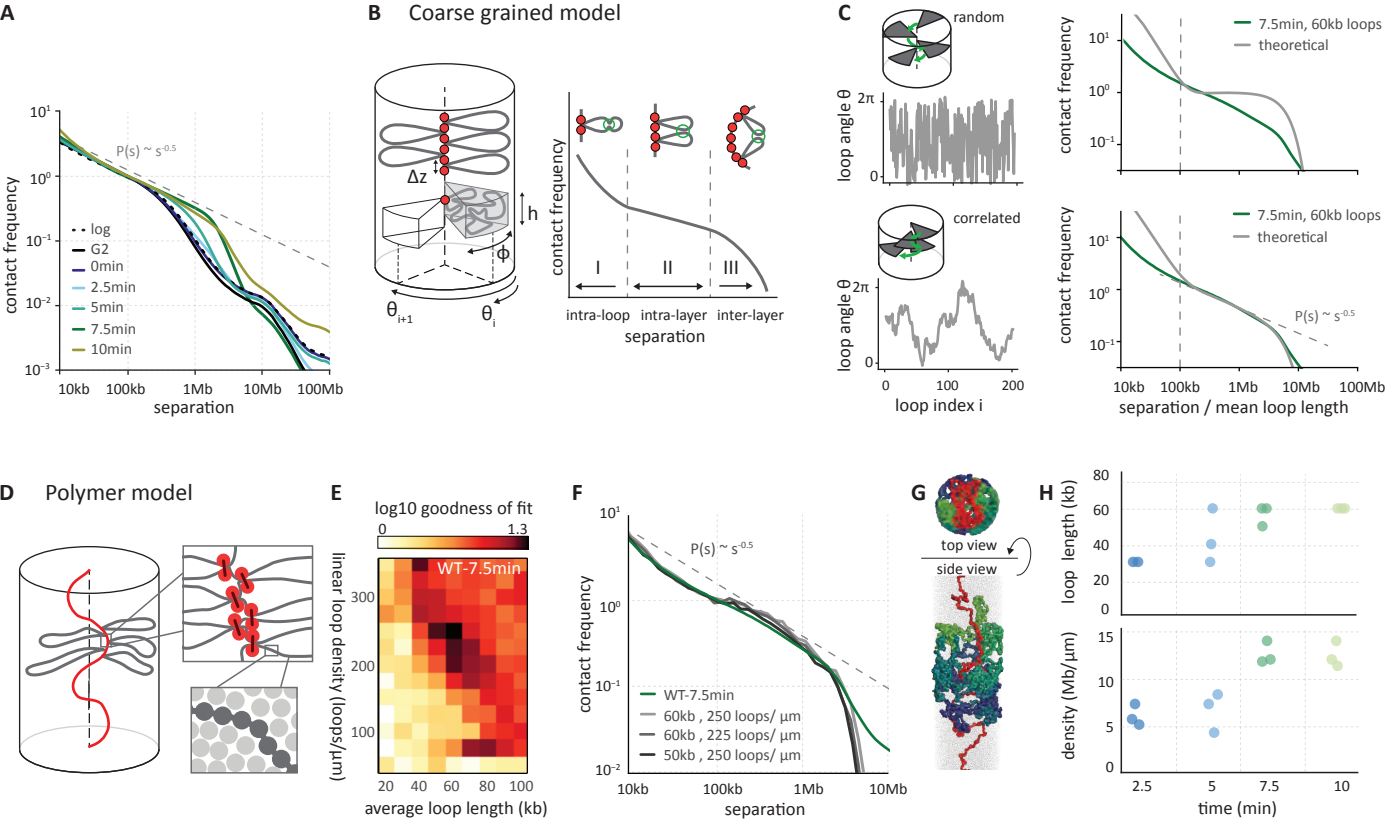
A
contact frequency
P(s) ~ s^-0.5
log
G2
0min
2.5min
5min
7.5min
10min
10kb
100kb
1Mb
10Mb
100Mb
separation
B
Coarse grained model
Δz
h
Φ
θi+1
θi
contact frequency
I
II
III
intra-loop
intra-layer
inter-layer
separation
C
random
loop angle θ
2π
0
correlated
0
100
200
loop index i
contact frequency
7.5min, 60kb loops
theoretical
P(s) ~ s^-0.5
separation / mean loop length

D
Polymer model
E
log10 goodness of fit
0
1.3
WT-7.5min
linear loop density (loops/μm)
average loop length (kb)
F
contact frequency
P(s) ~ s^-0.5
WT-7.5min
60kb , 250 loops/ μm
60kb , 225 loops/ μm
50kb , 250 loops/ μm
separation
G
top view
side view
H
loop length (kb)
density (Mb/μm)
time (min)

Fig.3

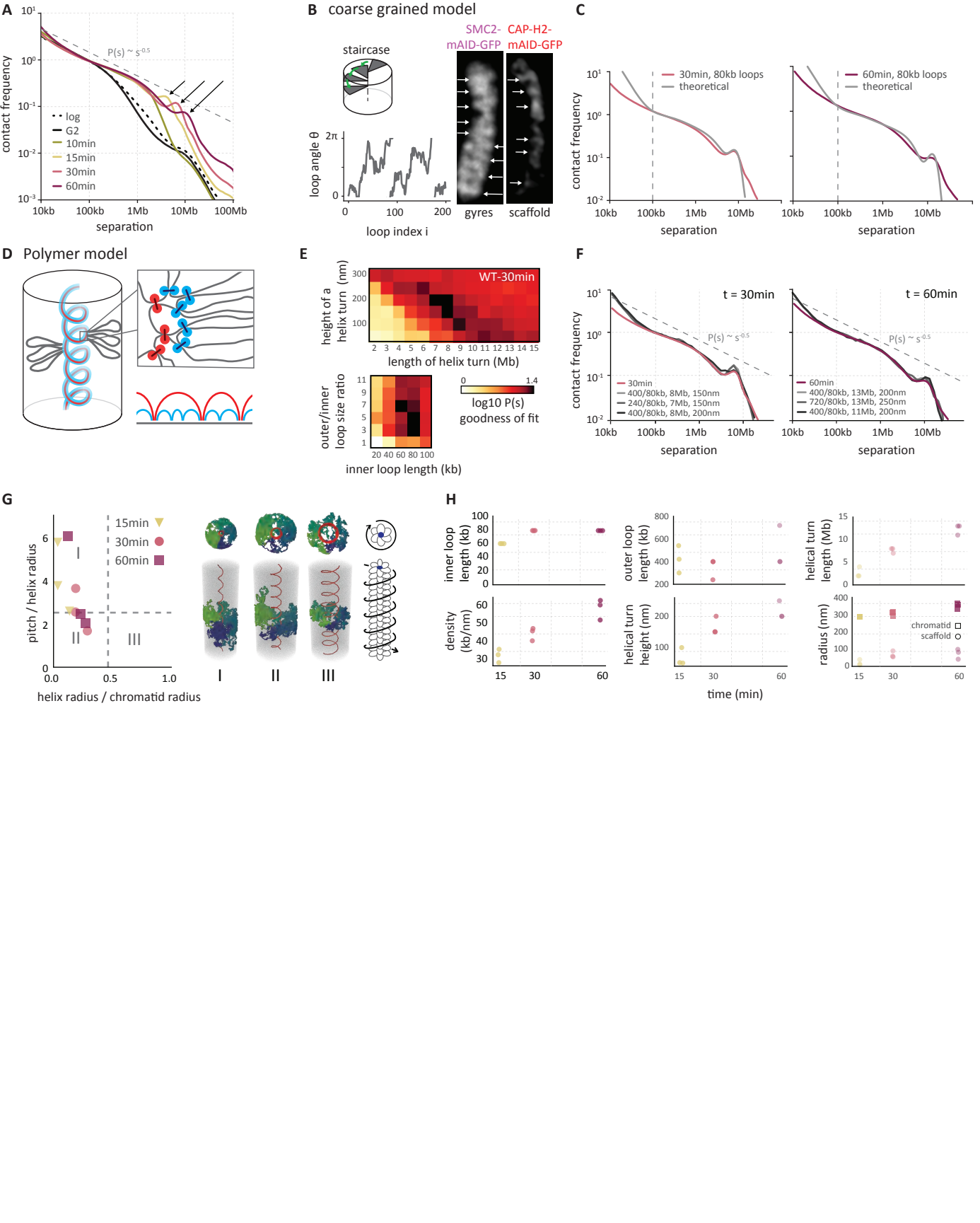
A
contact frequency
P(s) ~ s^-0.5
log
G2
10min
15min
30min
60min
separation
B coarse grained model
staircase
SMC2-mAID-GFP
CAP-H2-mAID-GFP
loop angle θ
2π
loop index i
gyres
scaffold
C
30min, 80kb loops
theoretical
60min, 80kb loops
theoretical
D Polymer model
E
WT-30min
height of a helix turn (nm)
length of helix turn (Mb)
outer/inner loop size ratio
inner loop length (kb)
log10 P(s) goodness of fit
F
t = 30min
t = 60min
30min
400/80kb, 8Mb, 150nm
240/80kb, 7Mb, 150nm
400/80kb, 8Mb, 200nm
60min
400/80kb, 13Mb, 200nm
720/80kb, 13Mb, 250nm
400/80kb, 11Mb, 200nm
G
15min
30min
60min
pitch / helix radius
helix radius / chromatid radius
H
inner loop length (kb)
outer loop length (kb)
helical turn length (Mb)
density (kb/nm)
helical turn height (nm)
radius (nm)
chromatid
scaffold
time (min)

Fig.4

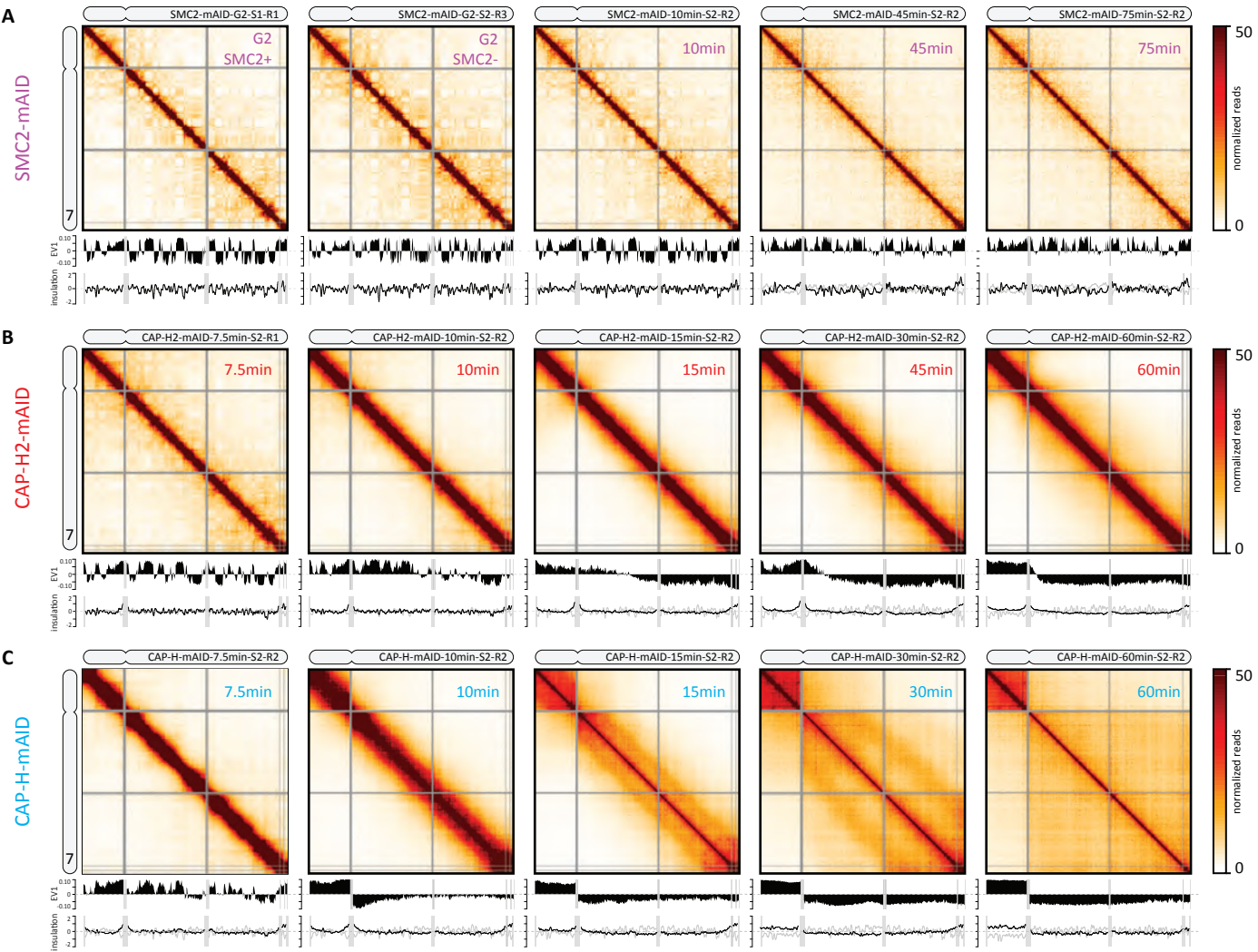
A
SMC2-mAID
SMC2-mAID-G2-S1-R1
SMC2-mAID-G2-S2-R3
SMC2-mAID-10min-S2-R2
SMC2-mAID-45min-S2-R2
SMC2-mAID-75min-S2-R2
G2
SMC2+
G2
SMC2-
10min
45min
75min
B
CAP-H2-mAID
CAP-H2-mAID-7.5min-S2-R1
CAP-H2-mAID-10min-S2-R2
CAP-H2-mAID-15min-S2-R2
CAP-H2-mAID-30min-S2-R2
CAP-H2-mAID-60min-S2-R2
7.5min
10min
15min
45min
60min
C
CAP-H-mAID
CAP-H-mAID-7.5min-S2-R2
CAP-H-mAID-10min-S2-R2
CAP-H-mAID-15min-S2-R2
CAP-H-mAID-30min-S2-R2
CAP-H-mAID-60min-S2-R2
7.5min
10min
15min
30min
60min
normalized reads
50
0
EV1
insulation

Fig.5

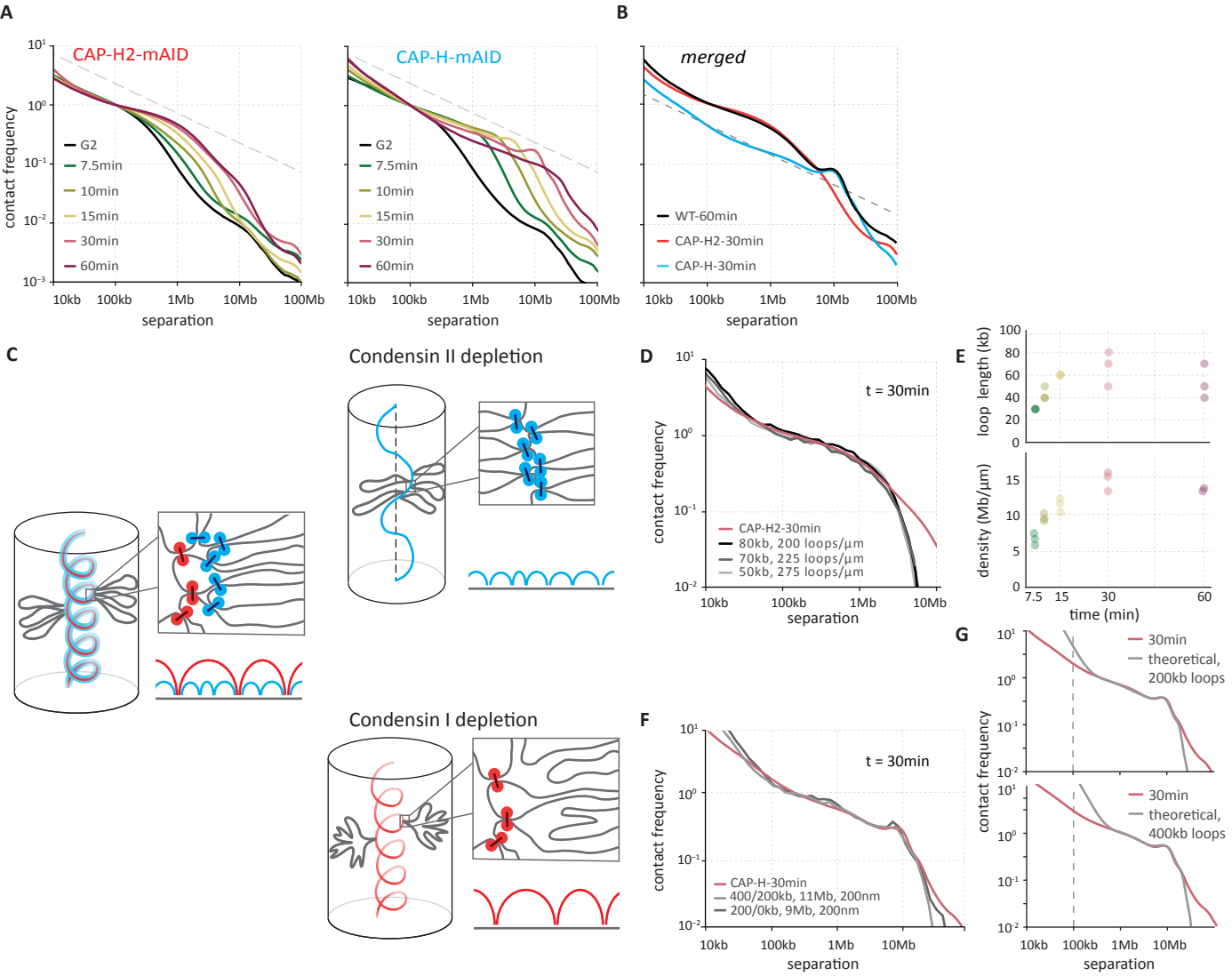
A
CAP-H2-mAID
CAP-H-mAID
contact frequency
G2
7.5min
10min
15min
30min
60min
10kb
100kb
1Mb
10Mb
100Mb
separation
B
merged
WT-60min
CAP-H2-30min
CAP-H-30min
C
Condensin II depletion
Condensin I depletion
D
t = 30min
CAP-H2-30min
80kb, 200 loops/μm
70kb, 225 loops/μm
50kb, 275 loops/μm
E
loop length (kb)
density (Mb/μm)
time (min)
F
t = 30min
CAP-H-30min
400/200kb, 11Mb, 200nm
200/0kb, 9Mb, 200nm
G
30min
theoretical,
200kb loops
400kb loops

Fig.6

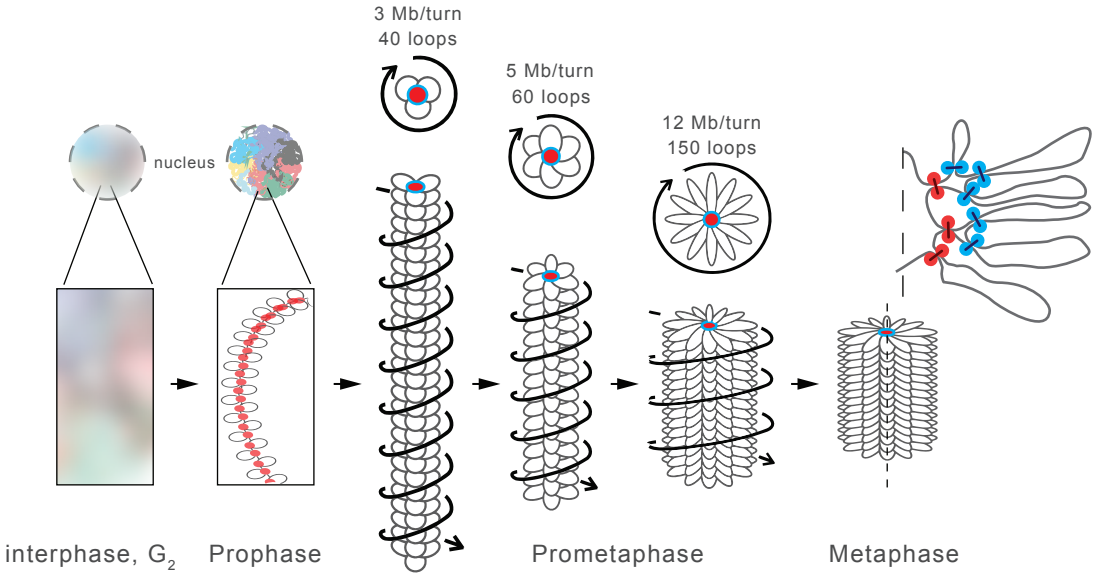
3 Mb/turn
40 loops
5 Mb/turn
60 loops
12 Mb/turn
150 loops
nucleus
interphase, G2
Prophase
Prometaphase
Metaphase

Supplementary Materials

Materials and Methods

Figures S1-S27

Tables S1-S4

Movie S1

References (*85-99*)

Supplementary Materials for

A Pathway for Mitotic Chromosome Formation

Johan H. Gibcus[1*], Kumiko Samejima[2*], Anton Goloborodko[3*$], Itaru Samejima[2], Natalia Naumova[1], Johannes Nuebler[3], Masato Kanemaki[4], Linfeng Xie[5], James R. Paulson[5], William C. Earnshaw[2#], Leonid A. Mirny[3#], Job Dekker[1,6#]

correspondence to: WCE: bill.earnshaw@ed.ac.uk; LAM: Leonid@MIT.edu; JD: Job.Dekker@umassmed.edu

This PDF file includes:

Other Suplementary Materials for this manuscript includes the following:

Materials and Methods

Cell culture

Chicken DT40 (B-cell lymphoma) cells were cultured in RPMI 1640 medium supplemented with 10 % fetal bovine serum and 1% chicken serum at 39°C in 5% CO2 in air.

Stable transfection into DT40 cells was performed as described previously (*23*). Transient transfection into DT40 cells was performed using a Neon transfection system from ThermoFisher Scientific. 2-4 million cells suspended in 100 µl 1X buffer R were mixed with plasmid DNA (4-10 µg), then electroporated at setting 5.

Doxycycline (BD) dissolved in water (1mg/ml) was added to a final concentration of 0.5 µg/ml. For G_2 arrest, 1NM-PP1 dissolved in DMSO (10 mM) was added to cultures at a final concentration of 2 µM. Degradation of AID-containing proteins was induced by addition of a 50 mM solution of Indole-3-acetic acid (auxin, Fluka) dissolved in ethanol to a final concentration of 125 µM. To prevent cells from entering anaphase, Nocodazole (Sigma-Aldrich) dissolved in DMSO at 1 mg/ml was added to some cultures to a final concentration of 0.5 µg/ml (see details below, **Table S1**).

Cell lines

A summary of the cell lines described below can be found in **Table S3**.

SMC2-AID-GFP cells: SMC2-AID-GFP cells were derived from a previously described SMC2 conditional (doxycycline induced) knockout cell line (*54*). Plasmids coding SMC2-mAID-GFP and OsTIR1 were randomly integrated into the DT40 genome. A 3.8 kb fragment of the endogenous GgSMC2 promoter (*54*) drove expression of the GgSMC2 cDNA fused with a minimal AID (mAID) tag (AtIAA1765-132) and GFP tag (SMC2-mAID-GFP) at the C-terminus. A CMV promoter drove the expression of plant-specific F-box protein OsTIR1 linked to a MmDHFR cDNA by a T2A peptide (synthesized at Thermofisher Scientific and cloned into pCDNA3). 10 µM Methotrexate (MTX) was used to select cells expressing high levels of MmDHFR and OsTIR1. The resultant cell lines (named SMC2-AID-GFP) were cultured continuously in the presence of doxycycline (0.5 µg/ml) to suppress the expression of non-tagged GgSMC2 protein.

CAP-H-AID-GFP cells: Plasmids encoding CAP-H-mAID-GFP and plant specific F-box protein OsTIR1 were randomly integrated into the genome of a CAP-H conditional (doxycycline induced) knockout cell line (*61*). A CMV promoter drove the expression of the GgCAP-H-mAID-GFP. A CMV promoter drove the expression of OsTIR1 linked to a MmDHFR cDNA by a T2A peptide (synthesized at Thermofisher Scientific and cloned into pCDNA3). 10 µM Methotrexate (MTX) was used to select cells expressing high levels of MmDHFR and OsTIR1. The resultant CAP-H-AID-GFP cell lines were cultured continuously in the presence of doxycycline (0.5 µg/ml) to suppress the expression of non-tagged GgCAP-H protein.

CAP-H2-AID-GFP cells: CAP-H2-AID-GFP cells were constructed starting with wild type DT40 cells. A codon-optimized GgCAP-H2 cDNA was synthesized (Thermofisher Scientific) and cloned into pAID2.3C so that CAP-H2 was tagged with mAID and GFP at its C-terminus. A CMV promoter drove the co-expression of OsTIR1 and CAP-H2-mAID-GFP, which are linked by a P2A peptide in the pAID2.3C-CAP-H2 plasmid. The pAID2.3C-CAP-H2 plasmid was randomly integrated into the DT40 genome. The endogenous GgCAP-H2 gene was then

inactivated by transient transfection of plasmids encoding hCas9 cDNA and GgCapH2 guide RNA (Thermofisher Scientific). The target sequence of guide RNA was CCTATACTCGCTGGTCTACCAGG.

CDK1as cells: A CMV promoter drove the expression of a XlCdk1as cDNA (*22*) linked to a puromycin or zeocin resistance gene via a T2A peptide. This construct was integrated at random in the genome of the desired target cell line. The endogenous GgCdk1 gene was then inactivated by transient transfection of plasmids encoding hCas9 cDNA (Addgene #41815) and GgCdk1 guideRNA (based on Addgene #41824). The target sequence of the guide RNA was AAAATACGTCTAGAAAGTG. SMC2-AID-GFP cells, CAP-H-AID-GFP cells and CAP-H2-AID-GFP cells were individually converted into CDK1as cell lines by this method. Wild type CDK1as cells were a gift of Helfrid Hochegger (University of Sussex) (*22*).

Detailed protocols to establish DT40-AID/CDK1as cell lines are available upon request to Dr. Kumiko Samejima.

Time course experiments

Typically 1-3 x10^7 CDK1as wild type cells/sample were treated with 1NM-PP1 (final concentration: 2 μM) for 10 h, after which over 95% were in G_2 (**Table S1**). G_2-arrested cells were collected prior to 1NM-PP1-washout. To release cells from the G_2 arrest, 1NM-PP1 was washed out by collecting the cells by centrifugation (1300 rpm, 2-5 min - depending on the volume of cultured cells - at RT) and suspending the cells in fresh media (10-20 ml). Cells were washed twice over a period of 10-20 minutes (this varied depending on the number of cultures being processed simultaneously). These cells were suspended in fresh media and divided into flasks (one flask for each time point, typically 1-3 x10^7 cells per flask) and returned to the incubator (counted as t = 0 minutes). At each time point (0, 2.5, 5, 7.5, 10, 30, 45, 60, 75 minutes), a flask was removed from the incubator and cells with media were transferred to a 50 ml Falcon tube, which was topped up with fresh media to 45 ml.

Three ml of 16% formaldehyde solution was added to the 50 ml tube to obtain a final concentration of 1%. The content was quickly mixed by inverting the tube twice and left at RT for 10 min for cross-linking. 2.5 ml of 2.5 M glycine was then added to the tube to stop cross-linking. The content was quickly mixed by inverting the tube twice and left at RT for 5 min, and then on ice for at least 15 min. Subsequently, cells were collected by centrifugation (2000 rpm, 10 min), and the cell pellet was frozen on dry ice and then stored at -80°C.

Modifications to the time course experiment

Auxin-induced protein depletion

Where required, auxin was added after 10 h 1NM-PP1 treatment and cells (SMC2-mAID-GFP cells, CAP-H-mAID-GFP cells, CAP-H2-mAID-GFP cells) were further incubated for 3 hours to deplete AID-tagged proteins. Cells were then released from the G_2 arrest as described above, except that auxin was kept in the 1NM-PP1 washout media and in the media during all further incubations. Note that the G2 cells for CAP-H-mAID-GFP and CAP-H2-mAID-GFP are either GFP-negative (degron active) or GFP-positive (degron not activated), depending on auxin addition (indicated in **Tables S1**, **S2)**.

Cell sorting to isolate cells depleted of target proteins

As a control, in some cases (indicated as “sorted”) SMC2-AID-GFP cells were FACS-sorted after cross-linking to exclude residual GFP-positive cells, which had not responded fully

to auxin. Some wild type cells were also sorted. Sorting did not alter the Hi-C data as compared to unsorted cells, indicating that degron-mediated protein degradation was very efficient (**Fig. 4A, Fig.S8 (set #4) and Fig.S20A (set #1**).

Nocodazole addition to prevent anaphase entry

Nocodazole was added for 30 minutes prior to 1NM-PP1 washout only for the $t \geq 30$ minute time points (Replicate 1 of WT) or for $t \geq 60$ minutes samples (all other time courses; **Table S1**). Nocodazole was present in 1NM-PP1 washout media and in the media during further incubations. No nocodazole was added for cells collected at any of the other time points.

Microscopy on fixed cells

Fixation of chromosomes from mitotic cells

Cells in media (200 µl) were directly fixed in 1 ml of ice-cold Methanol/Acetic acid solution (3:1) for > 30 minutes. Fixed Cells were centrifuged at 2000 g for 1 min, applied on slides, air dried, and stained with DAPI in Vectashield antifade mounting medium (H-1200, Vectashield). Images were taken by DeltaVision microscopy.

Lamin B1 and Histone H3 Phos-Ser10 staining

Cells were fixed in pre-warmed 4% Formaldehyde/PBS for 10 min and permeabilized with 0.15% triton for 5 minutes. The following steps were then performed at RT. Cells were blocked with 5% BSA/PBS for 30 minutes. Anti-lamin B1 mouse monoclonal antibody (1:100, Zymed) and Anti-histone H3 phospho-Ser10 rabbit polyclonal antibody (1:500, Millipore) diluted in the blocking buffer were applied to the cells for 1 hour. Cells were washed with PBS 3x for 5 minutes. Secondary antibodies (Molecular Probes, ThermoFisher Scientific) anti-mouse and anti-rabbit coupled with Alexa Fluor 488 and 594, respectively and diluted 1:500 and 1:1000 in the blocking buffer, were applied to the cells for 30 minutes. Cells were washed with PBS three times for 5 minutes. DNA was stained with Hoechst 33452 and mounted with Prolong diamond (Molecular Probes, ThermoFisher Scientific). Images were taken by DeltaVision microscopy.

DeltaVision microscopy

3D datasets were acquired using a cooled CCD camera (CoolSNAP HQ; Photometrics) on a wide-field microscope (DeltaVision Spectris; Applied Precision) with a 100× NA 1.4 Plan Apochromat lens. The datasets were deconvolved with softWoRx (Applied Precision), converted to Quick Projections in softWoRx, exported as TIFF files, and imported into Adobe Photoshop for final presentation.

Chromosome length measurements

Samples were prepared essentially by the same method used for Hi-C samples. WT/CDK1as cells were treated with 1NMPP1 for 10 hours. After 1NM-PP1 washout, cells were plated on poly-L-lysine coated coverslips and incubated with the corresponding media for either 30 or 60 minutes. Then the cells were rinsed with PBS and fixed with 1% formaldehyde in PBS. Note: Nocodazole was added to the culture 30 minutes prior to 1NM-PP1 washout and kept in the culture thereafter. MG132 was added to the culture at t = 30 minutes after release and cells were fixed 30 minutes after that. Ten or more pictures were taken for each condition using the Zeiss Airyscan microscope and analysed using IMARIS.

We measured the length and width of the longest chromosomes in DT40 cells fixed with 1% formaldehyde solution as used in the preparation of Hi-C specimens. It was not possible to measure all chromosomes in cells fixed under these Hi-C conditions, so by choosing the longest chromosome in each cell, we could be confident that we were measuring and comparing the same chromosome (chromosome 1). In order to identify chromosome 1 in each mitotic cell, we measured the length of several candidate chromosomes in each cell using IMARIS to track that chromosome through the three-dimensional data set. The measurement reported was for the longest chromosome. In order to calculate the chromosome width in each cell, avoiding centromeres and telomeres, we measured the width of the longest chromosome at 5 different positions.

Visualization of a repeating structure on chicken mitotic chromosomes

Asynchronously growing WT/CDK1as, SMC2-mAID-GFP/CDK1as, CAP-H-mAID-GFP/CDK1as, CAP-H2-mAID-GFP/CDK1as, CAP-H-GFP/CDK1as cells were treated with colcemid (100 ng/ml) for 2.5 hours. Cells were treated with 75 mM KCl for 5 minutes then fixed with ice-cold Methanol/Acetic acid. Cells were spread on coverslips, mounted with vectashield containing DAPI (Vectashield). 3D datasets were acquired using a cooled CCD camera (CoolSNAP HQ; Photometrics) on a wide-field microscope (DeltaVision Spectris; Applied Precision) with a 100× NA 1.4 Plan Apochromat lens. The datasets were deconvolved with softWoRx (Applied Precision), converted to Quick Projections in softWoRx, exported as TIFF files, and imported into Adobe Photoshop for final presentation.

This hypotonic treatment and spreading procedure caused a reorganization of the chromosome structure that appears to reveal the underlying helical organization of the chromosome scaffold. This helical organization is not seen in minimally perturbed chromosomes fixed with formaldehyde, as used for our Hi-C studies, and where the chromatin distribution appears to be uniform. In the chromosome spreads, we could unambiguously identify chromosomes 1 and 2 and could count the number of gyres, and therefore calculate the amount of DNA per gyre. This number is almost certainly an overestimate, because we did not see gyres at centromeres or telomeres. For Chromosome 1 we counted 10.5 ± 3.8 gyres, yielding 18.7 MB/gyre (n = 19 chromosomes). For chromosome 2 we counted 8.5 ± 2.4 gyres, yielding 17.7 Mb/gyre (n = 17 chromosomes). We note that these chromosomes had been arrested in mitosis for up to 2.5 hours with a colcemid block, so they would be expected to be more compacted than the 60 minute time point analyzed by Hi-C.

Helical distribution of GFP signal in single sister chromatids

SMC2-mAID-GFP/CDK1as, CAP-H-mAID-GFP/CDK1as, CAP-H2-mAID-GFP/CDK1as, CAP-H-GFP/CDK1as cells were treated with 2 µM 1NM-PP1 for 4h without auxin. Cells were plated on poly-lysine coated coverslips immediately after 1NM-PP1 washout and incubated for 40 minutes. The cells were then fixed with 4% Formaldehyde/PBS for 10 minutes, permeabilized with 0.15 % Triton/PBS for 5 minutes, stained with Hoechst solution, mounted with Prolong Diamond antifadant and imaged using the Airyscan module on a Zeiss LSM 880 confocal, using a x100 alpha Plan-Apochromat objective. Hoechst 33342 was detected using a 405 nm Diode laser and a 420-480 nm bandpass emission filter, Alexa488 was detected using the 488 nm line of an Argon laser and a 495-550 nm bandpass emission filter, Step size for Z stacks was set to 0.145 µm. 3D datasets were visualized and analyzed using Imaris V8.4 (Bitplane, Oxford Instruments, Oxfordshire, UK). Images show single sections from three-dimensional data stacks

and are representative of two biological replicate experiments. Cells had been arrested in mitosis for up to 2.5 hours with a colcemid block, so they would be expected to be more compacted than the 60 minute time point analyzed by Hi-C.

Immunoblot analysis

Typically 0.5-1 x 10^6 cells were loaded in each lane of a 7.5 % SDS-PAGE gel. Proteins were transferred to PVDF membranes at 200 mA for 2.5 hours in transfer buffer containing 119 mM Tris (pH 8.5), 40 mM glycine, 0.1% SDS, and 20% Methanol. Membranes were blocked with 5% skimmed milk in PBS (154 mM NaCl, 1.5 mM KH_2PO_4, 5.5 mM Na_2HPO_4) for 30 minutes, then incubated with relevant primary antibodies recognizing α-tubulin (1:2000, DM1A, Sigma-Aldrich; as a loading control), SMC2 (1:1000) (*17*), or GFP (1:1000) (gift from Simona Saccani, University of Edinburgh) with 1% skimmed milk in PBS/tween20 (1%) for 3 hours up to overnight. Membranes were washed three times for 5 minutes with PBS/tween20 (1%). Membranes were incubated with IRDye-labeled secondary antibodies diluted in 1% skimmed milk in PBS/tween20 (1%) (1:10,000) for 45 minutes followed by three 5 minute washes with PBS/tween20 (1%). Membranes were kept in PBS until fluorescence intensities were determined using a CCD scanner (Odyssey; LI-COR Biosciences) according to the manufacturer's instructions.

Flow cytometry analysis

DNA content: Cells were suspended overnight in ice-cold 70% ethanol. The next morning, cells were rinsed with PBS then re-suspended in PBS containing 100 µg/ml RNase A and 5 µg/ml propidium iodide. Samples were then analyzed using a FACSCalibur flow cytometer following the manufacturer's instructions. Data was analyzed using FlowJo V10.3. WT cells were gated for viability based on forward and side scatter (FSC/SSC), from which single cells were selected based on FSC height (H) and width (W). These gates were applied to all samples and DNA content was plotted as a histogram of FSC-H.

Chromatin Enrichment for Proteomics (ChEP)

Synchronized Cdk1as cells were crosslinked with 1% formaldehyde at specified time points in mitosis and chromatin was extracted from the crosslinked cells by the ChEP protocol (*58*). Briefly, 5 x 107 cells were fixed for 10 minutes by addition of formaldehyde to the cell culture. Formaldehyde was quenched by 125 mM glycine for 5 minutes. Crosslinked cells were washed with TBS (20 mM Tris pH 7.4, 150 mM NaCl) and frozen in liquid nitrogen. Cells were lysed on ice in Lysis buffer (25 mM Tris pH 7.4, 0.1% Triton X-100, 85 mM KCl, protease inhibitors: 1 mM PMSF, 1 µg/ ml each of chymostatin, leupeptin, antipain, pepstatin A). Cells were washed with Lysis buffer and the pellet was resuspended in 300 µl SDS buffer (50 mM Tris pH 7.4, 10 mM EDTA, 4% SDS, protease inhibitors as above) for 10 minutes at room temperature. Next, 3 volumes of Urea buffer (10 mM Tris pH 7.4, 1 mM EDTA, 8M Urea) were added and samples centrifuged at 16,000 x g for 30 minutes. The pellet was again resuspended in 1 volume of SDS buffer, then 3 volumes of Urea buffer was added before centrifugation again. The pellet was washed with SDS buffer before resuspension in ice cold storage buffer (10 mM Tris pH 7.4, 1 mM EDTA, 25 mM NaCl, 10% glycerol). Chromatin DNA was sheared by sonication. The solubilized chromatin was mixed with 3x SDS sample buffer (6% SDS, 150 mM Tris pH 6.8, 30% glycerol) and heated at 95°C for 30 minutes to reverse the crosslinks. 10% of the sample was electrophoresed in a NuPAGE Bis-Tris gel (NP0335, Invitrogen). The de-crosslinked

chromatin proteins were in-gel digested with 2µg trypsin overnight (> 16hours). The tryptic peptides were analyzed by liquid chromatography coupled with tandem mass spectrometry (LC-MS/MS). Data was analyzed with MaxQuant 1.5.7.4 (*85*). The abundance of proteins was estimated using the iBAQ algorithm (*86*), and normalized by the copy number of histone H4 (*87*).

ChIP-seq data re-analysis.

We used the publicly available CAPH ChIP-seq dataset obtained in DT40 cells (GSE45552). We processed the raw sequences following the steps of the ChIP-seq pipeline of the ENCODE consortium (*88*), available at https://github.com/ENCODE-DCC/chip-seq-pipeline/ .

Hi-C protocol

Chromosome conformation capture was performed as described previously (*89*). Briefly, 10-20x10^6 cells were cross-linked in 1% formaldehyde for 10 minutes and quenched in 125 mM glycine. Cells were snap-frozen and stored at -80°C before cell lysis.

Cells were lysed for 15 minutes in ice cold lysis buffer (10 mM Tris-HCl pH8.0, 10 mM NaCl, 0.2% Igepal CA-630) in the presence of Halt protease inhibitors (Thermo Fisher, 78429) and cells were disrupted by homogenization with pestle A for 2x 30 strokes. Chromatin was solubilized in 0.1% SDS at 65°C for 10 minutes, quenched by 1% Triton X-100 (Sigma, 93443) and chromatin was digested with 400 units of HindIII (NEB, R0104) overnight at 37°C.

Fill-in of digested overhangs by DNA polymerase I, large Klenow fragment (NEB, M0210) in the presence of 250 nM biotin-14-dCTP (Life Technologies, 19518-018) for a minimum of 90 minutes was performed prior to 1% SDS based enzyme inactivation and dilute ligation with T4 DNA ligase (Life Technologies, 15224) for 4 hours at 16°C. Cross-links of ligated chromatin were reversed overnight by proteinase K (Life Technologies, 25530-031) incubation at 65°C. DNA was isolated with 1:1 phenol:chloroform, followed by 30 minutes of RNase A incubation.

Biotin was removed from unligated ends by incubation with 15 units of T4 DNA polymerase in the presence of 25 nM dATP/dGTP. DNA was sheared using an E220 evolution sonicator (Covaris) and size selected with Agencourt AMPure® XP (Beckman Coulter) to 150-350 bps. After end repair in a mixture of T4 polynucleotide kinase (25 units; NEB, M0201), T4 DNA polymerase (7.5 units; NEB, M0203L) and DNA polymerase I, large (Klenow) fragment (2.5 units; NEB, M0210) at 20°C for 30 minutes, dATP was added to blunted ends using 15 units of polymerase I, large fragment (Klenow 3' → 5' exo-) (NEB, M0212L) at 37°C for 30 minutes.

Biotinylated DNA was collected by incubation in the presence of 10 µl of streptavidin coated myOne C1 beads (Life technologies, 650.01) and Illumina paired-end adapters were added by ligation with T4 DNA ligase (Life technologies) for 2 hours at room temperature. A PCR titration (primers PE1.0 and PE2.0) was performed prior to a production PCR to determine the minimal number of PCR cycles needed to generate a Hi-C library. Primers were separated from the library using Ampure size selection prior to 50 bp paired-end sequencing on an Illumina HiSeq sequencer (Life Technologies).

Hi-C data analysis

Briefly, we processed Hi-C data as described in (*36*), with multiple modifications, including using the galGal5 genome assembly. All scripts mentioned below to be from the Dekker Lab c-world pipeline are available at a GitHub repository (*90*). cMapping at

https://github.com/dekkerlab/cMapping; iterative correction (balancing) at https://github.com/dekkerlab/balance and analysis scripts at https://github.com/dekkerlab/cworld-dekker. The Mirny Lab software, including the *cooler* library for storage and analysis of Hi-C data is available at https://github.com/mirnylab.

Mapping sequenced Hi-C reads

Fastq files were mapped and binned using the c-world mapping pipeline. Briefly, 50 bp paired end reads obtained as fastq files were truncated to 25 bp starting at the 5' end. Then, they were iteratively mapped (*91*) to the Red Jungle Fowl laboratory line chicken genome (UCSC Genome Browser assembly ID: galGal5, Dec. 2015, Accession ID: GCF_000002315.4; NCBI genome/111 (Gallus gallus)(*92*). Uniquely mapped, paired reads were kept and assigned to a HindIII restriction fragment assigned through its 5' position. Mapped reads were filtered for same fragment ends and uniqueness, excluding PCR duplicates (defined as sequence matches with the exact same start and end).

Hi-C based karyotyping

Genome wide interaction matrices from Hi-C were binned at 1 Megabase resolution. For each bin, we summed up the interactions of this bin with all other bins. Chromosome normalization was obtained by dividing these sums with the total number of interactions per chromosome, corrected for the chromosome size (in Megabases). Genome wide normalization was obtained by dividing each bin sum by the genome wide number of counts (matrix total). The difference between sums normalized by chromosome and matrix indicates copy number alterations and was displayed for each chromosome on a log2 scale.

Contact probability (P(s)) curves

We used the mapped reads to calculate the functions of contact frequency P(s) vs genomic separation s. We split all genomic distances between 1 kb and 1Gb into bins of exponentially increasing widths, such that the upper edge of every bin was 1.12 larger than the lower edge. For every such separation bin, we found the number of observed cis-interactions within this range of separations and divided it by the number of all loci pairs, separated by such distances in cis.

Binning and balancing of Hi-C data

Unique valid pair reads were binned to 10kb, 50 and 100 kb bins, using cooler package, and noisy or low signal bins were excluded prior to balancing using the MADmax filter: we removed all bins, whose coverage was 7 genome-wide median deviations below the median bin coverage. Matrices were balanced by iterative correction (IC), equalizing the sum of every row/column to 1.0 (*33*), using cooler (https://github.com/mirnylab/cooler).

Compartment analysis

Compartments were quantified using principal component analysis on 100 kb binned data using the matrix2compartment perl script in our c-world pipeline. The largest eigenvector (eig1) typically represents the compartment profile(*3, 32, 93*). When compartment signals were low or absent, we checked consecutive eigenvectors to confirm loss of compartments. Per convention A/B-compartments were assigned by gene density, so that the A-compartment was more gene-dense than the B-compartment.

In order to measure the strength of compartmentalization, we used the observed/expected Hi-C maps, which we calculated from 100 kb iteratively corrected interaction maps of cis-interactions by dividing each diagonal of a matrix by its chromosome-wide average value. In each observed/expected map, we rearranged the rows and the columns in the order of increasing eigenvector value. Finally, we aggregated the rows and the columns of the resulting matrix into 30 equally sized aggregated bins, thus obtaining a compartmentalization plot ("saddle plot").

Insulation analysis (TADs)

TAD calling was performed on 50 kb binned data exactly as described previously (*32*). We first determined the optimal insulation square for TAD calling with our c-world pipeline perl script matrix2insulationRange. We used a range of insulation squares from 50 kbp (istart variable) to 1 Mb (iend variable) with a 50 kb (bin size) step (istep variable) to sweep through the insulation topology. From this sweep, we determined to use a 250x250 kb sliding square (is = 250000) along the matrix diagonal without smoothing (ss = 50000) for capturing the aggregate TAD signal for galGal5 (**Fig. S5**). For 40 kb binned HelaS3 (ATCC CCL2.2) Hi-C data, we detected TADs using a 520x520 kb sliding square (is = 520000) without smoothing (ss = 40000). These settings were used as input variables for insulation square analysis with the matrix2insulation perl script from our c-world pipeline. Briefly, the inter quartile (IQR) mean signal within the square (im = iqrMean) was assigned to the diagonal bin and this process was repeated for all bins. The insulation score was then normalized relative to average score of the insulation scores across each chromosome by calculating the log2 ratio of each bin's insulation score and the mean of all insulation scores, as described previously (*32*). Minima along the normalized insulation score vector represent loci of high local insulation and are interpreted as TAD boundaries. For aggregate insulation score pileups, bed files with TAD boundary positions from G2 arrested cells were used as input for each mutant cell line separately (ebf variable). TAD boundary pileups were generated for 50 kb steps (mindist = 50000) covering 500 kb upstream and 500 kb downstream from TAD boundaries (ezs = 500000) with a maximum interaction distance of 500 kb (maxdist = 500000) using our elementPileUp c-world perl script.

Coarse-grained model of contact probability decay in mitotic chromosomes

In the coarse-grained model loops are regularly placed along the axis of the chromosome (z-axis) with a spacing Δ_z. Each loop is represented by a cylindrical wedge, where loci that belong to this loop are distributed normally along the z directions, with mean at the base of the loop and the standard deviation σ), and normally in the angular position with the mean at the orientation of the loop and the standard deviation φ. Orientation of each loop depends on the model and can be uniformly random (*Randomly oriented uncorrelated loops*), correlated with its neighboring loops, forming an angular random walk (*Loops with correlated orientation*), or form a random walk while having a preferred orientation (*Loops with spiral staircase orientation*).

Below, we derive an approximate expression for the probability of a contact between two loci $P_c(s)$, separated by genomic distance s, in a chromosome compacted into an array of consecutive loops. Naturally, this expression has two regimes: (a) the intra-loop regime at shorter genomic separations, where the two loci are located on the same loop, and (b) the between-loop regime at larger separations, when loci are located on different loops. If the lengths of loops are random and distributed exponentially, the transition between the regimes occurs around the genomic separation comparable to the average loop length l_{avg}:

$$P_c(s) = e^{-s/l_{avg}} P_c^{in}(s) + \left(1 - e^{-s/l_{avg}}\right) P_c^{between}(s) \qquad (1)$$

Contacts within loops

The simplest model of individual loop conformations is a random walk in 3D. In this case, the contact probability decays as a power-law with a -3/2 exponent, assuming poor solvent conditions in the melt of loops, and neglecting correction for the closed loop:

$$P_c^{in}(s) = C_{in}\, s^{-1.5} \qquad (2)$$

This scaling is consistent with $P_c(s)$ observed even at larger distances during interphase in very large oocyte nuclei (*94*). Below, we will not attempt to improve this simple model, and instead focus on long-distance behavior of $P_c(s)$, which reflects the mutual arrangement of loops.

Contacts between loops

By definition, a contact between two loci occurs when they have similar coordinates, either in Cartesian or cylindrical coordinates:

$$P_c^{between}(s) = C_{between} P\left(x_i = x_j, y_i = y_j, z_i = z_j\right) = C_{between} P\left(r_i = r_j, \theta_i = \theta_j, z_i = z_j\right)$$

For two loci located on different loops, we can simplify this expression drastically by assuming that the probabilities of overlap at each coordinate are independent of each other:

$$P_c^{between}(s) = C_{between} P(r_i = r_j) P(\theta_i = \theta_j)\, P(z_i = z_j) \qquad (3)$$

Randomly oriented uncorrelated loops

In order to estimate the probability of contact between loci on different loops, we have to make extra assumptions on the mutual orientations of these loops. In the simplest case, each loop is randomly oriented and the orientations of consecutive loops are not correlated with each other. In this case, both $P_c(r_i = r_j)$ and $P_c(\theta_i = \theta_j)$ are independent of the separation between the loops and thus integrate to a constant, leaving:

$$P_c^{uncorr}(s) = C_{between} P(z_i = z_j) = C_{between} P_c^z(s)$$

We can calculate this remaining expression easily if we assume that the loci within each loop are normally distributed along the z-axis, each around the base of its loop:

$$P_c^z(s) = C \int_{-\infty}^{\infty} \int_{-\infty}^{\infty} N(z_i, \bar{z_i}, \sigma) N(z_j, \bar{z_j}, \sigma)\, \delta(z_i - z_j) dz_i dz_j$$

In this expression, N(x, mean, s.d.) is the PDF of the normal distribution, i and j are the genomic coordinates of the two loci, z_i and z_j are the axial coordinates in the 3D genomic structure, $\bar{z_i}$ and $\bar{z_j}$ are the expected axial coordinates of the i-th and j-th loci (which, by our assumption, are equal to the axial coordinates of their corresponding loop bases), σ is the measure of the spread of loop along the axis of the chromosome, i.e. the high of each loop, and $\delta(z_i - z_j)$ is the delta function that limits the integral only to the conformations where the particles have the same axial coordinate. Taking this integral gives us:

$$P_c^z(s) = C\, N(\bar{z_i} - \bar{z_j}, 0, \sqrt{2}\sigma)$$

Finally, if the loops are regularly places along the axis of the chromosome with a spacing Δ_z, than the expected axial distance between the bases of two loops is equal the expected number of loops between these two loci, multiplied by Δ_z:

$$P_c^z(s, l_{avg}, \Delta_z, \sigma)(s|\, l_{avg}, \Delta_z, \sigma) = C\, N\left(\Delta_z \frac{s}{l_{avg}}, 0, \sqrt{2}\sigma\right) = C'\, N\left(\frac{s}{l_{avg}}, 0, \frac{\sqrt{2}\sigma}{\Delta_z}\right) \qquad (4)$$

$P_c^Z(s)$ describes the decay of contact probability due to the decreasing axial overlap of more distant loops and, as illustrated in **Fig. 2B**, produces a characteristic drop-off in log-log representation of $P_c(s)$. The drop takes place at when the number of loop s/l_{avr} exceeds ~$2\sqrt{2}\sigma$ /Δ_z the ratio of the loop high and the separation between loop.

For example, at prophase a drop at 4.5Mb for loops of the average size l_{avr} = 80Kb requires 56 loops per layer. Hence $2\sqrt{2}\sigma$ /Δ_z = 56; then for σ= 200nm of loop high, one gets Δ_z=7.5nm separation between neighboring loops. This is a tight packing at the scaffold, but feasible with

10nm fiber emanating from condensins, possibly requiring the scaffold to wiggle inside the chromosome. For prometaphase, a drop at 10Mb and 80Kb loops leads to 125 loops per layer, and the spacing of 3nm, which is smaller than protein domains of condensin, necessitating nested loops and considerable winding of the scaffold inside the chromosome.

Loops with correlated orientation

$P_c^z(s)$ alone does not fully explain the experimentally observed $P_c(s)$ curves: it explains the origin of a drop in contact probability at longer distances, but does not explain the origin of a gradual decay before the drop. Equation (3) then suggests that this extra gradual decay might be due to the angular overlap $P(\theta_i = \theta_j)$. Specifically, if the angular orientations of consecutive loops are somehow correlated, forming the angular (1D) random walk, this would increase the frequency of angular overlaps for loci in adjacent loops and make it smaller for loci that are contained in distant loops.

$$P_c^{corr}(s) = C_{between} P(z_i = z_j) P(\theta_i = \theta_j) = C_{between} P_c^z(s) P_c^{ang,corr}(s) \quad (5)$$

We can derive the frequency of angular overlaps explicitly:

$$P_c^{ang,corr}(s) = \int_{-\infty}^{\infty}\int_{-\infty}^{\infty}\int_{-\infty}^{\infty} N(\theta_i, 0, \phi) N(\theta_j, \bar{\theta}_j, \phi) N\left(\bar{\theta}_j, 0, \gamma\sqrt{s/l_{avg}}\right) \sum_{k=-\infty}^{\infty} \delta(\theta_i - \theta_j + 2\pi k)\, d\theta_i d\theta_j d\bar{\theta}_j$$

Here, θ_i and θ_j are the angular coordinates of the two loci, which are distributed normally around the mean angular orientation of their loops (0 and $\bar{\theta}_j$, correspondingly) with the standard deviation φ. The correlations in the orientations of adjacent loops lead to the fact that the mean angular orientation of the loop with the j-th locus, $\bar{\theta}_j$, is normally distributed itself around the mean of 0 (which we picked to be the angular orientation of the loop with the i-th locus, without a loss of generality) and the standard deviation of $\gamma\sqrt{s/l_{avg}}$. The latter is calculated from the assumption the angles of two consecutive loops on average differ by γ; thus, between the i-th and j-th locus there are s/l_{avg} loops, each taking a random step of γ, thus producing a 1D random walk with the standard deviation of $\gamma\sqrt{s/l_{avg}}$. Taking all integrals gives us:

$$P_c^{ang,corr}(s) = \int_{-\infty}^{\infty} \sum_{k=-\infty}^{\infty} N(\bar{\theta}_j + 2\pi k, 0, \sqrt{2}\phi)\, N\left(\bar{\theta}_j, 0, \gamma\sqrt{s/l_{avg}}\right) d\bar{\theta}_j$$

$$P_c^{ang,corr}(s, l_{avg}, \phi, \gamma)(s|\, l_{avg}, \phi, \gamma) = C\left(\gamma^2 \frac{s}{l_{avg}} + 2\phi^2\right)^{-0.5} \quad (6)$$

$P_c^{ang,corr}$ describes the decay of contact probability with distance due to gradually decaying correlations of more distant loops. For a range of parameters, it can produce a characteristic -0.5 power-law decay of $P_c(s)$, before the random walk fills the whole 2π In combination with the drop-off decay due to decreasing axial co-localization, P_c^z, these two terms produce a prophase-like three-regime decay of contact probability, as illustrated in **Fig. 2B**.

Interestingly, when the angular random walk fills a full circle the angular part of the contact probability becomes constant and independent of *s*, i.e. $P_c^{ang\ corr}(s) \sim s^{-0.5}$, while the angular displacement $\gamma\sqrt{s/l_{avg}} < 2\pi$. For more loops per layer $P_c(s)$=const is expected to appear. Since we don't see this regime in the data, it means that $\sqrt{s/l_{avg}} < 2\pi$ for s within a layer. Hence for a drop at 10Mb and 80Kb loops, we get 125 loops per layer and $\gamma < 2\pi/11$, so the angle between loops should be below or around 30 degrees.

Loops with spiral staircase orientation

Finally, we build a model that could explain the non-monotonic dependency of contact probability with separation, observed in Hi-C of prometaphase chromosomes. This non-monotonicity could be explained by spiralization of chromosomes, previously observed with an electron microscope. In our model, we can describe this spiralization as periodicity of the angular orientations of loops. In order to agree with the experimental data, we have, however, to combine this periodicity at larger scales with random correlated angular loop orientations at shorter separations.

These properties could all be achieved when the angular orientations of loops follow a 1D random walk under the constraint that each loop cannot deviate too much from its preferred orientation, set by the spiral, i.e., linearly proportional to its index. The probability of an angular overlap between loci on two loops can be calculated as the probability of a return of such 1D random walk to its initial position after s/l_avg steps. These random walks are known under the name of the Ornstein-Uhlenbeck (OU) processes, and their properties, including the return probability, have been studied in the theory of stochastic processes (*95*):

$$P_c^{OU}(s) = C_{between} P(z_i = z_j) P(\theta_i = \theta_j) = C_{between} P_c^z(s) P_c^{ang,OU}(s)$$

$$P_c^{ang,OU}(s) = \sum_{k=-\infty}^{\infty} N\left(2\pi k, \Delta_\theta s/l_{avg}, \sqrt{2\phi^2 + \gamma^2 n_{return}(1 - e^{s/l_{avg}/n_{return}})}\right)$$

Here, Δ_θ is the systematic shift of the angle per loop (which produces the spiral phenotype). n_{return} is the parameter of the Ornstein-Uhlenbeck process characterizing the variability of the angular loop orientations around their optimal orientation: the loops deviate on average by $\sqrt{n_{return}}\gamma$ from their optimal angular orientation and the n_{return} consecutive loops have correlated orientations. We also modified the standard formula for the return probability of the trending OU process to account for the fact that, in angular coordinates, two points overlap when they have the same angle modulo 2*pi.

Bridging the in-loop and between-loop regimes

Note that both expressions of P_c^{in} and $P_c^{between}$ contain arbitrarily defined coefficients C_{in} and $C_{between}$. In order to obtain a unified expression that describes the contact probability at all length scales, we need adjust these coefficients, such that $P_c^{in}(s)$ and $P_c^{between}$ could be directly compared to each other. Both of these coefficients are arbitrary and their ratio only affects the narrow transitional region at s ~ 1-3 l_{avg}. In the calculations presented in the paper, we calculate these coefficients by matching the two curves at the separation of two average loop sizes:

$$P_c^{in}\left(\frac{2s}{l_{avg}}\right) = P_c^{between}\left(\frac{2s}{l_{avg}}\right)$$

Polymer models of mitotic chromosomes

The design of Langevin molecular dynamics simulations of chromosomes

In order to test the proposed architectures of prophase and prometaphase chromosomes against our Hi-C data, we simulate polymer models of chromosomes using Langevin molecular dynamics. The overall design of these simulations is similar to that in (*8*, *24*), with a few major differences. We model 10nm 'beads-on-string' chromatin fiber of nucleosomes as a chain of 10nm particles, each representing one nucleosome with 200bp of DNA. These particles are connected by springs with a using a harmonic potential with an equilibrium length of 10nm and the stiffness coefficient of 1 kbT/nm^2. We simulated repulsion between spatially overlapping nucleosomes using the following force potential:

$$U = 5\left(-1 + \left(\frac{0.105 \cdot r}{\sqrt{6/7}}\right)^{12} \cdot \left(\left(\frac{0.105 \cdot r}{\sqrt{6/7}}\right)^{2} - 1\right) \cdot \frac{823543}{46656}\right) k_b T$$

This potential is designed to be constant of 5.0 kbT until r = 7-8nm, and then rapidly go to zero around 10.5 nm. The limited maximum overlap energy of 5.0 kbT allowed chromatin fibers to pass through each other occasionally and thus accounted for the strand-passing activity topoisomerase II. In all of our simulations, we additionally compact chromosomes using cylindrical constraints to impose the high chromatin density of one nucleosome per 11nm x 11nm x 11nm box, as observed in EM images of mitotic chromosomes. The particular geometric parameters of the cylindrical constraint varied between simulations. We imposed this constraint using a harmonically increasing potential with k=0.1 kbT when monomer crossed the boundaries of the constraining cylinder. We perform Langevin dynamics polymer simulations using OpenMM, a high-performance GPU assisted molecular dynamics API (*96*, *97*). We used the following parameters of the Langevin dynamics – variable time step to achieve the relative accuracy of 0.001, the friction coefficient of 0.01, particle mass of 1.0 and the temperature of 300K. We ran the simulations until the simulated *P(s)* curves (see below) stopped changing at logarithmic time scales, which occurred after 1.5e7 timesteps in prophase simulations and after 3e6 timesteps in prometaphase simulations. We visualized the resulting chromosome structures using Pymol (DeLano, Warren Lyford. "PyMOL." (2002)).

Simulations of prophase and CAP-H2-depleted chromosomes

We simulated prophase chromosomes as arrays of consecutive loops compacted into a cylindrical shape with a high chromatin density. As in (*8*), we first randomly selected a subset of particles to be bases of consecutive loops, such that the loop lengths were exponentially distributed with an average of l_{avg}. We modelled loop-forming condensins by imposing extra harmonic bonds between the particles representing loop bases. Finally, we tethered the first and the last particles of the chromosome to the ends of the compacting cylinder using a harmonic attraction potential along z-coordinate with k=0.15 kbT/nm^2. We equilibrated the each simulation for 1.5e7 steps to allow for slow large-scale rearrangement of the flexible chromosome scaffold. To match the simulations with the WT prophase and CAP-H2 prometaphase experiments, we systematically varied the two model parameters: (1) the average loop length, l_{avg}, from 20 kb and 100 kb, with a step of 10 kb and (2) the average linear density of loops along the axis of the constraining cylinder, N_{loops}/L, from 50 loops/μm to 350 loops/μm, with a step of 50 loops/μm. For each parameter set, we modeled a chromosome containing 500 average loop lengths.

Simulations of prometaphase and CAP-H-depleted chromosomes

We simulated prometaphase chromosomes as helical arrays of consecutive nested loops compacted into a cylindrical shape with a high chromatin density. As in the prophase simulations above, we first imposed an array of consecutive loops with the average loop length of lavgouter. To account for the action of condensin I, we further split each of these “outer” loops into an array of smaller exponentially distributed “inner” loops, with an average length lavginner. To test if the Hi-C data is consistent with helical winding of prometaphase chromosomes, we fixed the bases of the “outer” loops along a 3-dimensional helical path winding around the axis of the constraining cylinder. We imposed this helical path by tethering each loop base to its specific position along the helix with a harmonic potential with k=0.04 kbT/nm2. We equilibrated each simulation only for 1e6 steps, since the motion of the backbone was suppressed and only individual loops had to equilibrate. To match the simulations with the prometaphase experiments, we varied four parameters of the model: (1) the average inner loop size, lavginner, from 20 kb to 100 kb every 20 kb; (2) the average outer loop size lavgouter as a multiple of the average inner loop size lavginner, from 1 to 11 inner loops, with a step of 2; (3) the average amount of DNA per helical turn, P, from 2 to 15 Mb, with a step of 1 Mb; (4) the pitch of the helical scaffold, b, from 50 to 300nm, with a step of 50nm. As above, for each parameter set, we modeled a chromosome containing 500 lavgouter. For each parameter set, the length of the constraining cylinder matched the axial length of the helical scaffold, and the radius of the cylinder was adjusted to reach the density of 1 particle per 11nm x 11 nm x 11 nm box.

Simulated Hi-C and P(s) calculation for polymer models

We then used our polymer models to perform in-silico Hi-C. For each polymer model, we picked the chromosome structure at the end of the simulation and found all pairs of contacting monomers, i.e. pairs of monomers separated by less than 51nm in 3D space. As in the experimental Hi-C, we used these pairs to calculate the contact frequency vs separation *P(s)* curves.

Model selection via comparison of simulated and experimental P(s) curves

To find which simulations produce the best agreement with the experimental data, we systematically tried all possible combination of the model parameters. For each parameter set, we performed a simulation, generated a *P(s)* curve and calculated the root mean square (r.m.s.) difference with the experimental *P(s)* in the log10-log10 scale, after normalizing both of the curves at the specific distance (see the table below). Our simulations cannot predict *P(s)* both at very short separations, below a loop size, and at very long separations, after the drop-off; for that reason, we limit our *P(s)* discrepancy computations to ranges shown in the table below. Finally, we equalize the contribution of the short- and long-distance parts of the *P(s)* (**Table S4**) by calculating the r.m.s. *P(s)* difference in each of these regions separately and reporting the mean of the two.

P(s) estimation for prophase models with sister chromatid cohesion

In order to understand how the presence of a spatially proximal sister chromatid could change the *P(s)* curves we performed a mock-up simulation. We considered the 3D structure of the best-fitting prophase model and added to it its identical copy shifted along the direction perpendicular to the chromatid axis by distance Δ_x^{sister}. We then calculated the *P(s)* for this structure, under the assumption that our *in-silico* Hi-C procedure could not tell apart the corresponding identical loci on the two chromatids. We then repeated this procedure for different values of Δ_x^{sister}, from 0 (a complete overlap between the two chromatids) to 2 chromatid radii (a complete segregation of the chromatids).

Estimation of the rate of loop formation at condensin binding sites.

We calculated the average contact frequency around condensin binding sites at 10kb resolution, considering interactions formed by loci located up to 1Mb away from the condensin sites. We then normalized these average maps by the distance-dependent decay of contact frequency *P(s)*, thus obtaining average "observed-over-expected" maps of contact enrichments around condensin binding sites.

We used the simulated 3D models of prometaphase chromosomes at 60 minutes to calculate the average contact map around a loop anchor. We simulated a Hi-C map for the whole model at 10kb resolution and averaged its segments around 1000 randomly chosen loop anchors. As with the experimental maps, we then normalized it by the decay of contact frequency with distance from the same model.

The average map of contacts formed by loop anchors in our 60 minute model showed a "plus-sing" pattern, corresponding to the enrichment of contacts between loop anchors and their neighboring loci. In our experimental Hi-C data, the condensin binding sites displayed a similar contact pattern, albeit noticeably weaker, suggesting that condensin binding sites harbor a loop anchor only in a fraction of sampled cells.

We then quantified the strength of these "plus-sign" patterns in our experimental and simulated maps as the median observed-over-expected enrichment of contacts formed between the sites in question (condensin binding sites, for experimental data, and a loop anchor, for simulated data) and their neighboring loci, divided by the median observed-over-expected of contacts between all pairs of neighboring loci. Comparing the strengths of "plus-signs" at condensin sites to the strength of such patterns at loop anchors in our simulations allowed us to estimate how often condensin sites harbor a loop in the sampled population of cells.

Simulations of nested loop formation by loop extrusion.

To test if the process of loop extrusion can form nested loops, we performed lattice loop extrusion simulations as previously described in (*25*). Briefly, such simulations aim to model the positions and sizes of loops produced through the process of loop extrusion and do not explicitly consider the 3D chromosome conformation. In these simulations, a chromosome is divided into a 1D lattice of sites and the condensin-extruded loops are represented by a pair of sites, loop anchors, which are brought together at the base of a loop. We simulate loop extrusion by step-wise shifting of the two loop anchors of each condensin away from each other over time. To simulate the chromatin binding/unbinding dynamics of condensins, we occasionally remove them from the lattice and put back to a randomly chosen location, where they start a new loop. The code for these simulations is available at https://github.com/golobor/looplib/.

To simulate extrusion of loops by condensins I and II, we considered 20Mb of chromatin fiber, divided into a lattice of 100,000 sites of 200bp each. We initialized the system by randomly placing condensins I (one per 40kb) and II (one per 160kb) along the lattice, such that the two loop anchors of each condensin were located on the adjacent lattice sites (i.e. they have not yet extruded any loop). We then simulated the process of loop extrusion at the average speed of 10 sites per second at each loop anchor. The average residence time was 2 minutes for condensins I and 120 minutes for condensins II. We ran simulations for 2 hours of experimental time.

Simulations of suppression of TADs and compartments by loop extrusion in prophase

Polymer simulations of an 8.3 Mb fiber with loop extrusion and compartmentalization are performed as described in *(24, 98)*. We chose parameters to reproduce loop length estimates in interphase / 5min prophase / 7.5min prophase: Loop extrusion factor (LEF) processivity/separation was 250kb/500kb = 1/2 (interphase), 125kb/31.3kb = 4 (5 min prophase), 250kb/25kb = 10 (7.5 min prophase). Other simulation parameters are: coarse graining = 400bp/monomer, LEF speed = 580 bp/s on each LEF side, boundary stopping probability=90%, monomer volume density=0.15 (bead diameter)^3, compartmental interaction parameter=0.12 kT, repulsive core strength=3 kT, mean distance between CTCF sites=430 kb, crosslinking radius for simulated Hi-C = 4 bead diameters. Hi-C maps, insulation tracks, Eigenvectors, and insulation pileups are binned at 50 kb, compartmentalization plots at 100 kb. Example configurations are colored linearly along the fiber from red to blue.

Figures S1-S27

Fig.S1

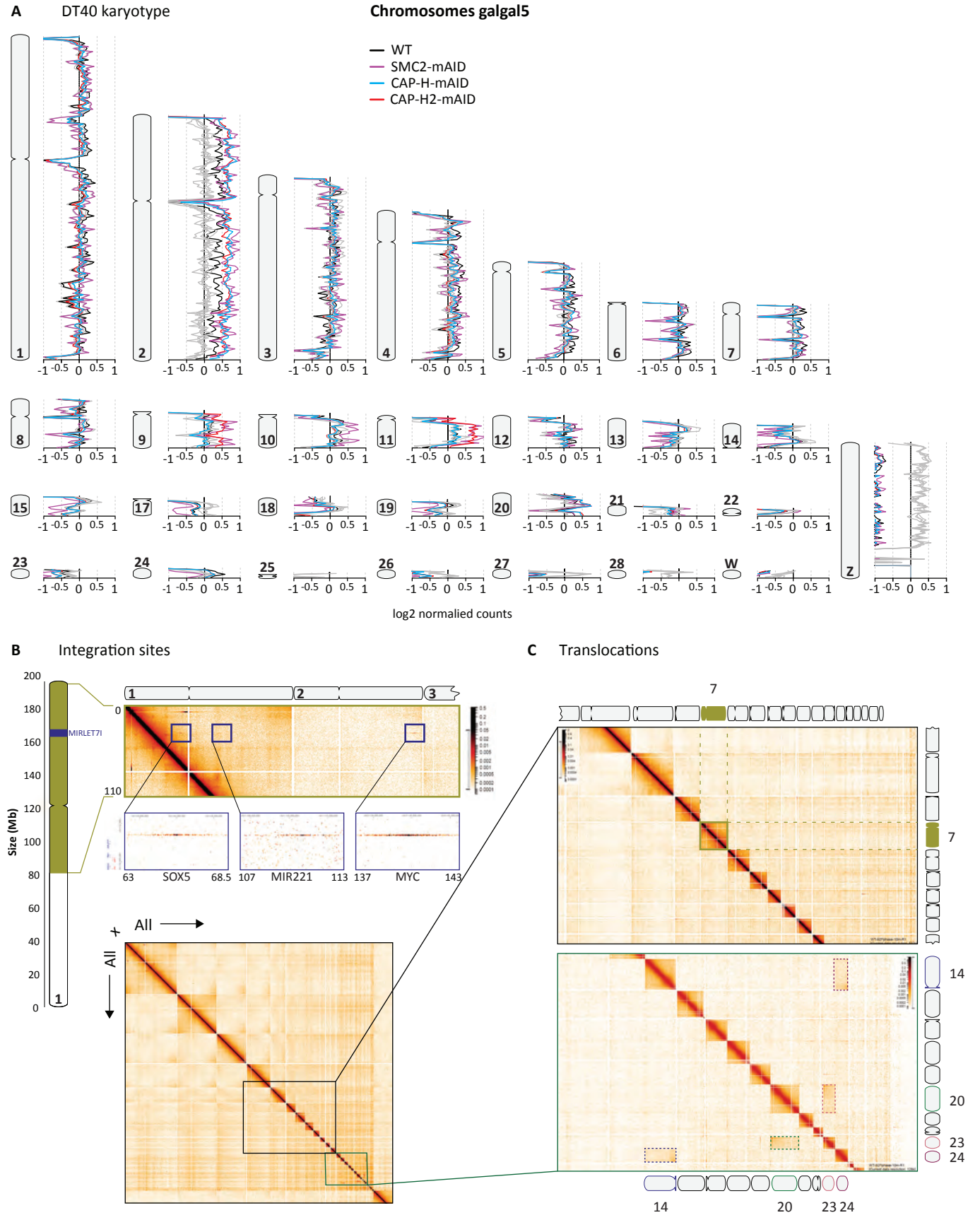
A
DT40 karyotype
Chromosomes galgal5
WT
SMC2-mAID
CAP-H-mAID
CAP-H2-mAID
log2 normalied counts
B
Integration sites
Size (Mb)
MIRLET7I
SOX5
MIR221
MYC
All
C
Translocations

Fig.S1

Hi-C based karyotyping of cell lines. (A) Karyotype plots derived from 1Mb binned Hi-C matrices. The sum of interactions for each bin with every other bin is normalized both genome wide (gray lines) and by chromosome (colored by cell line) and displayed on the x-axis (log2 normalized counts) for each individual chromosome (y-axis) from Hi-C data obtained from cells at t = 10 minutes (wild-type (black), SMC2-mAID (magenta), CAP-H2-mAID (red) and CAP-H-mAID (blue)). A relative increase in chromosome normalized counts in comparison to genome wide normalized counts indicates copy number gains, whereas a decrease shows copy number loss. (B) Integration sites. Translocations are visible from Hi-C maps as an increased normalized read counts at the intersection of the original locus and the site of translocation. The integration of SOX5 near the MYC gene occurred at the generation of the DT40 cells line and has been described previously (*98*). Our Hi-C maps show that MYC, SOX5 and MIR221 have translocated to a single integration site on chromosome 1 (shown in green box), just upstream of MIRLET7I (blue). (C) Translocations. Translocations show as an increase in Hi-C signal between different chromosomes. We observed translocations between chromosomes 14 and 24 as well as 20 and 23 (dotted boxes), but not for the other chromosomes including chromosome 7 (green), which was used as our model chromosome throughout this manuscript.

Fig.S2

FACS analyis after release from synchronization

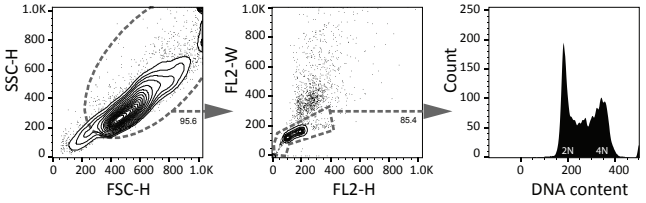

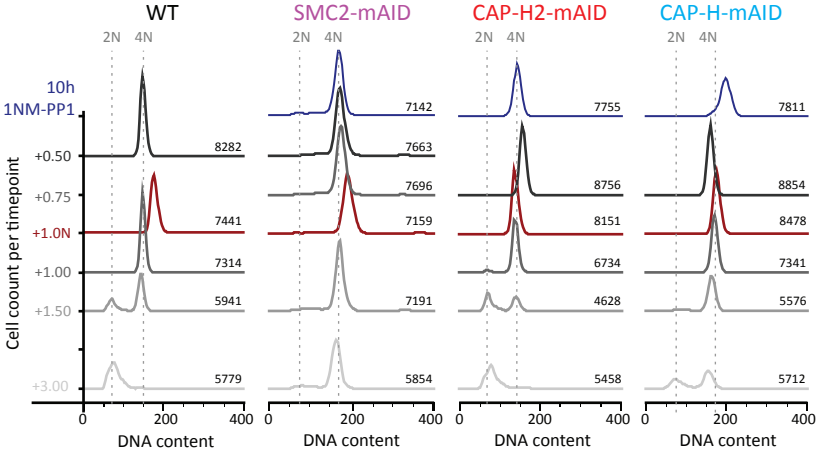

Fig.S2

FACS analysis for synchronized cell cultures. FACS is shown for auxin induced and CDK1as synchronized (10 hr 1NM-PP1) cell cultures. Gating was applied for live cells (top-left) and singlets (top-middle) and gated cells were plotted as a histogram for DNA content (top-right). The bottom plot shows the DNA content (propidium iodide) on the x-axis and time after 1NM-PP1 release (in hours after release from G_2 arrest) on the y-axis (top to bottom) for each auxin induced cell line. Cells were not blocked at prometaphase with nocodazole except for the samples indicated with red lines (1.0N). This analysis allows determination of the timing for exit from mitosis as a loss of cells in G_2/M (4N peak) and a subsequent increase in cells in the G_2 peak (2N).

Fig.S3

NEBD visualized by Lamin staining

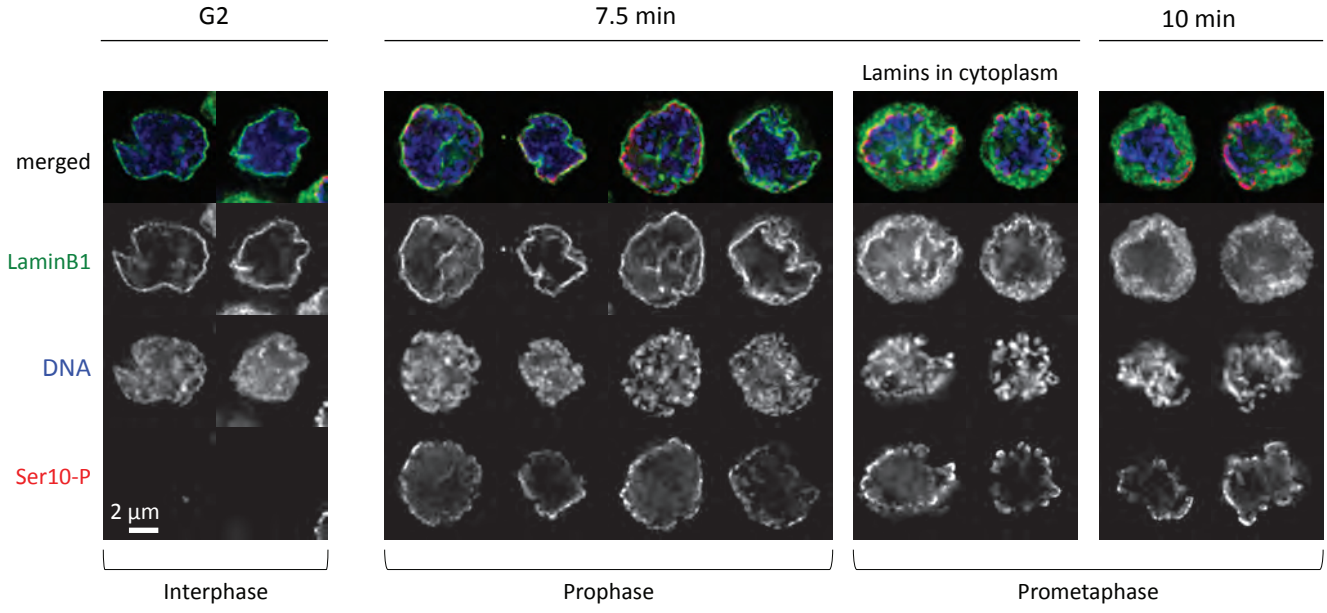

Fig.S3

Nuclear envelope breakdown (NEBD) in CDK1as synchronized DT40 cells determined by Lamin B1 staining. Lamin disassembly and chromosome condensation gradually occur at nuclear breakdown. Lamin B1 localizes at the nuclear periphery (green pseudocolor) before and throughout the cytoplasm after NEBD. Serine 10 of histone H3 becomes phosphorylated during mitosis (H3K10ph, red). DNA stained by DAPI is shown in blue (pseudocolored).

Fig.S4

A Images corresponding to samples for condensin ChEP data

WT

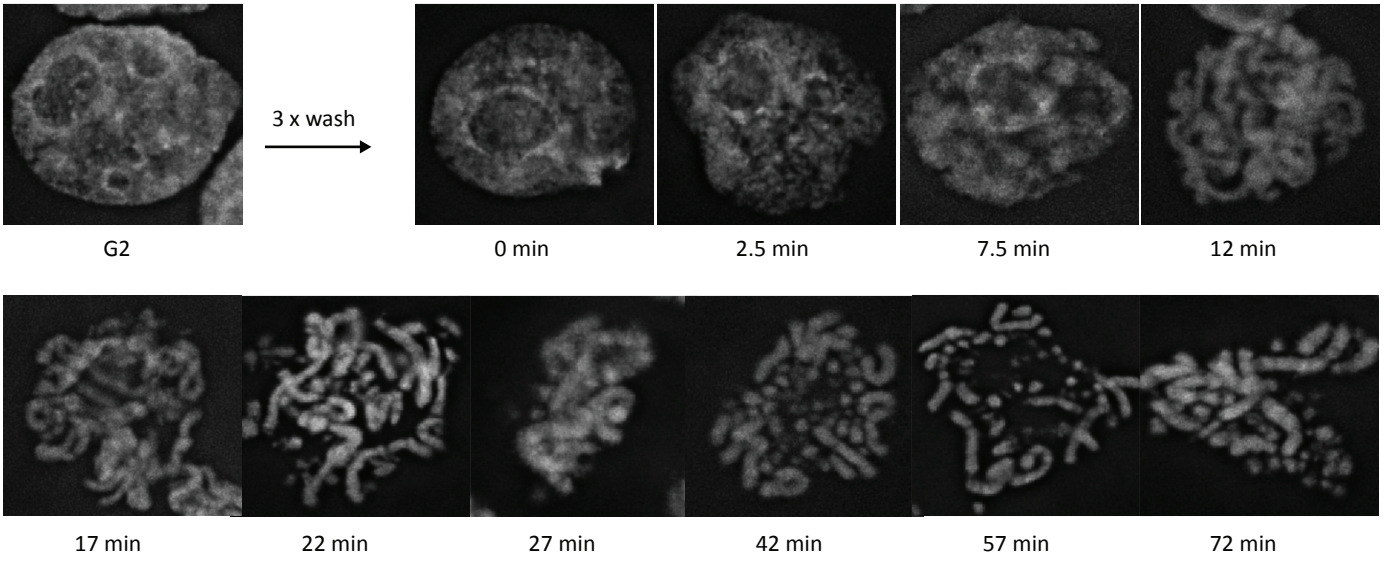

ChEP data

B WT

C CAP-H-mAID

D Cohesin/CTCF

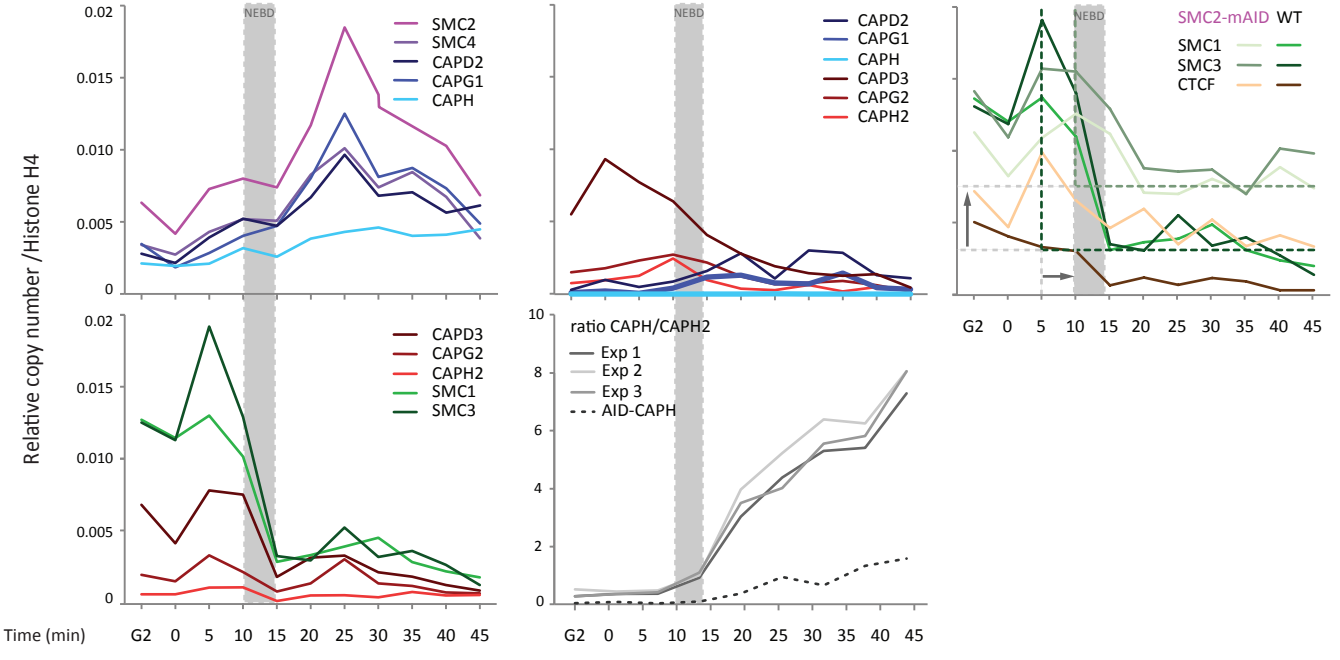

Fig.S4

Chromatin enriched proteomics (ChEP) data for CDK1as synchronized DT40 cells. Chromatin enrichment for proteomics (ChEP) (*58*) identifies proteins associated with the DNA (see Supplementary Methods). **(A)** Microscopy (DAPI staining of chromosomes) of cells at different time points in mitosis. **(B)** The relative quantitation of chromatin bound condensin I, II and cohesin subunits in CDK1as synchronized cells through WT prophase and prometaphase. Numbers on the y-axis are arbitrary MaxQuant units (in millions), normalized for Histone H4 levels. Timing was made comparable to samples used for microscopy and Hi-C libraries based on nuclear and chromosomal morphology in (**A**). **(C)** ChEP from CAP-H depleted (CAP-H-mAID) cells indicates a loss of chromatin bound condensin I subunits after auxin mediated depletion (top). The bottom plot shows the ratio of chromatin binding for CAP-H over CAP-H2 subunits after CAP-H depletion (dotted line) in comparison to 3 replicate control synchronized time course experiments wherein CAP-H was not depleted. **(D)** ChEP for cohesin and CTCF binding to chromatin in SMC2-depleted cells (auxin induced SMC2-mAID) and condensin containing (un-induced) cells. Condensin depletion results in delayed loss of cohesin and CTCF (indicated by the horizontal arrow) and retention of more cohesin and CTCF binding (indicated by the vertical arrow).

Fig.S5

A Insulation analysis at varying length scales

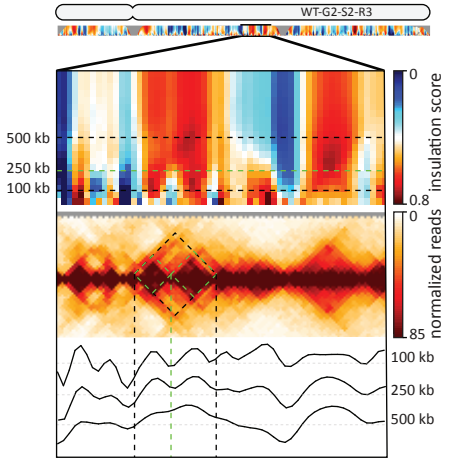

B Insulation score variance

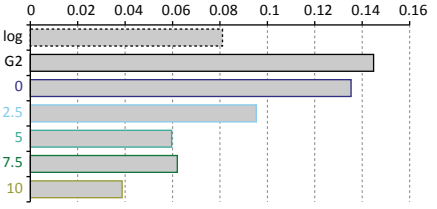

Fig.S5

Insulation parameter settings for TAD analysis. **(A)** Insulation at different length scales. Hi-C matrices were subjected to insulation analysis (depicted in interaction heatmap below). An insulation score is calculated for each bin by summing all interactions occurring between loci located up to a defined distance upstream and downstream of the bin (indicated by the diamond squares in the bottom panel). This method is described in detail in (*32*). Bins with high insulation (at a TAD boundary) have a low insulation score, as measured by fewer interactions occurring across it. Bins with low insulation or boundary activity (the middle of a TAD) have a high insulation score. Minima along the insulation profile are potential TAD boundaries. We determined the optimal square size from a range of 50kb to 1Mb to be 250 kb. The large black dotted square (chromatin domain) contains 2 smaller domains structures, indicated by green squares. The specific insulation analyses using 100, 250 and 500 kb windows below the interaction heatmap reveal that small insulation square sizes (<100kb) pick up small scale fluctuations in insulation, whereas larger squares (>500 kb) miss weaker boundaries (green dotted line derived from square above). The line graph in the bottom shows the fluctuation in insulation score for each tested square size (100, 250, 500kb) for the same chromosomal region as the interaction maps above. **(B)** Insulation score variance calculated with a square size of 250 kb for Hi-C data obtained at different times during prophase. The loss of variance in insulation score as prophase progresses indicates loss of TAD structure (*8*).

Fig.S6

Contact frequency *P(s)* plots for all individual chromosome arms

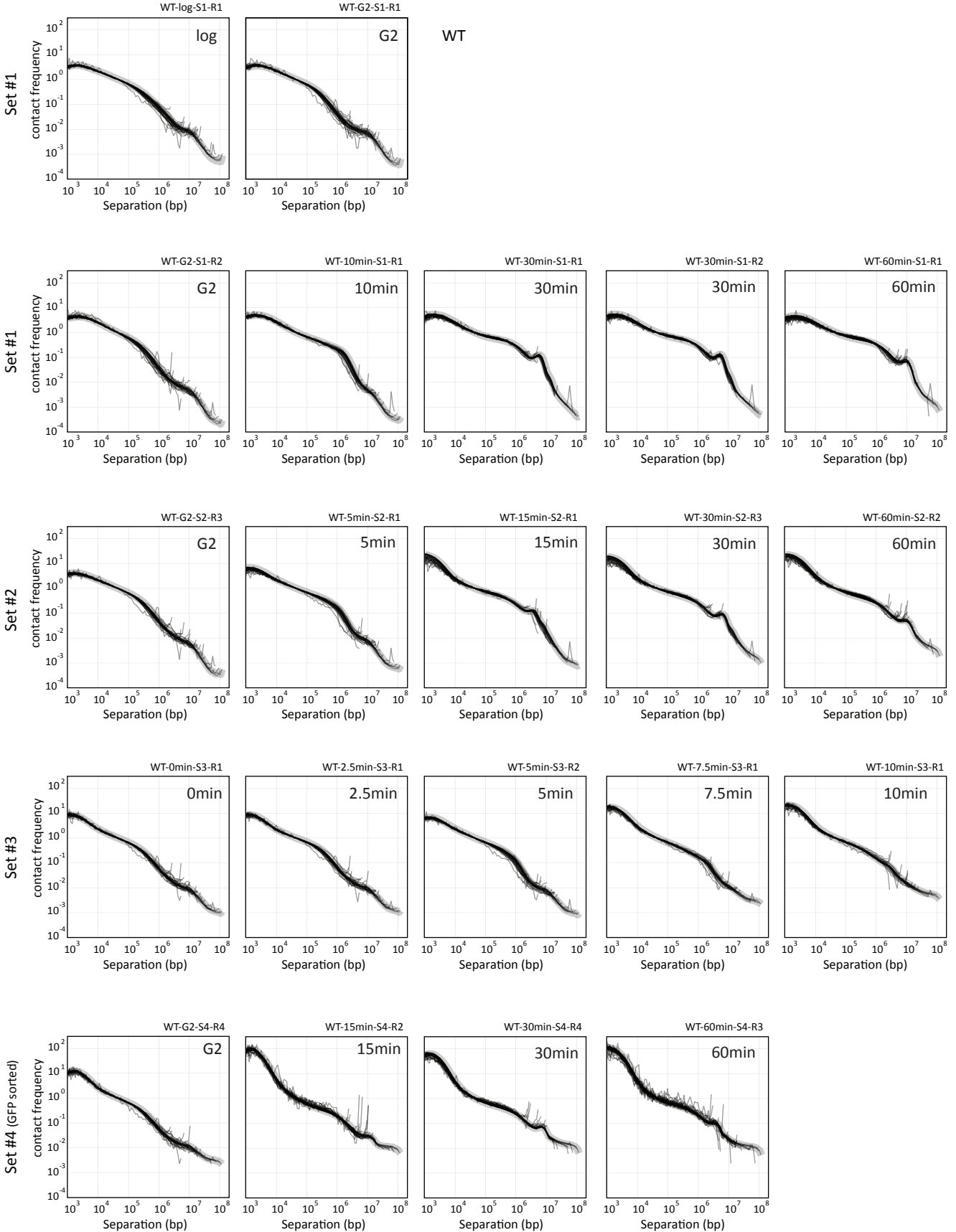

Fig.S6

Contact frequency (*P(s)*) derived from Hi-C data obtained from CDK1as synchronized DT40 cells. Contact frequency *P(s)* plots for all 4 sets of WT Hi-C libraries. Plots for individual chromosome arms are shown in gray; the deviation from the mean decay is shown in light gray. **Table S2** describes each sample in detail.

Fig.S7

A Contact frequency *P(s)* plots for all WT chromosome arms combined

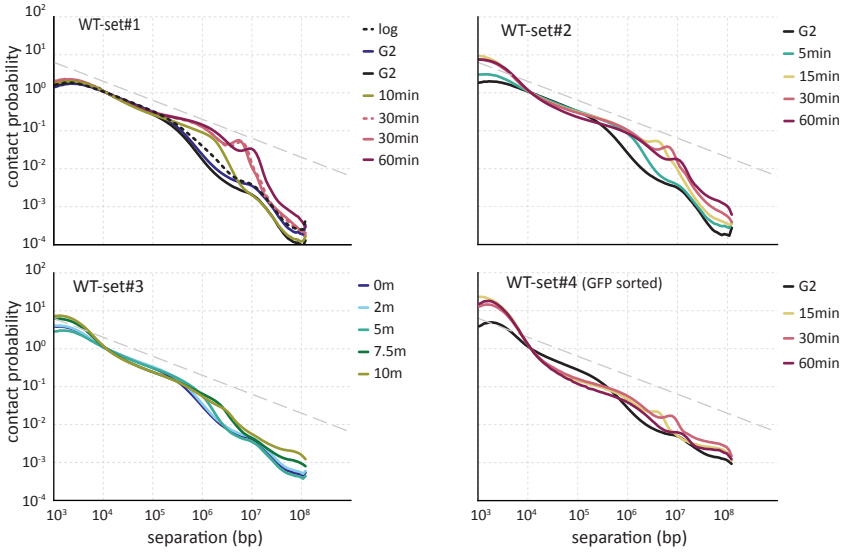

B Scaling derivative plots for all WT chromosome arms combined

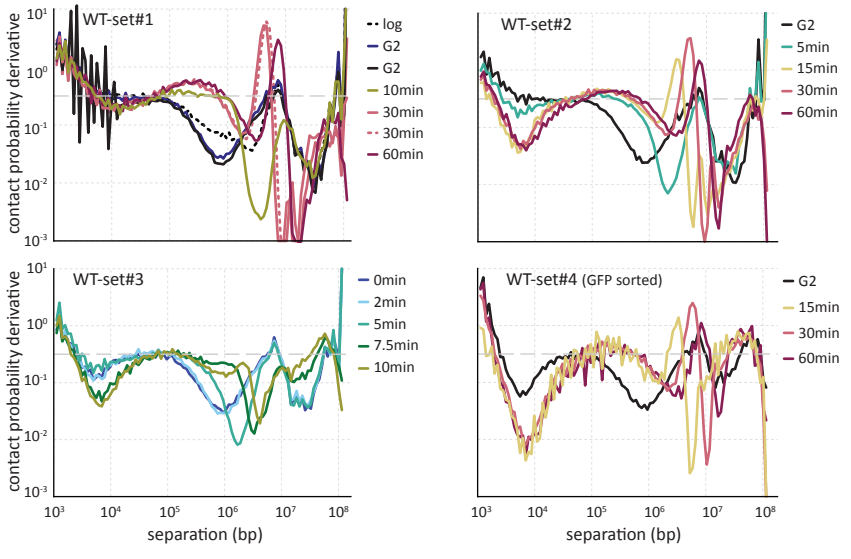

Fig.S7

P(s) plots and their corresponding derivative plots. *P(s)* plots and their corresponding derivative plots for 4 separate timecourse sets are shown for Hi-C datasets obtained from WT CDK1as cells at indicated time points after release from G_2 arrest.

Fig.S8 Chromosome 7 Hi-C interaction maps from all individual libraries for WT

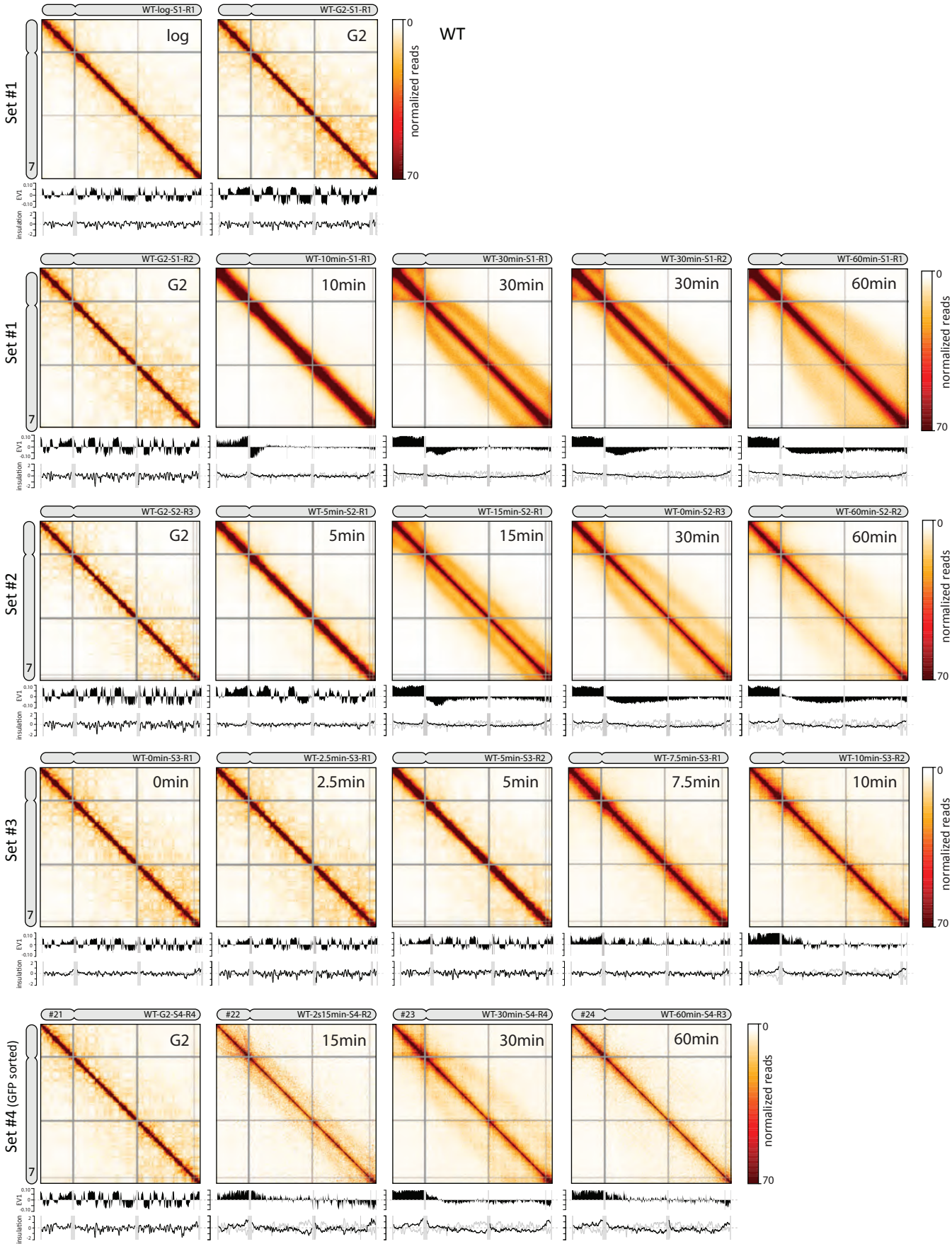

Fig.S8

Hi-C data obtained from CDK1as synchronized DT40 cells at different time points in mitosis. Hi-C interaction maps were generated for chromosome 7 normalized to 1,000,000 interactions. Library names are indicated in the chromosome drawing on top right. **Table S2** describes each sample in detail. The top plot below each Hi-C interaction map displays compartment signal (Eigenvector 1). The bottom graph shows insulation score (TADs). Data for 4 independent sets of Hi-C data obtained from independent time courses are shown.

Fig.S9

Saddle plots for all individual chromosome arms from WT

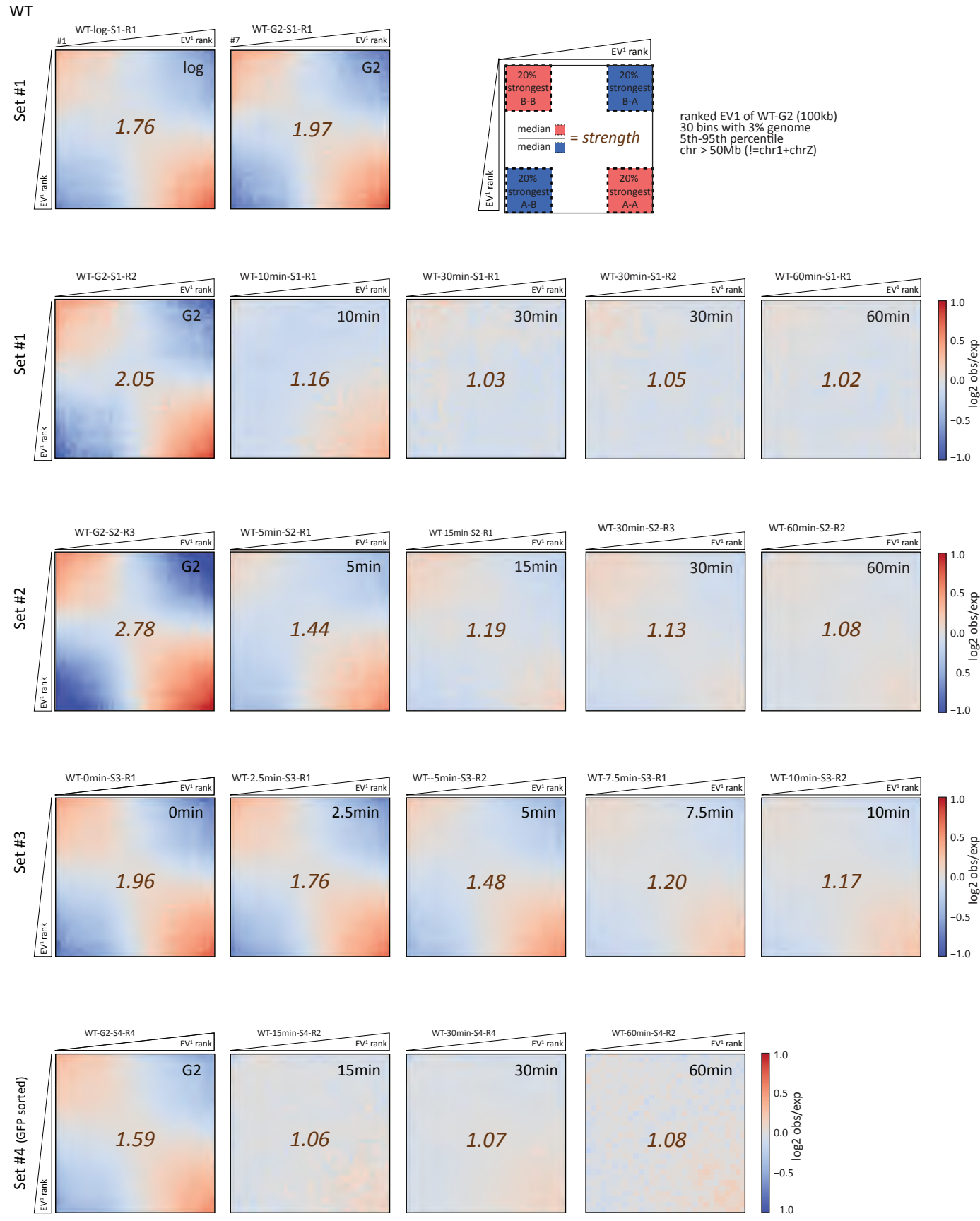

Fig.S9

Quantification of compartment interactions by "saddle plots". The heatmaps show the average distance-normalized cis interaction frequencies between pairs of 100kb bins as a function of their compartment state (defined as the genome-wide rank of their eigenvector 1 value). The upper left corner of the map shows the interactions between pairs of bins, where both belong to the inactive compartment (i.e. compartment B); the lower right corner shows the interactions between pairs of bins from the active compartment (compartment A). The number on each heatmap indicates the overall strength of compartmentalization, defined as the median signal from the top 20% of A-A and B-B interactions, divided by the top 20% of A-B interactions ((AA+BB)/2AB). Library names are located on the top left. **Table S2** describes each sample in detail.

Fig.S10

Normalized insulation

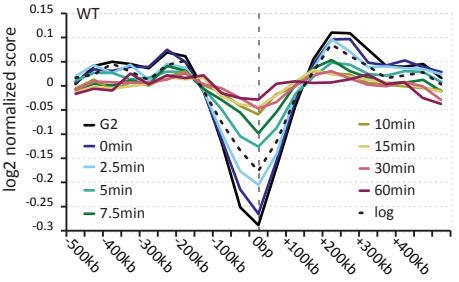

Schematic of pileup at TAD borders

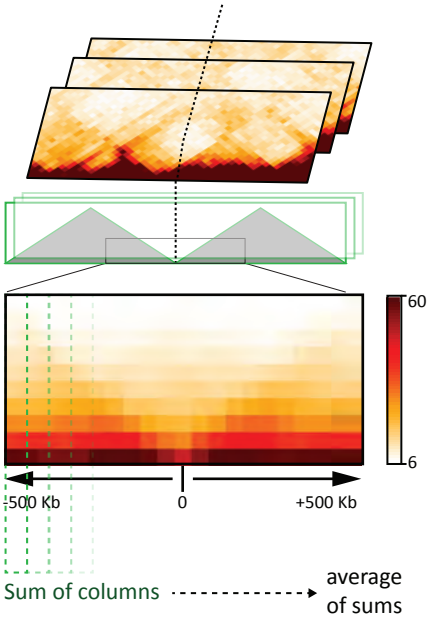

Fig.S10

Average insulation profiles around WT G_2 TAD boundaries on chromosome 7 at different time points in mitosis The schematic on the right outlines how average insulation plots are calculated around TAD boundaries. The insulation plot on the left shows the sum of the interactions for each 50kb bins located 500kb upstream or downstream of a TAD border, normalized by the average interactions for each timepoint. The presence of a minimum at 0 kb indicates a TAD boundary. As cells progress through mitosis the minimum disappears indicating loss of insulation and loss of the TAD boundary.

Fig.S11

Heatmaps from WT-20150609-R1 libraries showing 2nd Diagnal at similar length scales for chromosomes of a range of sizes

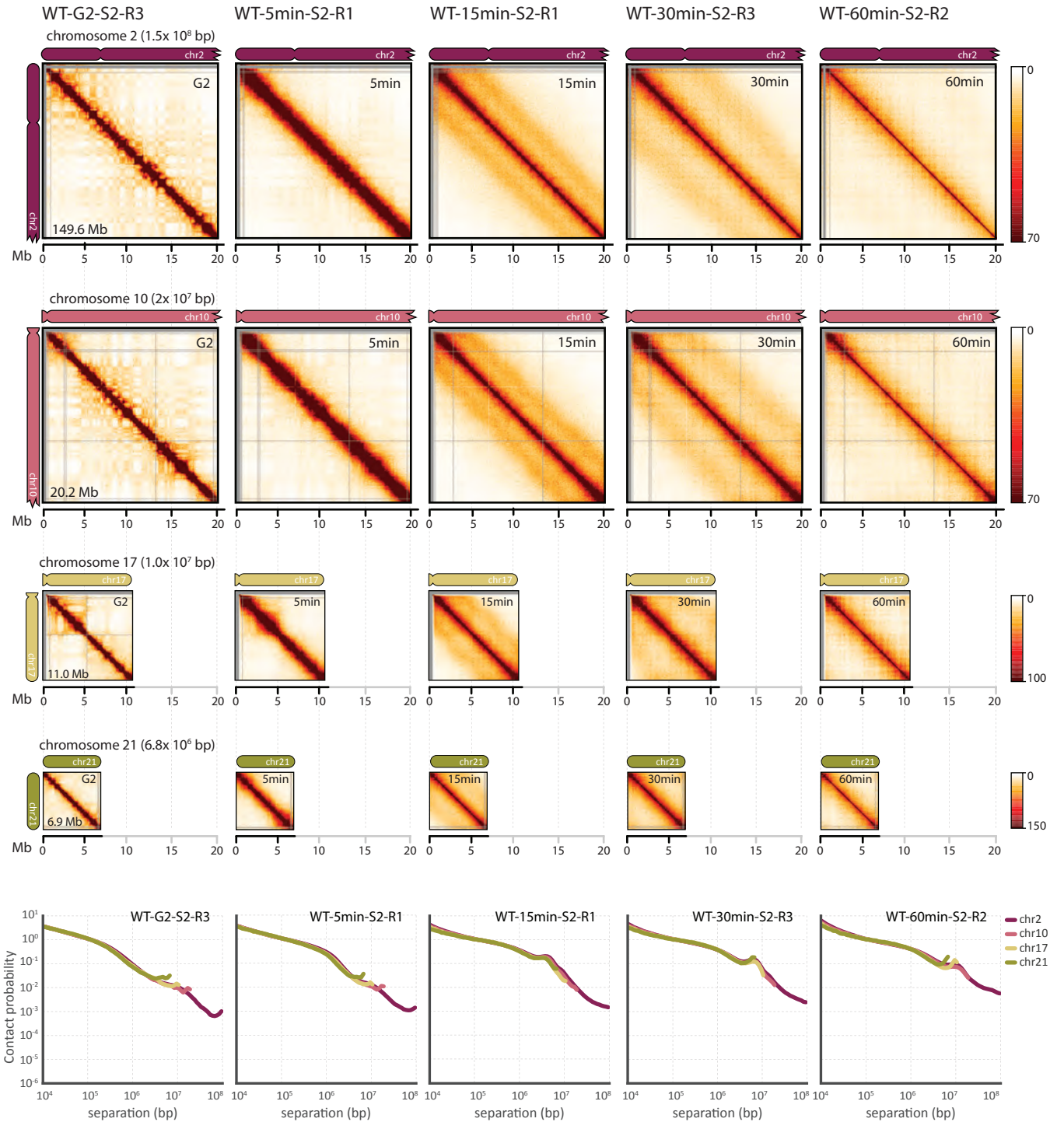

Fig.S11

Position of the second diagonal is independent of chromosome size. . We compared contact frequency plots (*P(s)*) for wild-type chromosomes 2 (150 Mb), 10 (20 Mb), 17 (11 Mb) and 21 (6.8 Mb) to illustrate that the position of the second diagonal does not depend on chromosome size. At the onset of mitosis (G2) and in prophase (t = 5 min), there is no second diagonal for any chromosome. In early prometaphase (t = 15min), a second diagonal (increase in contact frequency) can be seen for all chromosome sizes and in each Hi-C interaction map. A t = 15 minutes the position of the second diagonal is smaller than the size of each of these chromosome. At t = 30 minutes, the position of the second diagonal moved to larger genomic distance (~ 7 Mb). This distance exceeds the size of chromosome 21 (> 6.8 Mb), and leads to a disappearance of a visible increase in contact frequency for this chromosome only (as is observed in in both the Hi-C interaction map and contact frequency plot below). At t = 60 minutes the position of the second diagonal (~12 Mb) exceeds the size of chromosome 17, so that the second diagonal is no longer detected along that chromosomes. *P(s)* plots (bottom) illustrate that positions of the second diagonals are the same for all chromosomes, at different timepoints in prometaphase.

Fig.S12

A Heatmaps, compartments and TADs for HelaS3

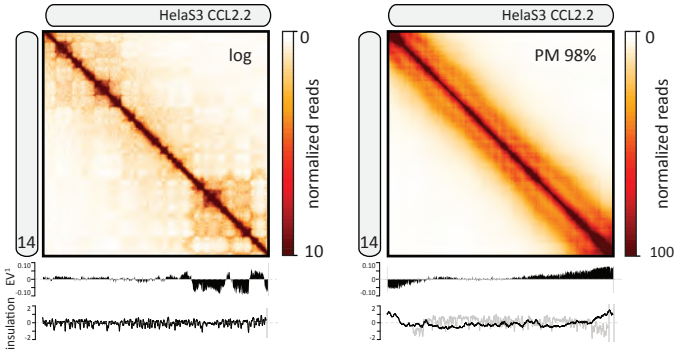

B Contact frequency *P(s)* plot for HelaS3

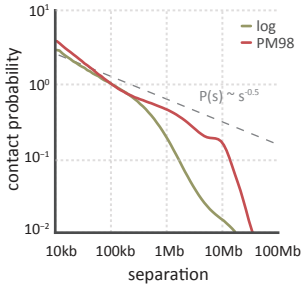

Fig.S12

Hi-C interaction maps from HeLaS3 cells arrested in late prometaphase display a second diagonal. **(A)** Hi-C interaction maps for HelaS3 (ATCC CCL-2.2). Hi-C was performed on logarithmically growing HelaS3 cells (log) and HelaS3 cells arrested in late prometaphase with nocodazole, resulting in 98% prometaphase (PM 98%). Nocodazole synchronization was performed for 3 hrs following a double thymidine block, as described before (*8*). The compartment and insulation signals below the interaction frequency heatmaps are as in **Fig. S8**. **(B)** *P*(*s)* for HelaS3 logarithmically growing cells (log) and for prometaphase arrested cells (PM98) for chromosome 14, as in **Fig. 2**. The dotted line indicates $P(s) \sim s^{-0.5}$ reported before for mitotic chromosomes (*8*). The local peak in *P(s)* around 10 Mb corresponds to the second diagonal band visible in the Hi-C interaction map (**A**).

Fig.S13

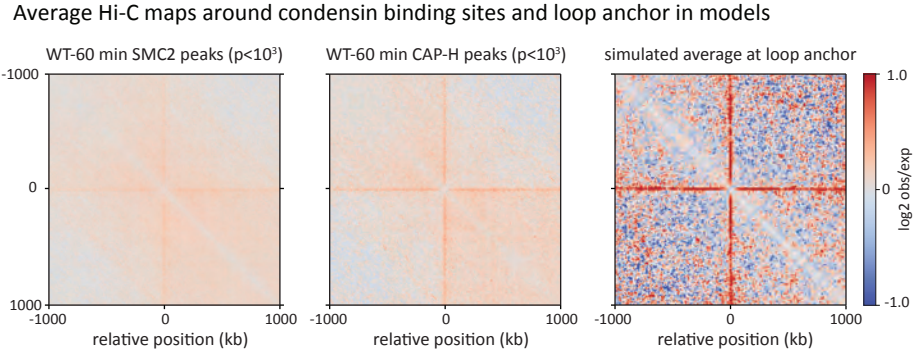
Average Hi-C maps around condensin binding sites and loop anchor in models
WT-60 min SMC2 peaks (p<10³)
WT-60 min CAP-H peaks (p<10³)
simulated average at loop anchor
-1000
0
1000
relative position (kb)
1.0
-1.0
log2 obs/exp

Fig.S13

The Hi-C contact footprint of condensin binding in experimental and simulated Hi-C maps. (**A-B**) The Hi-C maps of 60-min mitotic chromosomes averaged over 2Mb regions around (**A**) 13120 SMC2 and (**B**) 4674 CAPH ChIP-seq peaks. (**C**) The simulated Hi-C map of the 60-min mitotic chromosome model averaged over 2Mb regions around 1000 loop anchors. All three maps were normalized for the distance-dependent contact frequency decay in the corresponding dataset. See Supplementary Materials for description and interpretation of this analysis.

Fig.S14

A Second diagonal not explained by sister overlap

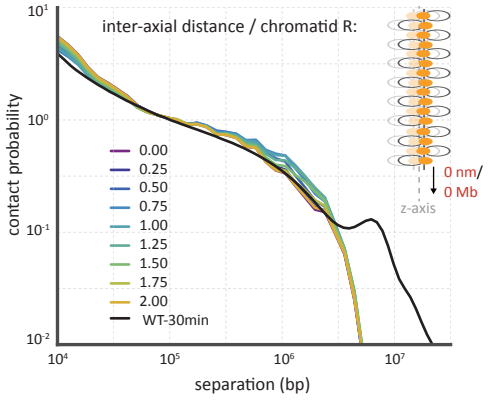

B Without nested loops it does not fit

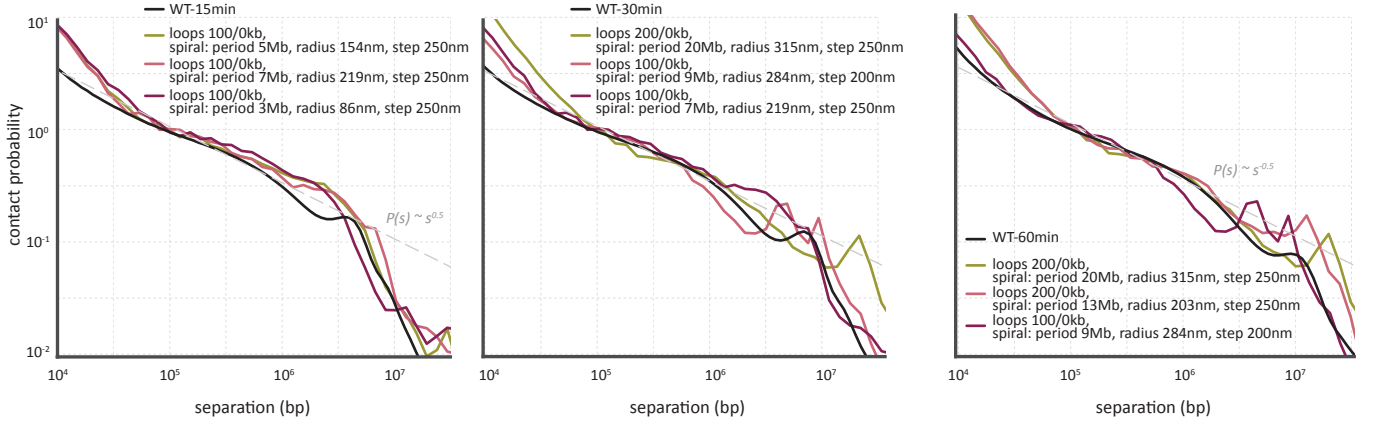

C An external helix does not fit

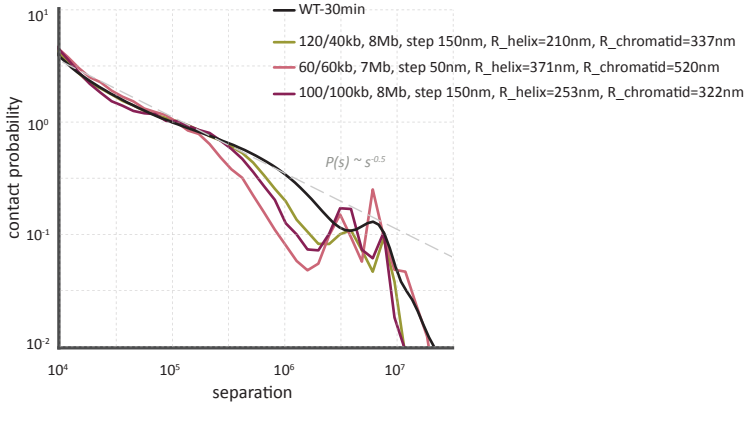

Fig.S14

Rejected polymer models of prometaphase chromosomes. **(A)** Interactions between sister chromatids do not produce a second diagonal in Hi-C interaction maps. Plot shows *P(s)* of a model of sister chromatid interactions, where two identical prophase models are overlaid on top of each other in 3D space. The *P(s)* in this model was calculated under the assumption that Hi-C would not be able distinguish between the two copies of the same locus on the two sister chromatids. *P(s)* plots were calculated for a different levels of sister chromatid overlap. **(B)** Without nested loops polymer models do not reproduce experimental Hi-C data. Plots show *P(s)* of prometaphase models without nested loops. Left-right: the panels show the best fitting models for each time point (t = 15,30 and 60 minutes) in prometaphase. **(C)** Simulation of an external helix does not produce *P(s)* that corresponds to experimental prometaphase Hi-C data. The *P(s*) curves of examples of prometaphase models with wide spiraling of the scaffold (i.e. the radius of the scaffold > ½ of the chromatid radius). All panels: black lines - experimental Hi-C data (dataset indicated in the legend); colored lines - *P(s)* plot obtained by simulations with different parameters (indicated in the legend).

Fig.S15

Gyre visualization and quantification for chromosome 2

A

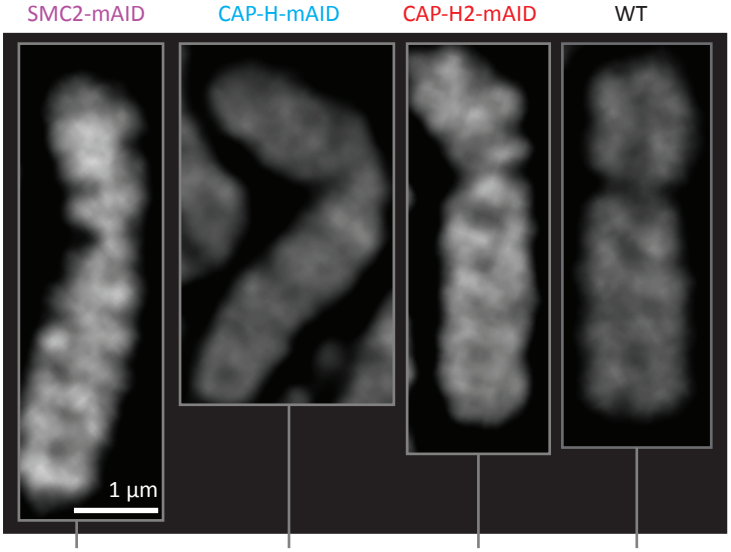

Note:
No auxin, asynchronous cells
100ng/ml cocemid for 2.5h
75 mM KCl for 5 min
Me/Ac fixation
drop/dry on slides
Vectashield with DAPI

B

chromosome 2	chromosome 2	chromosome 2	chromosome 2
10 gyres	10 gyres?	9 gyres	6 gyres?
149.6 Mb	149.6 Mb	149.6 Mb	149.6 Mb
=15 Mb/gyre	=15 Mb/gyre	= 16.6 Mb/gyre	= 24.9 Mb/gyre
length: 5.6 µm	length: 6.0 µm	length: 5.2 µm	length: 4.5 µm

C

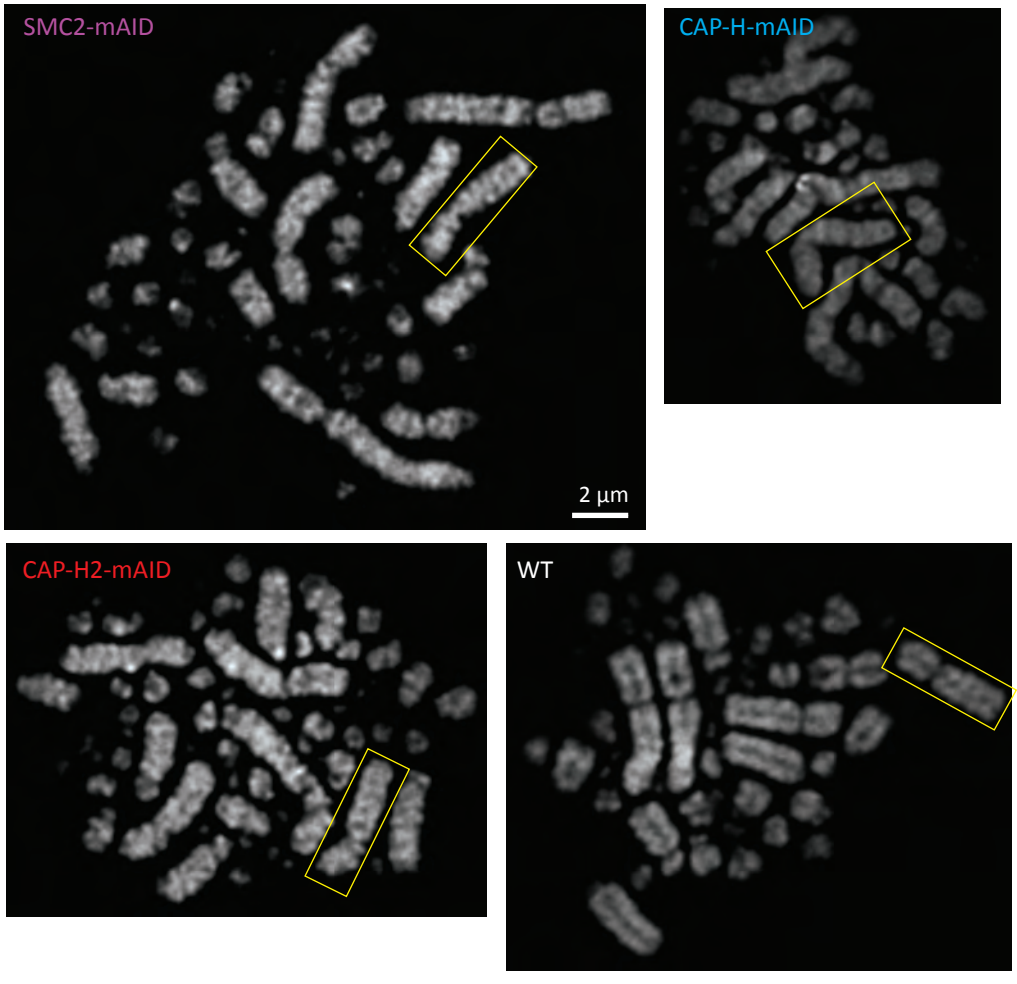

Fig.S15

Gyre visualization and quantification for chromosome 2. (**A**) Visualization (by DAPI) of a repeating structure on DT40 mitotic chromosomes following hypotonic treatment and spreading of indicated DT40 cell lines treated with colcemid for 2.5 hours. (**B**) Gyre count and size per gyre (Mb) estimates for chromosome 2. (**C**) Chromosome spreads of indicated cell lines. Boxed chromosomes are chromosome 2 based on size and centromere position, used for measurements in (**A**) and (**B**).

Fig.S16

GFP expression of condensins

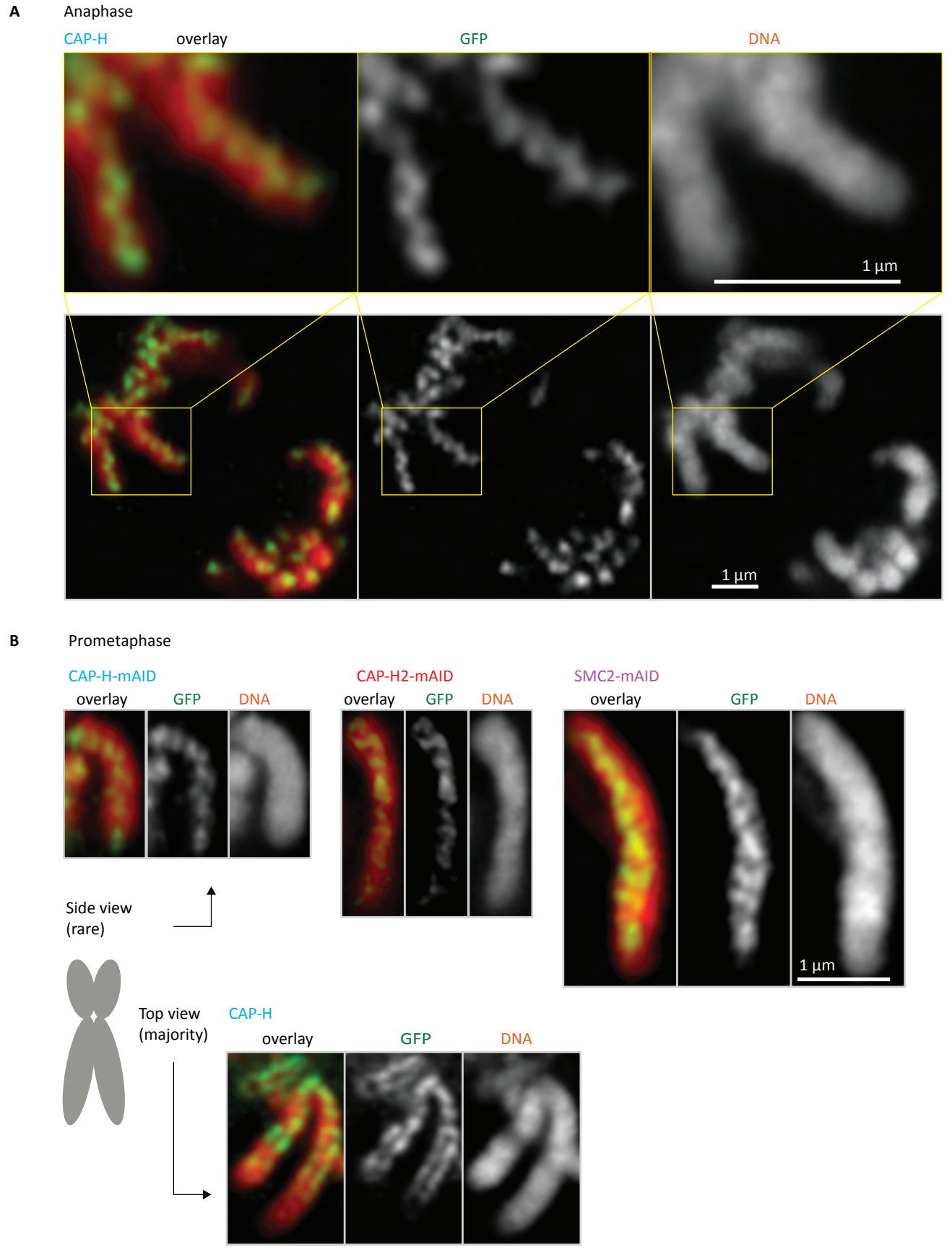

Fig.S16

Helical distribution of SMC2-mAID-GFP, CAP-H-mAID-GFP and CAP-H2-mAID-GFP in single sister chromatids. (**A**) Distribution of condensin components (as visualized by GFP) in anaphase chromosomes where only a single sister chromatid is present (this simplifies interpretation of the image). (**B**) Distribution of condensin components in rare views of prometaphase chromatids in which the two sister chromatids were oriented normal to the surface of the slide. This enabled us to use optical sectioning to resolve a single sister chromatid. Scale bars 1 μm. DNA is visualized by DAPI staining.

Fig.S17

Chromosome length and width measurements

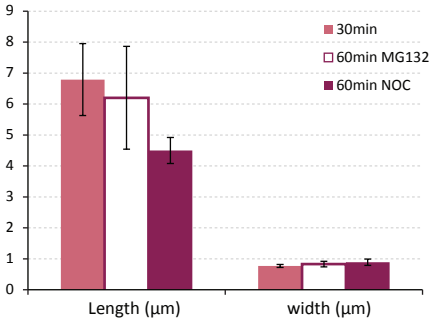

Fig.S17

Chromosome length and width measurements. Measurements of the length and width of chromosome 1 (196 Mb) in DT40 cells prepared under the conditions used for Hi-C experiments, at different timepoints in prometaphase.

Fig.S18

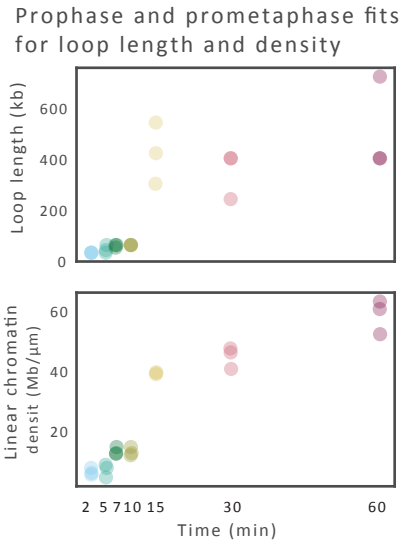
Prophase and prometaphase fits
for loop length and density
Loop length (kb)
600
400
200
0
Linear chromatin
densit (Mb/µm)
60
40
20
2 5 7 10 15
30
60
Time (min)

Fig.S18

Parameters of the best fitting models as a function time after release from G2 arrest. Chromatin density and loop length increase linearly from prophase through prometaphase.

Fig.S19

Western blots for auxin-treated condensin mutants

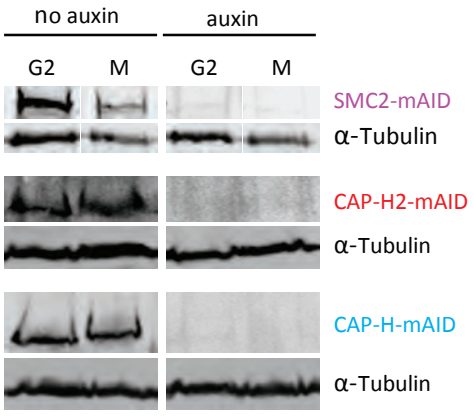

Fig.S19

Western blots showing protein levels of SMC2-mAID, CAP-H-mAID and CAP-H2-mAID for corresponding cell lines treated with or without auxin induction. Western blots indicate SMC2-mAID, CAP-H2-mAID and CAP-H-mAID are efficiently depleted after 3 hours of auxin addition.

Fig.S20 **A** Chromosome 7 Hi-C interaction maps from all individual libraries for SMC2-mAID plus auxin

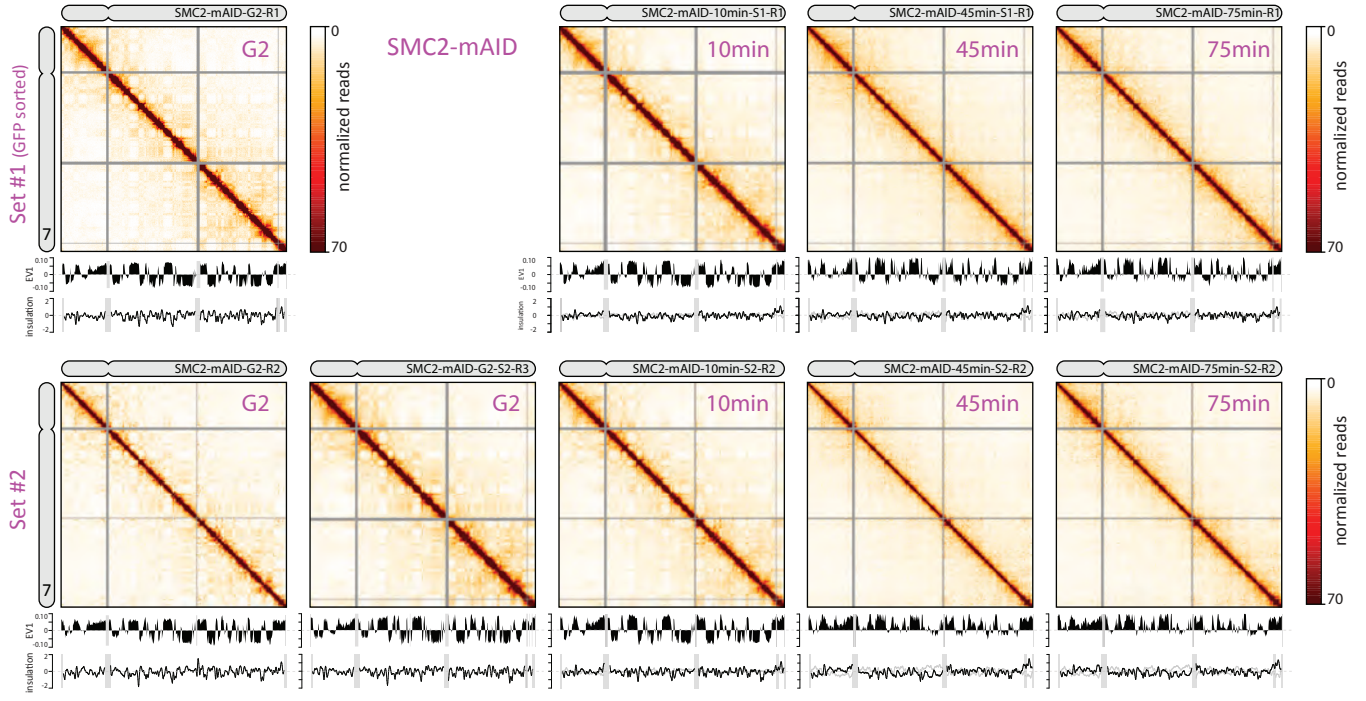

B Chromosome 7 Hi-C interaction maps from all individual libraries for CAP-H2mAID plus auxin

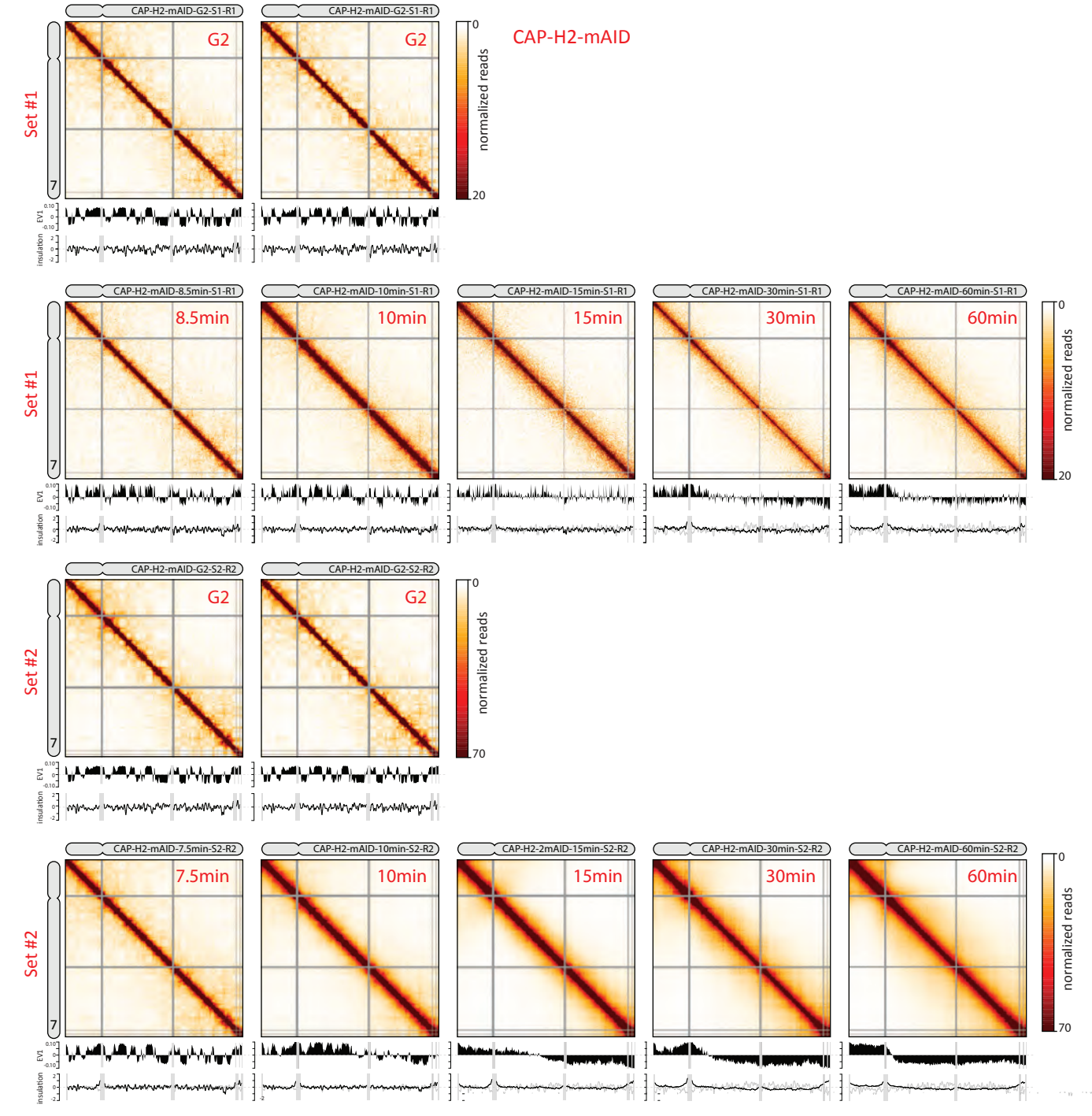

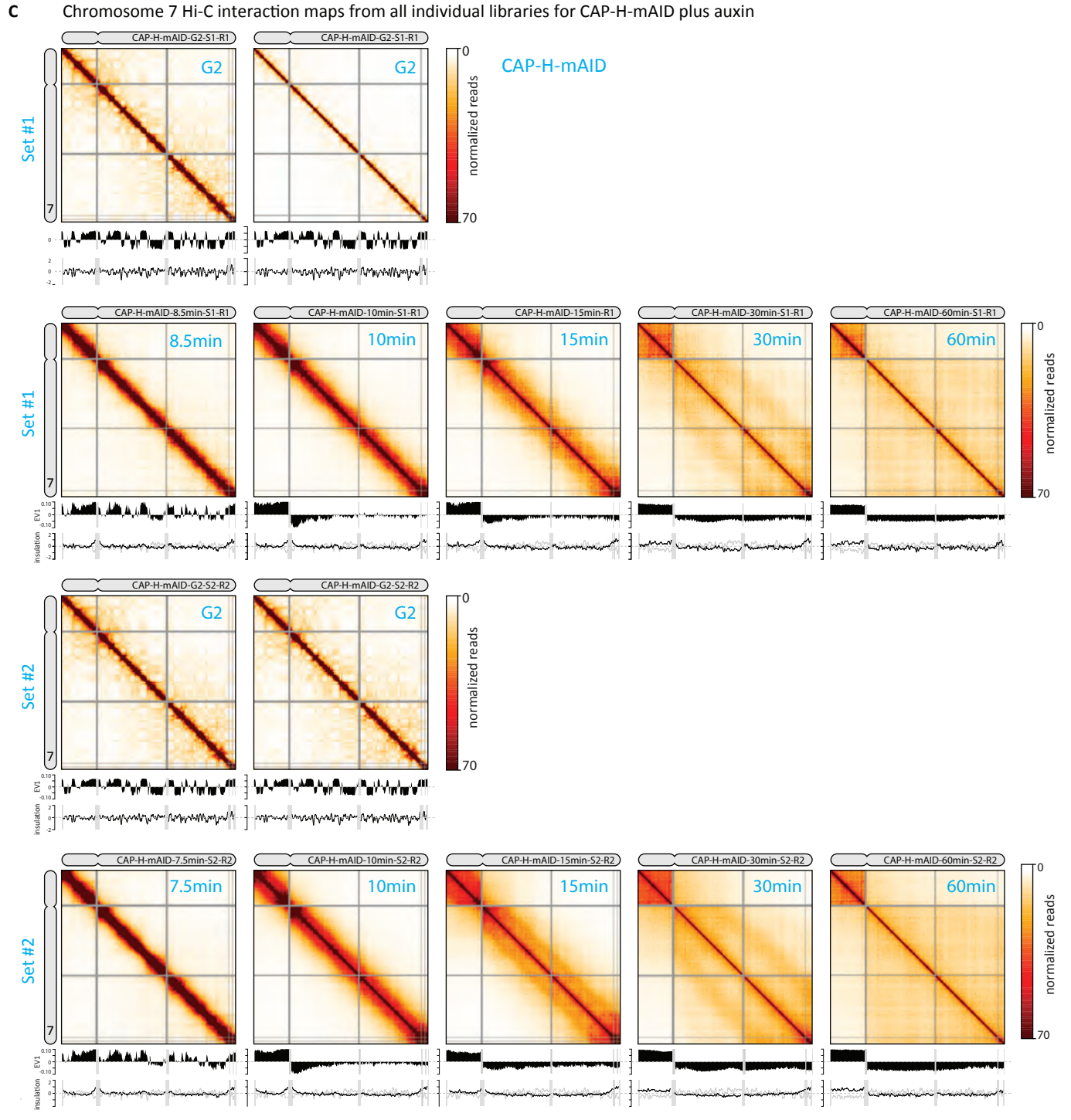
C
Chromosome 7 Hi-C interaction maps from all individual libraries for CAP-H-mAID plus auxin
CAP-H-mAID
Set #1
Set #2
CAP-H-mAID-G2-S1-R1
CAP-H-mAID-G2-S2-R2
CAP-H-mAID-8.5min-S1-R1
CAP-H-mAID-10min-S1-R1
CAP-H-mAID-15min-R1
CAP-H-mAID-30min-S1-R1
CAP-H-mAID-60min-S1-R1
CAP-H-mAID-7.5min-S2-R2
CAP-H-mAID-10min-S2-R2
CAP-H-mAID-15min-S2-R2
CAP-H-mAID-30min-S2-R2
CAP-H-mAID-60min-S2-R2
G2
8.5min
10min
15min
30min
60min
7.5min
normalized reads
0
70
7
EV1
insulation

Fig.S20

Hi-C interaction maps obtained from SMC2, CAP-H and CAP-H2 depleted cells at different timepoints in mitosis. Hi-C interaction maps were generated for chromosome 7, normalized to 1,000,000 interactions. Dataset names are indicated in the chromosome drawing on top. **Table S2** describes each sample in detail. (**A**): SMC2-mAID cells; (**B**): CAP-H2-mAID cells; (**C**): CAP-H-mAID cells. The top plot below each Hi-C interaction map displays compartment signal (Eigenvector 1; with percentage signal explained by first eigenvector). The bottom graph shows insulation score (TADs). Data for two independent time courses are shown.

Fig.S21

DAPI stain for synchronized cells

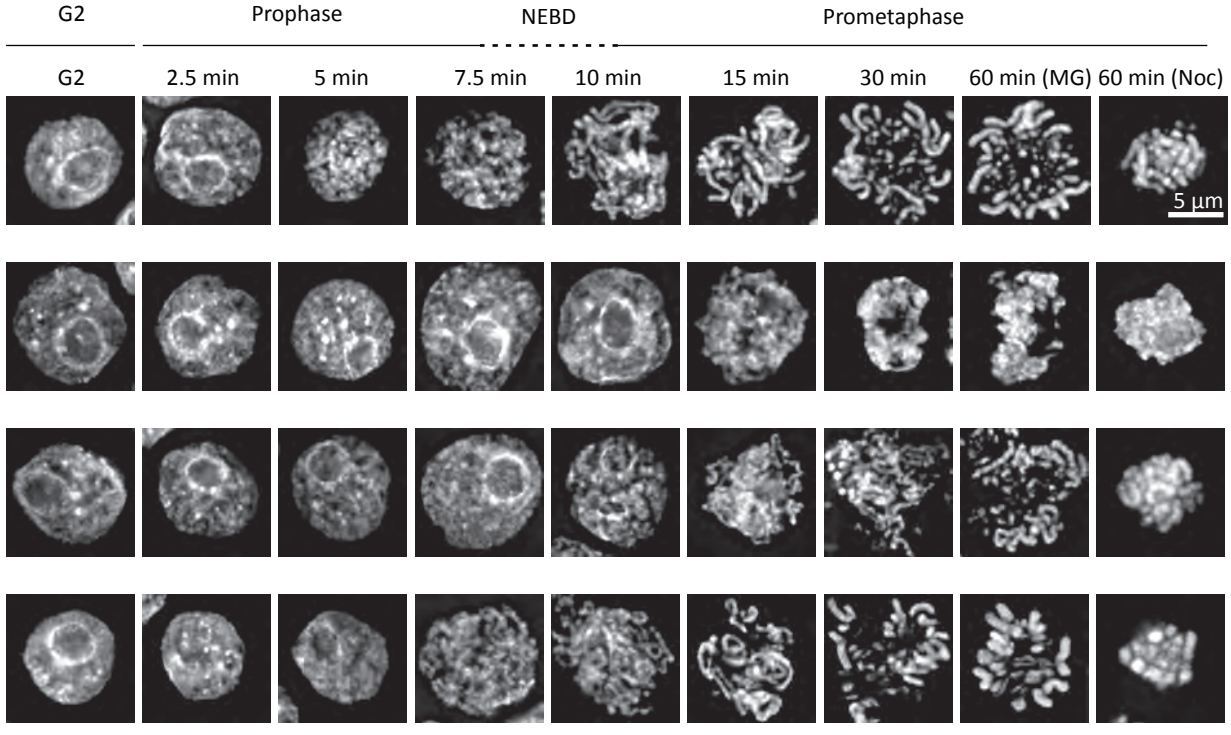

Fig.S21

Microscopy analysis of chromosome morphology for wild-type (WT) cells and SMC2, CAP-H and CAP-H depleted cells. Chromosomes were stained with DAPI. Samples are ordered by time of harvest after release from G2 arrest. NEBD was used a marker for the prophase-prometaphase transition. Cells were prevented from entering anaphase by addition of nocodazole or MG132. Scale bar indicates 5 micron. Noc: nocodazole; MG: MG132.

Fig.S22

A Saddle plots for all individual chromosome arms from SMC2-AID plus auxin

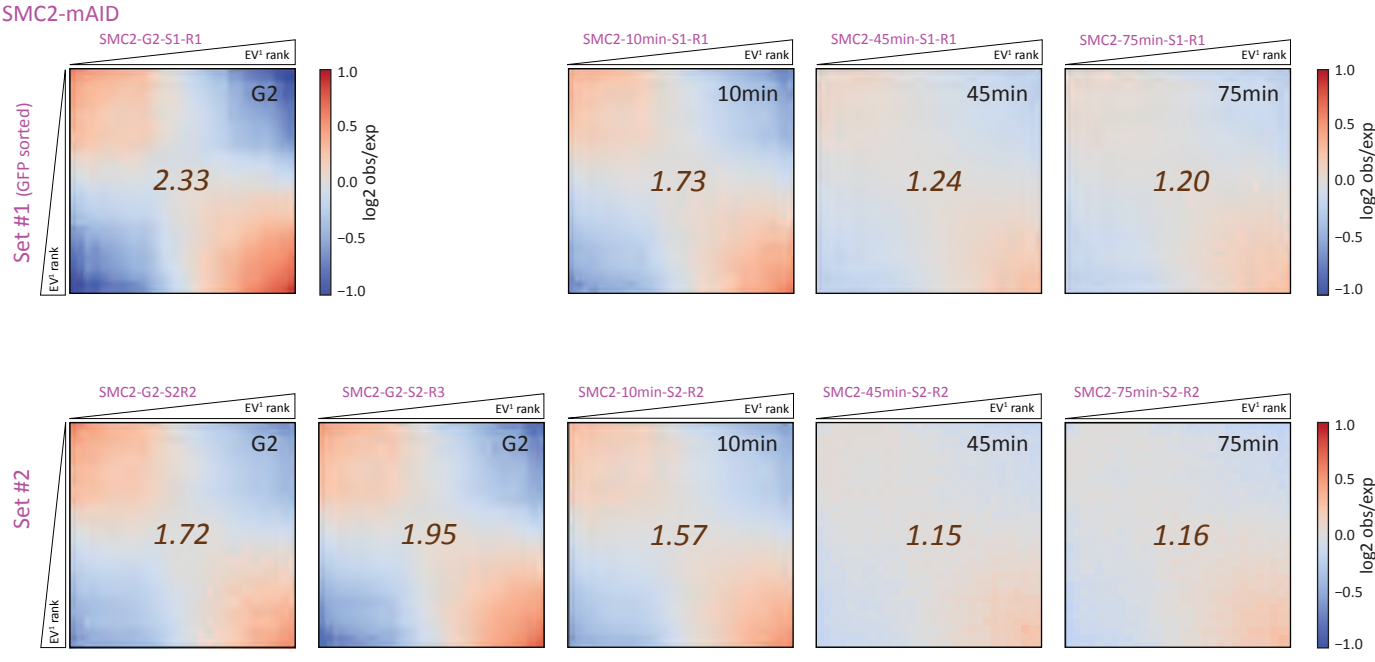

B Saddle plots for all individual chromosome arms from CAP-H2-mAID plus auxin

CAP-H2-mAID

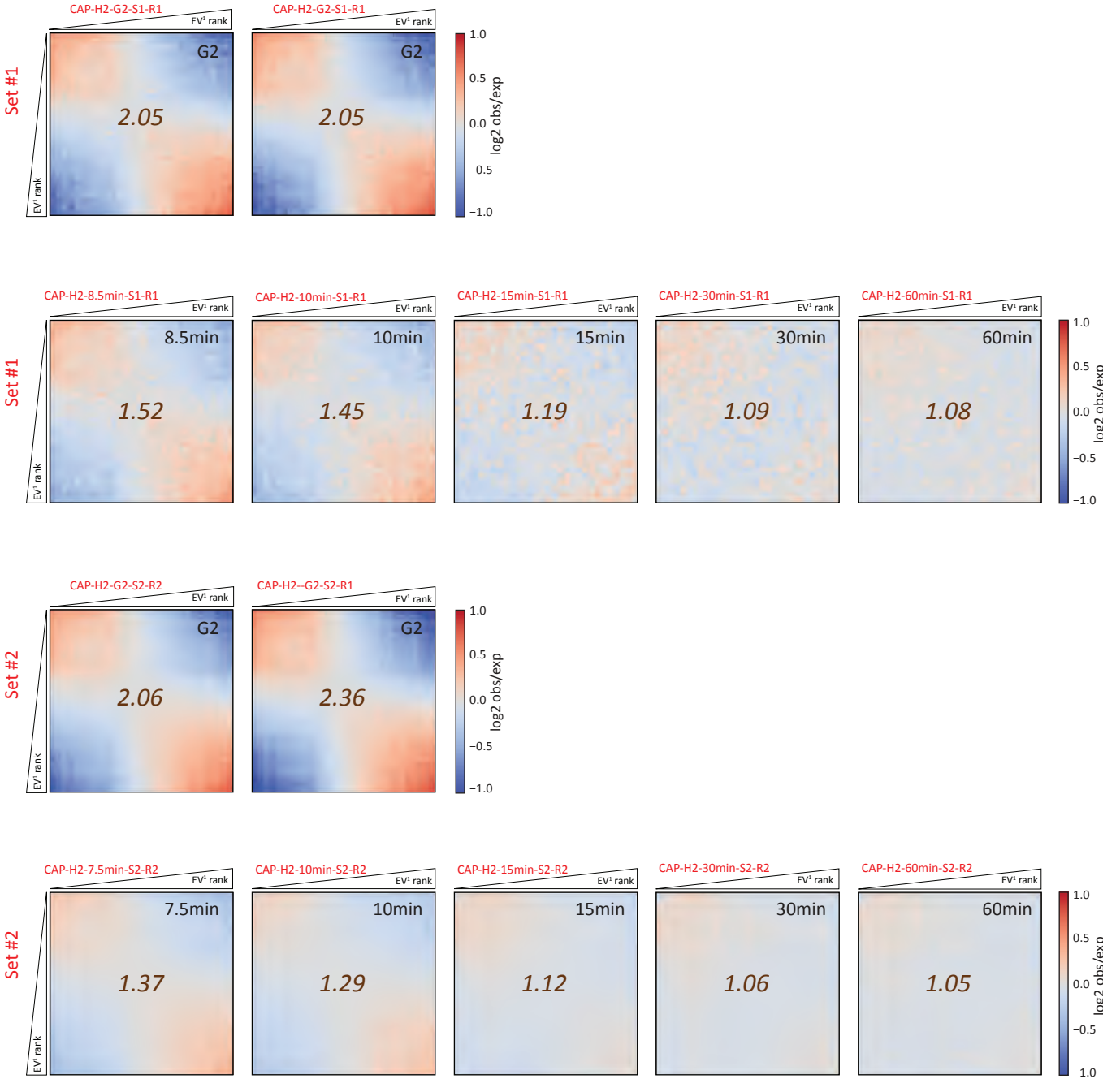

C Saddle plots for all individual chromosome arms from CAP-H-mAID plus auxin

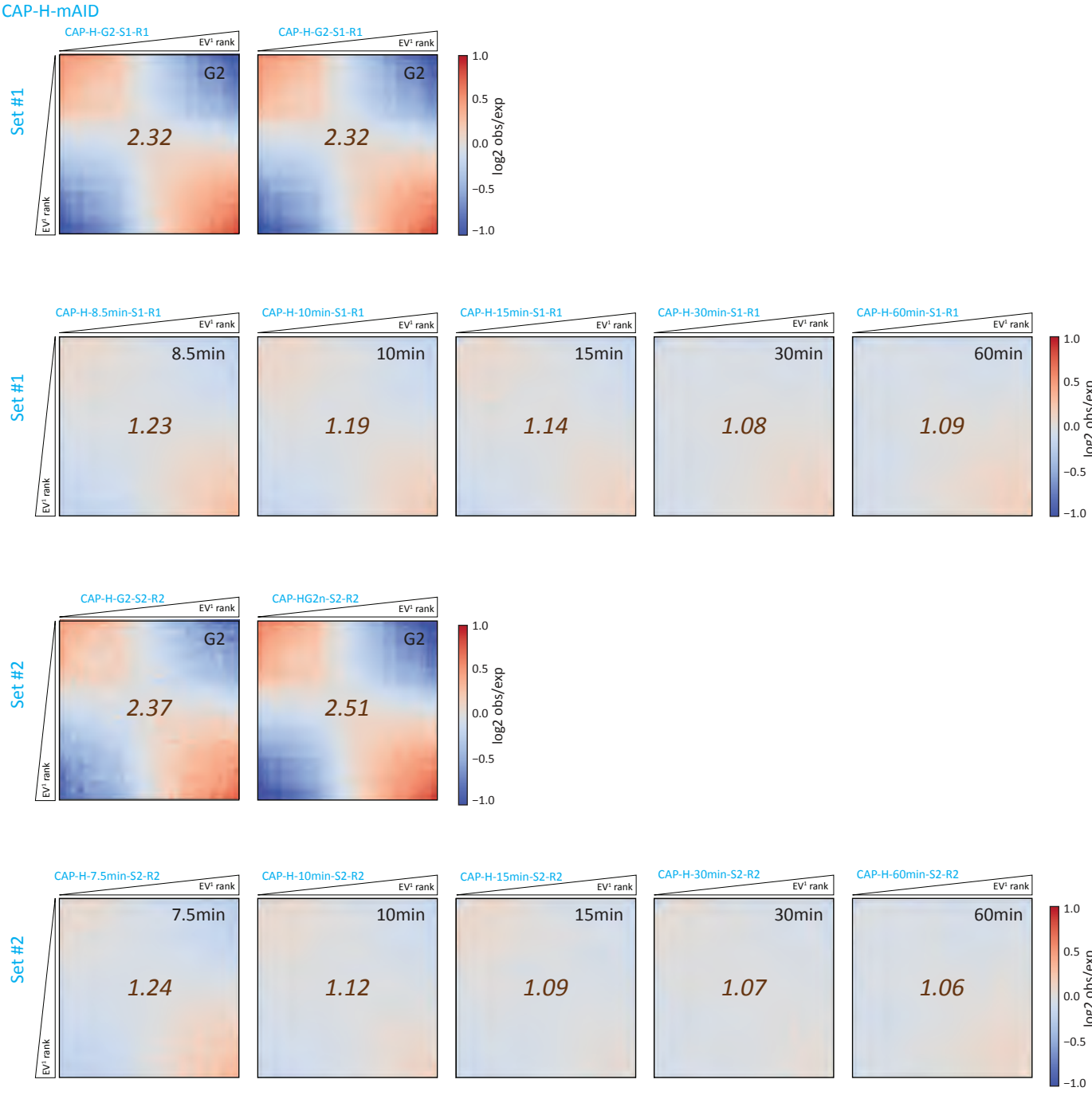

Fig.S22

Quantification of compartment interactions in SMC2, CAP-H and CAP-H2 depleted cells by saddle plots. (**A**): SMC2-mAID cells; (**B**): CAP-H2-mAID cells; (**C**): CAP-H-mAID cells. See supplementary Materials and legend of **Fig. S9** for description of saddle plots.

Fig.S23

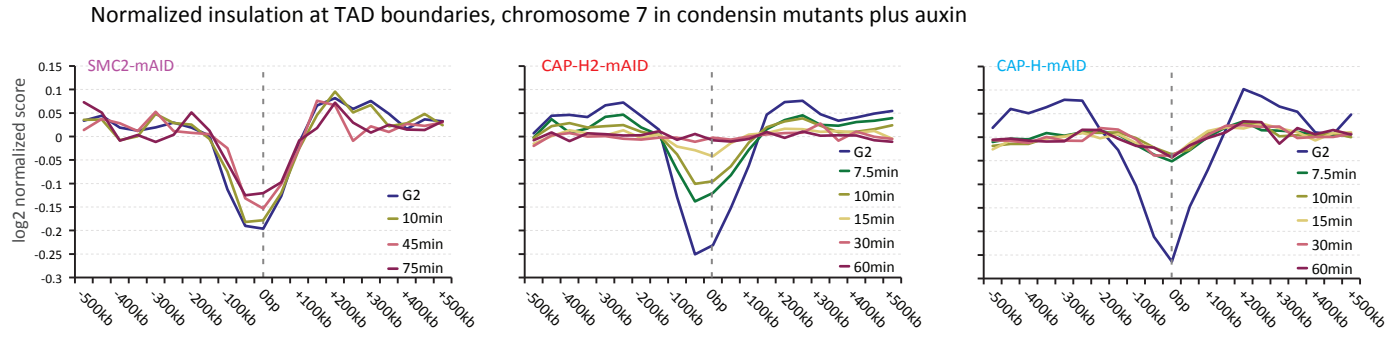
Normalized insulation at TAD boundaries, chromosome 7 in condensin mutants plus auxin
SMC2-mAID
CAP-H2-mAID
CAP-H-mAID
log2 normalized score
0.15
0.1
0.05
0
-0.05
-0.1
-0.15
-0.2
-0.25
-0.3
G2
10min
45min
75min
7.5min
15min
30min
60min
-500kb
-400kb
-300kb
-200kb
-100kb
0bp
+100kb
+200kb
+300kb
+400kb
+500kb

Fig.S23

Average insulation profiles around G_2 TAD boundaries on chromosome 7 for cells depleted for SMC2, CAP-H2 or CAP-H at different timepoints in mitosis. Plots show the sum of the interactions for each 100 kb bin 500kb upstream or downstream of the TAD normalized by the average sum of interactions for each time point. The presence of a minimum at 0 kb indicates a TAD boundary. SMC2 depletion prevents complete loss of the minimum, indicated maintenance of TAD boundaries. Depletion of CAP-H2 leads to slower loss of TAD boundaries as compared to WT (**Fig. S10**). Depletion of CAP-H does not prevent efficient loss of TAD boundaries.

Fig.S24

A Contact frequency *P(s)* plots for all individual chromosome arms plus auxin

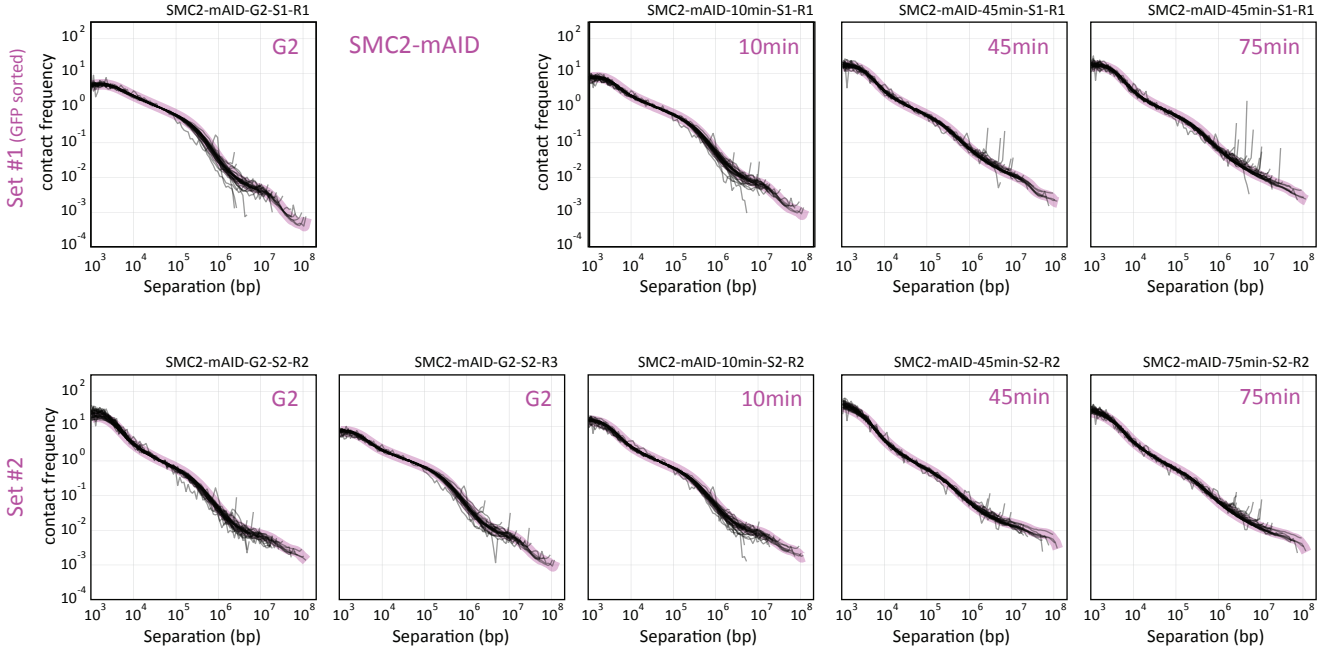

B CAP-H2-mAID contact frequency *P(s)* plots for all individual chromosome arms plus auxin

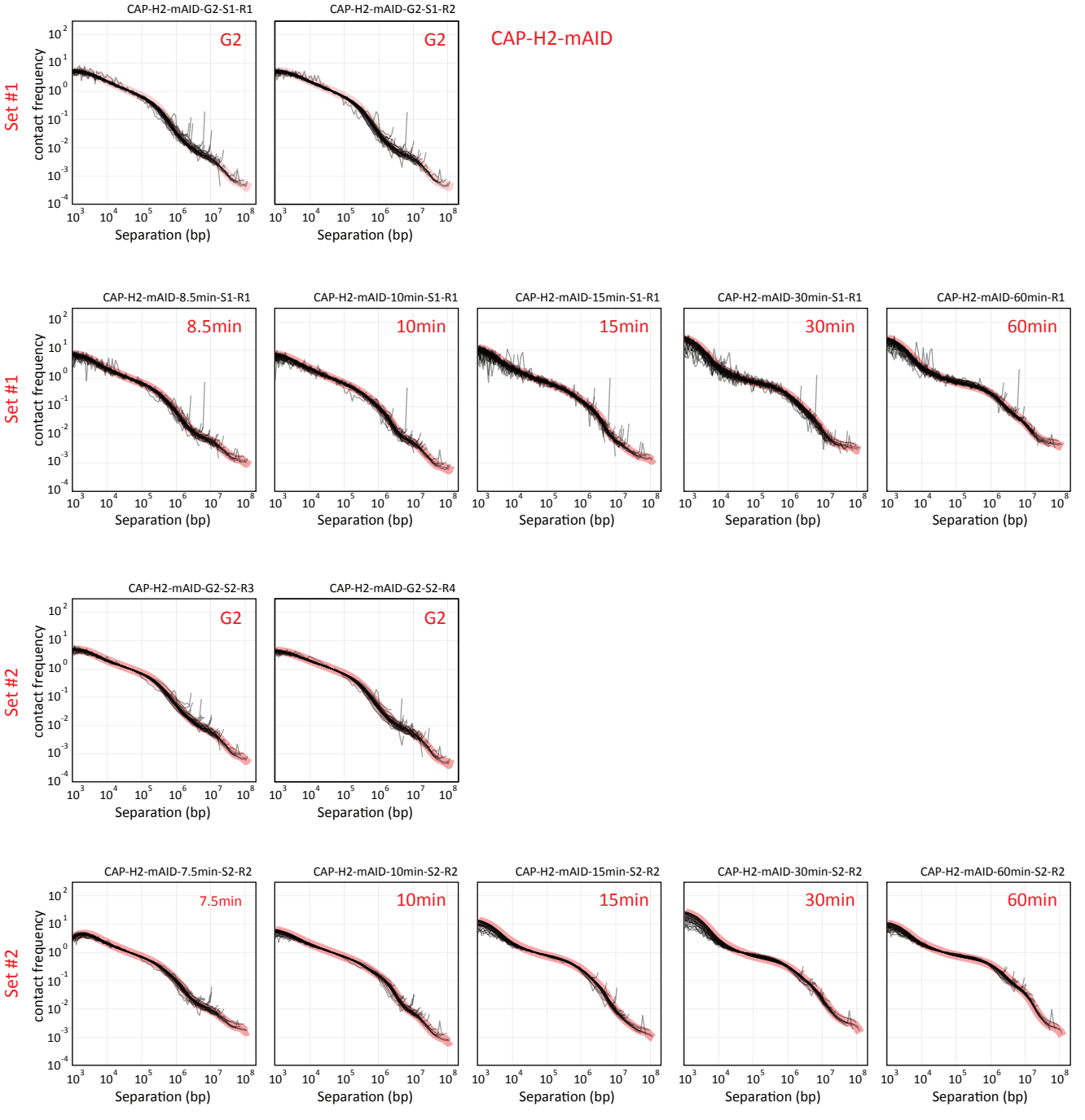

C CAP-H contact frequency *P(s)* plots for all individual chromosome arms plus auxin

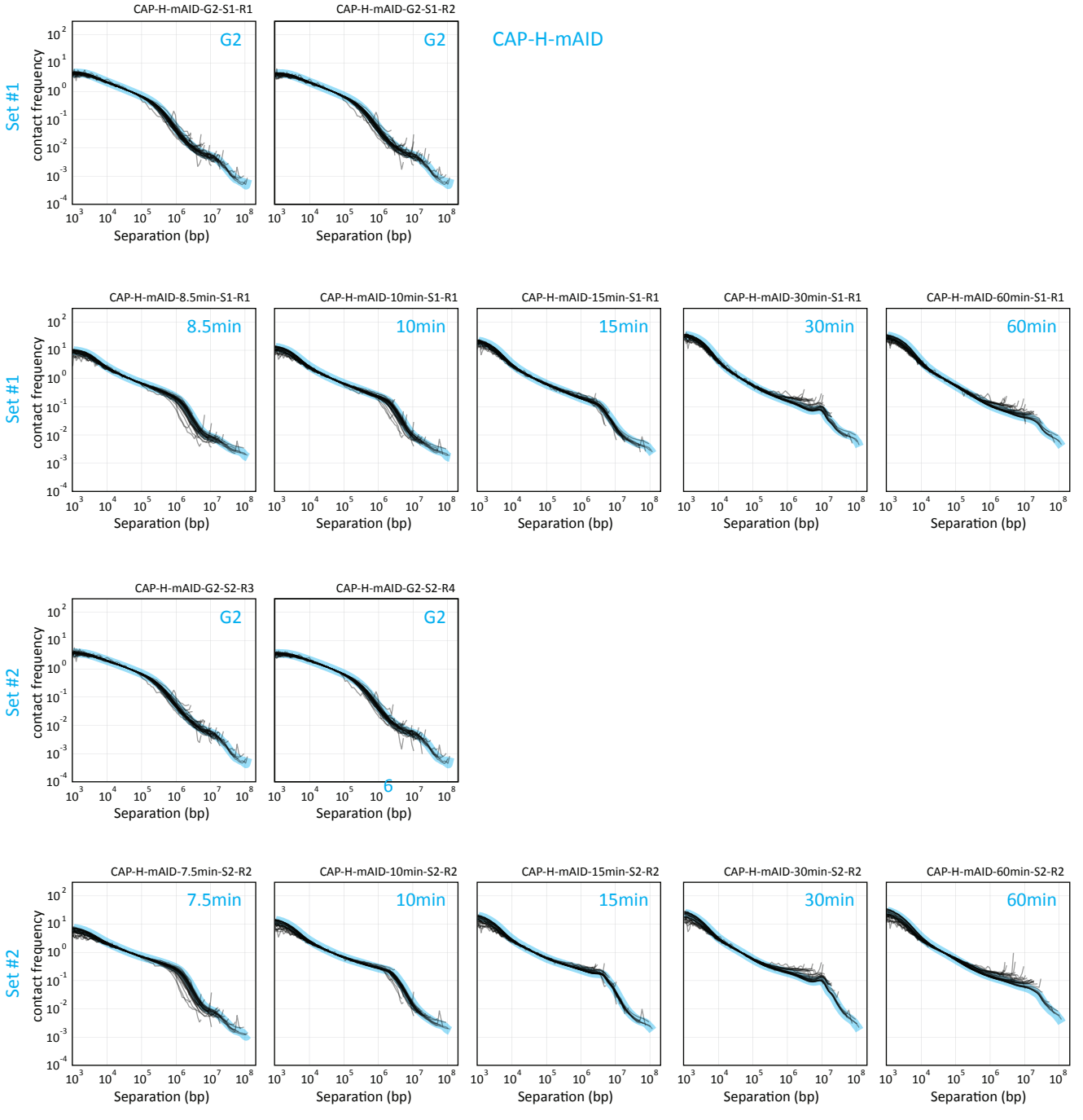

Fig.S24

Contact frequency (*P(s)*) derived from Hi-C data obtained from CDK1as synchronized DT40 cells depleted for SMC2, CAP-H2 or CAP-H. (**A**): SMC2-mAID cells; (**B**): CAP-H2-mAID cells; (**C**): CAP-H-mAID cells. Contact frequency *P(s)* plots are shown for all Hi-C datasets (two independent time courses). Plots for individual chromosome arms are shown in gray; the deviation from the mean decay is shown in magenta (SMC2), red (CAP-H2-mAID) or blue (CAP-H-AID).

Fig.S25

Contact frequency *P(s)* plots for all chromosome arms combined from condensin mutants plus auxin

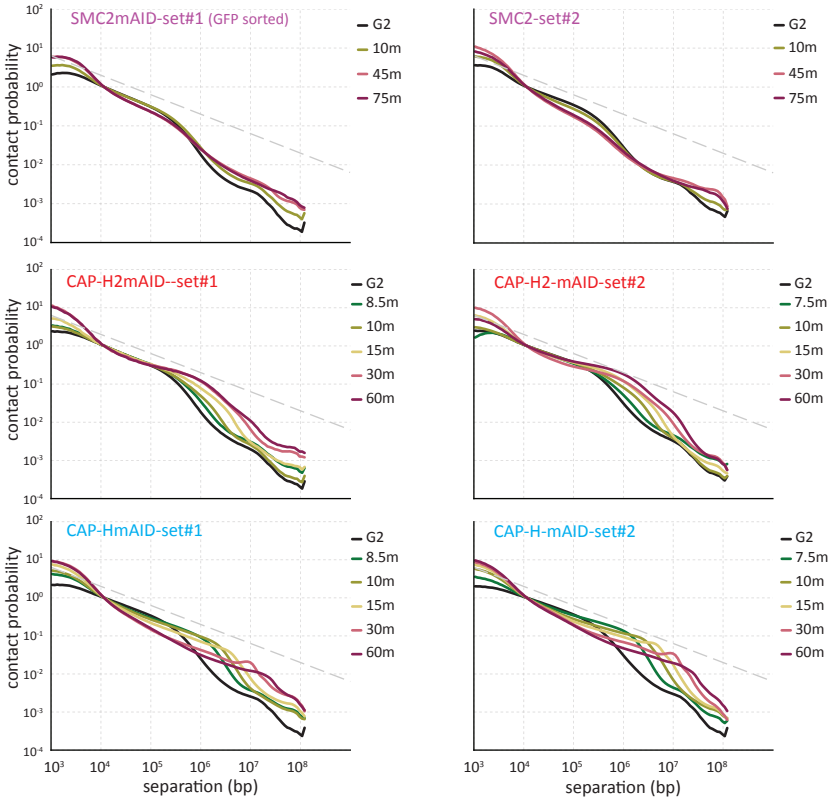

Fig.S25

P(s) plots for SMC2-mAID, CAP-H2-mAID and CAP-H-mAID DT40 cells at different time after degron induction and release from G2 arrest. *P(s)* plots for Hi-C datasets corresponding to different timepoints in each time course experiment are plotted in one graph.

Fig.S26

Contact frequency *P(s)* derivative plots for all chromosome arms combined from condensin mutants plus auxin

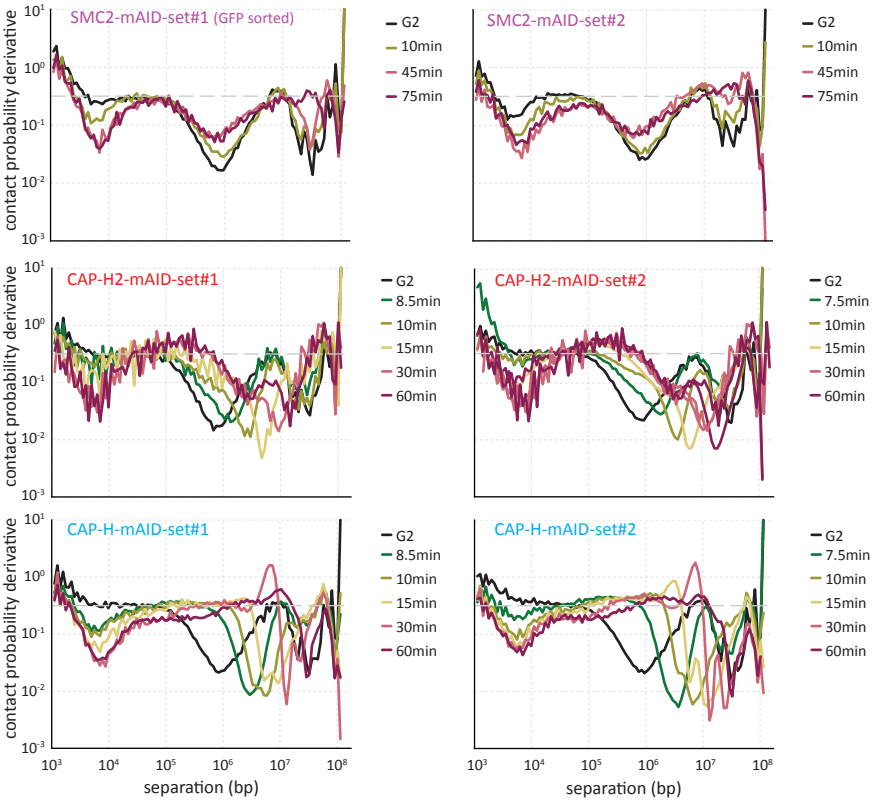

Figure S26

Derivatives of *P(s)* plots for SMC2, CAP-H2 or CAP-H depleted cells. Plots show derivative of *P(s)* plots for Hi-C datasets obtained from SMC2-mAID, CAP-H2-mAID and CAP-H-mAID CDK1as cells at indicated time points after auxin-induced protein depletion and release from G_2 arrest.

Fig.S27

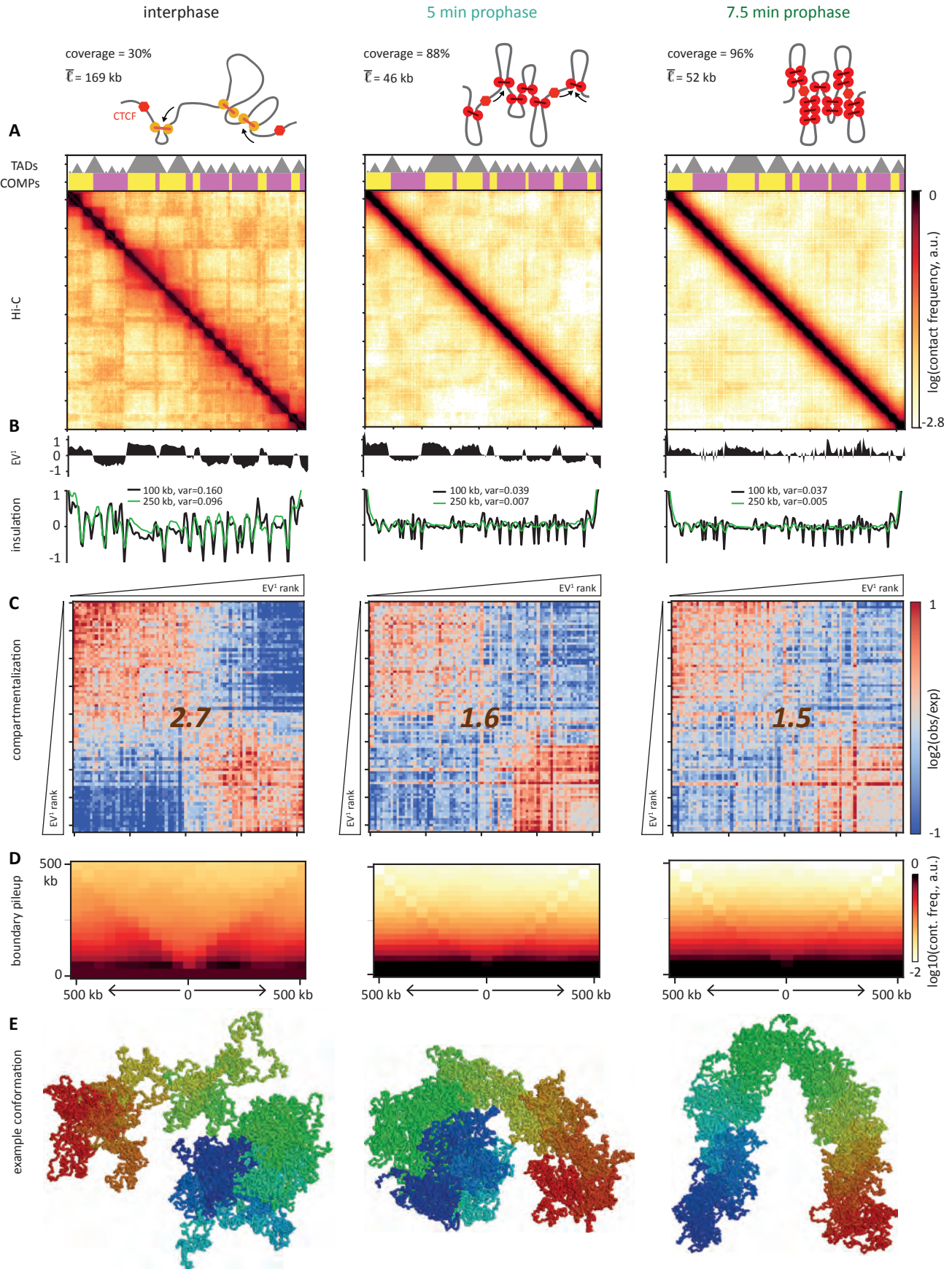
interphase
5 min prophase
7.5 min prophase
coverage = 30%
ℓ = 169 kb
CTCF
coverage = 88%
ℓ = 46 kb
coverage = 96%
ℓ = 52 kb
A
TADs
COMPs
Hi-C
log(contact frequency, a.u.)
0
-2.8
B
EV¹
100 kb, var=0.160
250 kb, var=0.096
100 kb, var=0.039
250 kb, var=0.007
100 kb, var=0.037
250 kb, var=0.005
insulation
C
compartmentalization
EV¹ rank
2.7
1.6
1.5
log2(obs/exp)
D
boundary pileup
500 kb
0
log10(cont. freq., a.u.)
E
example conformation

Figure S27

Chromosome compaction by loop extrusion suppresses TADs and compartments even in the presence of CTCF. A possible mechanism for the loss of TADs (gray rectangles in (**A**) and insulation signal in (**B**)) and A/B compartments in prophase is revealed by polymer simulations with loop extrusion and compartmental interaction. In interphase, the chromatin fiber is locally compacted into TADs by sparse loop extrusion factors (LEFs, yellow). Compartmentalization (yellow/magenta COMPs in (**A**) and EV^1 in (**B, C**)) emerges from preferential interactions between loci of the same compartment type. In prophase, coverage of chromosomes by LEFs (red) increases strongly. According to this model, TADs disappear in prophase because CTCF sites are now just one of many loci where loops are stacked up against each other and contacts across them are as frequent as between them (TAD boundary pileup in (**D**)), compartmentalization is suppressed (compartmentalization plots in (**C**)), because the bottlebrush imposes linear ordering and reduces fiber flexibility. Example conformation renderings are shown in (**E**).

Tables S1-S3

Table S1

Sample and FACS summary. All samples with their cell type used for Hi-C libraries (name_galGal5) are listed by the names used throughout all figures. For each cell collection (time), the main cell cycle phase, treatments and drugs used are listed. FACS analysis was used to determine AID-GFP presence (and level of protein degradation). A subset of cells was sorted (sorted) for GFP positivity or negativity respectively, as indicated.

Table S2

Hi-C dataset overview. The names used corresponds to those used in figures and **Table S1**. Each harvested cell sample was submitted to Hi-C as part of a set (Set#) and the sequencing results and mapping statistics for galGal5 (gg5) are listed. Valid pair: reads mapped for both ends; NRVP (non-redundant valid pairs): valid pairs with duplicate reads removed (see Supplementary Methods); %Dangling: percentage of dangling ends (inward reads [→|←] derived from false biotin incorporation); %cis: percentage of intra-chromosomal interactions; %redundant: percentage of exact (PCR) duplicate reads (used to determine NRVP).

Table S3

DNA constructs used for generation of cell lines. Mutant: name used throughout the manuscript; background: cell line used to generate modified cell line; construct: vector used to generate mutants; FBOX: the specific FBOX protein used to degrade the AID-fused mutant; endogenous: the modification to the endogenous locus using homologous recombination (HR) or CRISPR; alleles: the number and location of altered alleles in DT40 mutants; selection: antibiotic resistance used for mutant selection; publication: previous work using these mutants.

Table S4

Short- and long-distance parts of the *P(s)*.Equalization of the contribution of the short- and long-distance parts of the *P(s)* was calculated using the r.m.s. *P(s)* difference in each of these regions separately and reporting the mean of the two.

Movie S1

The emergence of nested loop architecture in loop extrusion lattice simulations of slow- and fast-exchanging condensin populations. The video shows the simulated dynamics of loops extruded by condensins I and II on a 2Mb chromatin segment during two hours of simulated time. The positions of loops formed by fast-exchanging condensins I are shown as blue semi-transparent arcs and those formed by slow-exchanging condensin II are shown in red. The detailed description of simulations is available in **Supplemental Materials and Methods**.